



THE UNIVERSITY *of* EDINBURGH

Edinburgh Research Explorer

## Cosmogenic Nuclide Systematics and the CRONUScalc Program

**Citation for published version:**

Marrero, S, Phillips, FM, Borchers, B, Lifton, N, Aumer, R & Balco, G 2016, 'Cosmogenic Nuclide Systematics and the CRONUScalc Program', *Quaternary Geochronology*.

**Link:**

[Link to publication record in Edinburgh Research Explorer](#)

**Document Version:**

Peer reviewed version

**Published In:**

Quaternary Geochronology

**Publisher Rights Statement:**

Copyright © 2015 Elsevier B.V. All rights reserved.

**General rights**

Copyright for the publications made accessible via the Edinburgh Research Explorer is retained by the author(s) and / or other copyright owners and it is a condition of accessing these publications that users recognise and abide by the legal requirements associated with these rights.

**Take down policy**

The University of Edinburgh has made every reasonable effort to ensure that Edinburgh Research Explorer content complies with UK legislation. If you believe that the public display of this file breaches copyright please contact [openaccess@ed.ac.uk](mailto:openaccess@ed.ac.uk) providing details, and we will remove access to the work immediately and investigate your claim.



# Cosmogenic Nuclide Systematics and the CRONUScale Program

Shasta M. Marrero<sup>a,b</sup>, Fred M. Phillips<sup>b</sup>, Brian Borchers<sup>c</sup>, Nathaniel Lifton<sup>d</sup>, Robert Aumer<sup>e,c</sup>, Greg Balco<sup>f</sup>

<sup>a</sup>Corresponding author; University of Edinburgh, School of Geosciences, Drummond Street, Edinburgh, EH8 9XP, UK

<sup>b</sup>New Mexico Tech, Earth & Environmental Science Dept., Socorro, NM, 87801, USA

<sup>c</sup>New Mexico Tech, Department of Mathematics, Socorro, NM, 87801, USA

<sup>d</sup>Purdue University, West Lafayette, IN, USA

<sup>e</sup>Current position: BENTEK Energy, 32045 Castle Court, Ste. 200, Evergreen, CO 80439, USA

<sup>f</sup>Berkeley Geochronology Center, Berkeley, CA 94709, USA

---

## Abstract

As cosmogenic nuclide applications continue to expand, the need for a common basis for calculation becomes increasingly important. In order to accurately compare between results from different nuclides, a single method of calculation is necessary. Calculators exist in numerous forms with none matching the needs of the CRONUS-Earth project to provide a simple and consistent method to interpret data from most commonly used cosmogenic nuclides. A new program written for this purpose, CRONUScale, is presented here. This unified code presents a method applicable to  $^{10}\text{Be}$ ,  $^{26}\text{Al}$ ,  $^{36}\text{Cl}$ ,  $^3\text{He}$ , and  $^{14}\text{C}$ , with  $^{21}\text{Ne}$  in testing. The base code predicts the concentration of a sample at a particular depth for a particular time in the past, which can be used for many applications. The multi-purpose code already includes functions for calculating surface exposure age for a single sample or for a depth profile containing multiple samples. The code is available under the GNU General Public License agreement and can be downloaded and modified to deal with specific atypical scenarios.

*Keywords:* cosmogenic nuclide, exposure age calculator, beryllium-10, chlorine-36, aluminum-26, helium-3, carbon-14

31 **1. Introduction**

32 The CRONUS-Earth Project, funded by the U.S. National Science Foun-  
33 dation, is intended to improve many aspects of cosmogenic isotope use and  
34 help create a consistent, accurate use of the technique within the commu-  
35 nity. It functioned in collaboration with CRONUS-EU, a similarly motivated  
36 group in Europe funded by the European Commission. One important part  
37 of that project is the creation of a code that can consistently perform nec-  
38 essary calculations for different scaling schemes and that is applicable to  
39 many of the commonly used nuclides ( $^{10}\text{Be}$ ,  $^{26}\text{Al}$ ,  $^{36}\text{Cl}$ ,  $^3\text{He}$ ,  $^{14}\text{C}$ ). The pro-  
40 gram presented here, called CRONUScalc, is a joint effort by the CRONUS  
41 Project to incorporate all major contemporary advances in the understand-  
42 ing of cosmogenic-nuclide production and to treat all the commonly used  
43 nuclides in an internally consistent fashion. This calculator directly incor-  
44 porates much of the format and function of the  $^{26}\text{Al}/^{10}\text{Be}$  code by Balco  
45 et al. (2008), but it extends the functionality beyond  $^{26}\text{Al}/^{10}\text{Be}$  as well as  
46 introducing other new features. The new CRONUScalc code keeps the orig-  
47 inal modular format, but has updated the code with functions to perform  
48 production/accumulation calculations, calibrations, and surface and depth  
49 profile exposure ages and erosion rates.

50 The base code of CRONUScalc predicts the cosmogenic nuclide concen-  
51 tration in a sample (of either finite or point thickness) at a given depth  
52 at a particular time in the past. This function allows great versatility  
53 in earth science applications. CRONUScalc can be used to predict con-  
54 centrations of a suite of nuclides for a variety of purposes. The code is  
55 published under the GNU General Public License, version 2 terms. The  
56 basic code can be modified to output many different parameters and can  
57 be downloaded (<https://bitbucket.org/cronusearth/cronus-calc>) and  
58 modified to suit a user's particular needs. The code repository is open to user  
59 contributions, allowing for sharing and future growth of the program. The  
60 version of the program described in this paper is marked online as Version  
61 2.0 in the downloadable repository.

62 The code has been used to create two specific calculators to address the  
63 common need to calculate surface exposure ages from unknown samples.  
64 The two calculators that are included with the program are a single-sample  
65 surface exposure age calculator and a multi-sample depth-profile calculator.  
66 Additional functions in the code are designed to calibrate production rates,  
67 test alternative scaling frameworks, and determine erosion rates.

68 The fundamental theory and assumptions that have gone into the code are  
69 described in this paper. This paper matches the CRONUScalc downloadable  
70 version 2.0 available in the repository. There are significant new features in  
71 CRONUScalc as compared to previous calculators, including a more accurate  
72 method of integration through time and depth, updated geomagnetic history,  
73 newly produced calibration data sets, updated and calibrated muon produc-  
74 tion model, and the ability to calculate exposure ages for single samples at  
75 depth or perform a calibration.

## 76 2. CRONUScalc Program Systematics

77 The complete set of equations and fundamental theory behind the code  
78 can be found in Appendix A and will be useful for those new to the topic  
79 or interested in particular details because Appendix A systematically doc-  
80 uments all the equations used in CRONUScalc, without need for the reader  
81 to refer back to numerous prior publications. The sections contained in the  
82 main body of the paper are designed to provide a general cosmogenic user  
83 with a summary of the systematics and relevant publications, focusing on the  
84 new research developments compared to the code described in Balco et al.  
85 (2008). A standard reference that describes the equations for production  
86 of cosmogenic nuclides is Gosse & Phillips (2001). The equations given in  
87 that paper have provided the baseline for numerous applications of cosmo-  
88 genic nuclides. CRONUScalc is an implementation of equations from Gosse  
89 & Phillips (2001) and from newer sources, as described in each section.

### 90 2.1. Production Equations

#### 91 2.1.1. Spallation

92 Cosmogenic-nuclide production from spallation, defined for this purpose  
93 as the interaction of a high-energy particle with a target nucleus producing  
94 a cosmogenic nuclide as a product of the reaction, follows a well-established  
95 exponential decrease with depth. At the surface, spallation is typically the  
96 dominant production mechanism. All the nuclides discussed in this paper  
97 are produced through at least one spallation pathway. The formula for the  
98 instantaneous production rate from spallation ( $P_{s,m}$ ) is (Gosse & Phillips,  
99 2001; Schimmelpfennig et al., 2008):

$$P_{s,m}(Z) = S_T \sum S_{el,s} P_{m,k}(0) C_k \exp\left(-\frac{Z}{\Lambda_{f,e}}\right), \quad (1)$$

100 where  $P_{m,k}$  is the modern sea-level, high-latitude production rate of species  
101 m by spallation of element k at 2010 solar modulation (atoms  $\text{g}^{-1} \text{a}^{-1}$ );  $S_T$   
102 is the topographic shielding factor (unitless);  $S_{el,s}$  is the geographical scaling  
103 factor for spallation reactions for the particular reaction of interest, which  
104 varies temporally due to fluctuations in the geomagnetic field or solar mag-  
105 netic field (unitless);  $C_k$  is the concentration of the element k (atoms  $\text{g}^{-1}$   
106  $\text{a}^{-1}$ ); and  $\Lambda_{f,e}$  is the effective attenuation length for the spallogenic reactions  
107 (applies to fast neutrons and spallogenic protons) ( $\text{g cm}^{-2}$ ). The production  
108 is summed for all target elements k that produce nuclide m to give the total  
109 spallation production rate.

### 110 2.1.2. Epithermal and Thermal Neutrons

111 Low-energy cosmogenic nuclide production, including that from thermal  
112 and epithermal neutrons, does not follow a simple exponential pattern with  
113 depth due to the atmosphere-ground interface effects. Low-energy neutrons  
114 produced in the upper  $\sim 50$  cm of rock tend to diffuse upward out of the  
115 rock and into the atmosphere, resulting in a reduction of the flux as the rock  
116 surface is approached. Phillips et al. (2001) analytically solved the neutron-  
117 flux differential equation across the land/atmosphere interface to obtain the  
118 appropriate production equations.

119 The production of cosmogenic nuclides via the low-energy pathway is  
120 dependent on the neutron flux, which is, in turn, dependent on the composi-  
121 tion of the rock. In order to calculate production from this pathway using a  
122 universal parameter, the value  $P_f(0)$  is calibrated instead of any parameter  
123 dependent on composition. The  $P_f(0)$  parameter is the production rate of  
124 epithermal neutrons from fast neutrons in the air just above the surface. This  
125 parameter can be used in conjunction with the sample-specific composition  
126 to calculate the applicable production rates.

127 Cosmogenic nuclide production via low-energy neutrons is implemented  
128 as described in Gosse and Phillips (2001), except for a small modification  
129 to the calculation of muon-induced neutrons (discussed in Section 2.1.3). In  
130 several cases, small typos in Gosse and Phillips (2001) were also corrected  
131 (see the appendix for the corrected equations). Low-energy production is  
132 currently only implemented for  $^{36}\text{Cl}$ , but could be modified by advanced  
133 users to apply to other nuclides with low-energy production pathways, such  
134 as  $^3\text{He}$ .

135 *2.1.3. Muons*

136 Although muons make up a large portion of the incoming cosmic-ray flux  
137 at the earth’s surface, the low interaction rate means that they penetrate  
138 more deeply into the subsurface than neutrons. Muon contributions to total  
139 cosmogenic nuclide production are typically small at the surface, but become  
140 important at depth (Stone et al., 1998). Accurate calculation of muogenic  
141 production is thus important for sampling sites with large erosion rates or  
142 samples at depth.

143 Early calculators employed an exponential approximation for production  
144 from muons reactions according to Stone et al. (1998). Balco et al. (2008)  
145 implemented a newer model by Heisinger et al. (2002b,a) that calculates  
146 the production from muon reactions using physical parameters determined  
147 from laboratory irradiation experiments. Braucher et al. (2003) used a deep  
148 core to provide evidence that the parameters specified by Heisinger et al.  
149 (2002a,b) overestimated actual  $^{10}\text{Be}$  production by fast muons by approxi-  
150 mately a factor of two. This was supported by additional profile data mea-  
151 sured by Braucher et al. (2011) and by Kim & Englert (2004), as well as  
152 reanalysis of previously published deep profile data by Braucher et al. (2013).

153 Rather than using parameters estimated from laboratory muon irradiations,  
154 the CRONUS-Earth Project has adopted values calibrated from nuclide-  
155 concentration profiles at carefully selected sites (Fig 1 in Phillips et al., 2015;  
156 Marrero, 2012; Borchers et al., 2015). A 30-m deep quartzite core from  
157 Antarctica has allowed the calibration of muon production parameters for  
158  $^{26}\text{Al}$  and  $^{10}\text{Be}$  (Fig 1 in Phillips et al., 2015). For  $^{36}\text{Cl}$ , previously published  
159 data sets (Evans, 2001; Stone et al., 1998) collected from quarry profiles were  
160 used to reparameterize the muon model for cosmogenic  $^{36}\text{Cl}$  production from  
161 muons on Ca and K (Marrero, 2012). A CRONUS-Earth depth profile was  
162 not measured for  $^{14}\text{C}$ , and  $^{14}\text{C}$  profiles measured by other investigators (Kim  
163 et al., 2007; Lupker et al., 2013, 2015) have shown problems with distinguish-  
164 ing slow-muon production from production by muogenic neutrons, therefore  
165 at present CRONUScalc uses the values from Heisinger et al. (2002a,b) for  
166  $^{14}\text{C}$ . This may result in less accuracy for the calculation of muogenic  $^{14}\text{C}$   
167 production than for other nuclides, but ongoing investigations (Lupker et al.,  
168 2013, 2015) may yield improved parameter values in the near future.

169 Nuclide production by fast muon reactions ( $P_{\mu,fast}$ ) is described by Equa-  
170 tion 2 (Heisinger et al., 2002b). The parameter  $\sigma_0$  was selected as the cali-  
171 bration parameter for the production of nuclides by muon reactions, as dis-

172 cussed in (Fig 1 in Phillips et al., 2015). This was mainly because it is the  
 173 only nuclide-dependent parameter in the fast production equation. However,  
 174 direct calibration of the  $\sigma_0$  parameter also eliminates any dependence on the  
 175 accuracy of the conversion from  $\sigma_{190}$  (the parameter measured in the labo-  
 176 ratory irradiation experiments) to  $\sigma_0$  (see Equation B.27, from Equation 14  
 177 in Heisinger et al. (2002b)).

$$P_{\mu,fast} = S_T \phi_{\mu,total}(Z) \beta(Z) (\bar{E}(Z))^\alpha \sigma_0 N_{t,i} \quad (2)$$

178 Where the factor  $\beta(Z)$  is a function of the mean total muon energy and  
 179 is shown in Equation B.25 and  $\bar{E}$  is defined as the mean muon energy at a  
 180 given depth  $Z$  and is shown in Equation B.26.  $\phi_{\mu,total}$  is the total muon flux  
 181 at the site, as calculated by the same equations used to calculate the fluxes  
 182 for the Lifton et al. (2014) scaling framework.  $N_{t,i}$  is the number density of  
 183 the atoms in the target element (in units of at/g). This value is a constant  
 184 for each nuclide unless the composition of the target changes, as it does for  
 185  $^{36}\text{Cl}$ .  $\alpha$  is an energy-dependent coefficient that parameterizes the energy  
 186 dependence of the cross-section ( $\sigma$ ) on muon energy. Experimental results  
 187 permit values for  $\alpha$  between 0.75 and  $>1.0$  (Heisinger et al., 2002b) so the  
 188 CRONUS-Earth Project chose a value of  $\alpha = 1.0$ . By assuming that  $\alpha$  equals  
 189 one,  $\beta$  will also be equal to one.

190 Nuclide production by slow negative muon capture ( $P_{\mu-}$ ) is described by  
 191 Equation 3, originally from Charalambus (1971) and discussed in detail for  
 192  $^{36}\text{Cl}$  by Stone et al. (1998). The production rate depends on the stopping rate  
 193 of negative muons ( $\phi_{\mu-}$ ) as well as the nuclide-dependent factors ( $f_{i,C}$ ,  $f_{i,D}$ ,  
 194  $f_i^*$ ).  $\phi_{\mu-}$  is derived from the muon flux calculated by the same equations used  
 195 in Lifton et al. (2014).  $f_{i,D}$  is the fraction of muons stopped by element  $k$  and  
 196 absorbed by the nucleus before decay of the muon.  $f_{i,C}$ , the compound factor,  
 197 represents the fraction of the muons that are captured by a target element  
 198 (as opposed to the other elements present) within the bulk rock. The formula  
 199 for the compound factor (Equation E.40) is taken from Charalambus (1971)  
 200 and the values are consistent with those used by Heisinger et al. (2002a).

$$P_{\mu-} = S_T \phi_{\mu-}(Z) f_{i,C} f_{i,D} f_i^* \quad (3)$$

201 The remaining parameter,  $f_i^*$ , the particle emission channel probability,  
 202 is the probability that the excited nucleus of the target atom will emit the  
 203 proper particle to result in transformation to the nuclide of interest. Heisinger  
 204 et al. (2002a) experimentally determined  $f_i^*$  values for the production of  $^{26}\text{Al}$

205 (from Si),  $^{10}\text{Be}$  and  $^{14}\text{C}$  (from O), and  $^{36}\text{Cl}$  (from K and Ca), but these  
 206 values tend to overestimate nuclide concentrations measured in depth profiles  
 207 in the same fashion as for fast muon production (Fig 1 in Phillips et al.,  
 208 2015; Braucher et al., 2011). The production parameters for slow negative  
 209 muon capture,  $f_i^*$ , were calibrated by fitting to the measured CRONUS-Earth  
 210 profile for  $^{10}\text{Be}$  and  $^{26}\text{Al}$  and by fitting to previously published profiles  
 211 for  $^{36}\text{Cl}$ , as previously discussed.

212 The muon-capture reactions can release neutrons that later participate  
 213 in neutron-capture reactions (muon-induced neutrons). Instead of assuming  
 214 an exponential decrease in muon production with depth to calculate this  
 215 flux, as most previous calculators do, the new muon module described above  
 216 is used to calculate production with depth. The muon code calculates the  
 217 negative muon stopping rate ( $\phi_{\mu-}(Z)$ ) and total muon flux ( $\phi_{\mu f}(Z)$ ) terms  
 218 at a given depth for the calculation of the production rate of muon-induced  
 219 neutrons (Equation 4). This muon-induced neutron production rate is used  
 220 in the thermal and epithermal neutron flux equations (Equations B.30 and  
 221 B.34), which are ultimately used to determine the production rate via the  
 222 low-energy neutron pathway.

$$P_{n,\mu}(Z) = Y_s \phi_{\mu-}(Z) + 5.8 \times 10^{-6} \phi_{\mu f}(Z), \quad (4)$$

223 where  $Y_s$  is the average neutron yield per stopped negative muon (Fabryka-  
 224 Martin, 1988).

#### 225 2.1.4. Radiogenic Production

226 Radiogenic production in this context refers to the generation of low-  
 227 energy neutrons by reactions related to the radioactive decay or spontaneous  
 228 fission of U or Th, and the subsequent absorption of those neutrons to pro-  
 229 duce nuclides of interest, principally  $^{36}\text{Cl}$ . Although  $^3\text{He}$  is also produced  
 230 from Li in this manner (Lal, 1987; Dunai et al., 2007), only  $^{36}\text{Cl}$  radiogenic  
 231 subtraction is incorporated into the program and the discussion below focuses  
 232 on  $^{36}\text{Cl}$  for that reason. The radiogenic low-energy neutron flux is assumed to  
 233 be in equilibrium with the concentrations of uranium (U) and thorium (Th)  
 234 in the rock. This component is quantified using measured concentrations  
 235 of U and Th and the method described in Fabryka-Martin (1988), which is  
 236 based on the formulations developed by Feige et al. (1968). These equations  
 237 are shown in Appendix B.5.

238 The quantification of the bulk rock properties requires fundamental nu-  
 239 clear properties for each element. The original table of these properties pre-



240 sented in Fabryka-Martin (1988) has now been corrected and updated using  
241 the information in Mughabghab (2006) and Schimmelpfennig et al. (2009).  
242 A table of nuclear properties for all the elements considered in CRONUScalc  
243 is shown in Table 1.

244 In most studies, the rocks (not the exposure age) are sufficiently old that  
245 the assumption of equilibrium is reasonable. Even for younger features, such  
246 as a newly-erupted basalt, the assumption of equilibrium is reasonable due to  
247 equilibration with the uranium and thorium concentrations prior to eruption,  
248 so long as the magma did not undergo differentiation or mixing that signifi-  
249 cantly changed its U and Th contents less than  $\sim 0.5$  Ma prior to sampling.  
250 The alternative is to allow production from radiogenic sources to begin at  
251 the exposure age (or any rock formation age). This difference in assumption  
252 is small for most  $^{36}\text{Cl}$  samples and no data set currently exists to differenti-  
253 ate between the two assumptions. This assumption is only significant for  
254 young samples with high chlorine contents ( $> 50\%$  production from Cl) or  
255 significant U or Th.

## 256 *2.2. Calibration Technique*

257 The production rates incorporated into the CRONUScalc code are the  
258 results from CRONUS-Earth Project calibrations. The calibration data set  
259 compiled by CRONUS-Earth includes a large number of sites representing a  
260 large range of latitudes, longitudes, and elevations. Ideal sites should have  
261 little uncertainty in the sample parameters (e.g. erosion rate, elevation,  
262 shielding, independent age constraints, etc.). The sites were divided into  
263 two categories based on the quality of the site, with the sites that came clos-  
264 est to fitting the criteria above placed into the 'primary calibration data set'.  
265 Additional sites with independent age constraints, but not meeting the strict  
266 criteria for primary sites, were placed into the 'secondary data set'. These  
267 samples are independent of the primary calibration data set and therefore  
268 can be used to assess the final calibrated parameters.

269 The calibration method, data set details including references, and the  
270 spallation calibration results for all nuclides are discussed in detail in Borchers  
271 et al. (2015). Additionally, some details of the  $^{10}\text{Be}$  and  $^{26}\text{Al}$  muon calibration  
272 can be found in Phillips et al. (2015) and the full chlorine-36 calibration can  
273 be found in Marrero (2012); Marrero et al. (2015).

El.	$A_i$	$\xi_i$	$\sigma_{sc,i}$	$\sigma_{th,i}$	$I_{\alpha,i}$	$S_i$	$Y_{n,i}^u$	$Y_{n,i}^{th}$	$K_m$	St.	#	$\mathbf{P}$
-	[g/mol]	[-]	[b]	[b]	[ $\times 10^{-24}$ ]	[-]	[-]	[-]	[-]	[-]	[-]	[-]
O	16	0.120004104	3.761	0.00019	0.0002693	539	0.23	0.079	0	0	8	1.00
H	1.01	1	20.49	0.3326	0	1542	0	0	0	0.5	1	0.00
C	12.01	0.157760474	4.74	0.0035	0.0018	573	0.45	0.18	13.691	2	6	0.36
Na	22.99	0.084543589	3.038	0.517	0.311	454	14.5	6.8	19.42	0.5	11	1.00
Mg	24.31	0.08009077	3.414	0.0666	0.038	463	5.8	2.6	14.94	1	12	0.93
Al	26.98	0.072337427	1.413	0.231	0.17	449	5.1	2.6	11.812	1.5	13	0.76
Si	28.09	0.069559975	2.044	0.171	0.082	455	0.69	0.335	10.01	2	14	0.84
P	30.97	0.063210393	3.134	0.165	0.079	444	0	0	8.48	2.5	15	1.04
K	39.1	0.050295528	2.04	2.1	1	432	0.45	0.305	12.78	0.5	19	1.54
Ca	40.08	0.049086179	2.93	0.43	0.233	436	0	0	10.73	1	20	1.90
Ti	47.87	0.041208508	4.09	6.41	3.1	367	0	0	7.53	2	22	2.66
Mn	54.94	0.035968204	2.06	13.36	13.4	351	0	0	8.486	1	25	2.73
Fe	55.85	0.035390922	11.35	2.56	1.36	353	0.19	0.205	7.54	1.5	26	3.28
Cl	35.45	0.055371497	15.8	33.14	13.83	420	0	0	16.98	0	17	1.32
B	10.81	0.174236264	4.27	767	343	537	62.3	19.2	55.68	0	5	0.25
Sm	150.36	0.013242694	38	9640	1400	0	0	0	4.004	0	62	4.4
G	157.25	0.012664667	172	41560	390	0	0	0	3.828	0	64	5.8
U	238.03	0.008378873	9.08	2.68	277	0	0	0	2.529	0	92	4.7
Th	232.04	0.008594581	13.55	7.34	83.3	0	0	0	2.594	0	90	3.0
Li	6.9	0.264	0.95	70.5	0.0	548	21.1	9.6	86.731	0.0	3	0.18
Cr	52.0	0.038	3.38	3.1	1.6	0.0	0.0	0.0	11.578	0.0	24	2.98

Table 1: Table of constants used for elemental parameters. The table was originally taken out of Fabryka-Martin (1988). It has been updated using Mughabghab (2006). El is the element; St is the stoichiometry. Note: 1 barn (b)= $1 \times 10^{-24}$ cm<sup>2</sup>. The columns correspond to the following parameters:  $A_i$  - Atomic weight of element;  $\xi_i$  - Average log decrement of energy per neutron collision with element i;  $\sigma_{sc,i}$  - Neutron scattering cross-section of element i;  $\sigma_{th,i}$  - Thermal neutron absorption cross-section of element i;  $I_{\alpha,i}$  - Dilute resonance integral for element i;  $S_i$  - Mass stopping power of element i for alpha particles of a given energy;  $Y_{n,i}^u$  - neutron yield of element i per ppm U in radioequilibrium;  $Y_{n,i}^{th}$  - Neutron yield of element i per ppm Th in radioequilibrium;  $K_m$  - 602/atomic weight of sample, used to convert to at/g from ppm; St. - Stoichiometric ratio of oxide (oxygen to element i); # - Atomic number;  $\mathbf{P}$  - Average capture probability relative to oxygen.

274 *2.3. Production Rate Scaling*

275     Cosmogenic nuclide scaling applies the physics governing the modulation  
276 of the cosmic-ray flux by atmospheric mass and the terrestrial and solar  
277 magnetic fields to provide production rates as a function of location and ex-  
278 posure time. Numerous scaling frameworks have been proposed in order to  
279 correct for latitude, elevation, atmospheric pressure anomalies, dipole and  
280 non-dipole geomagnetic field changes, and solar modulation. CRONUScale  
281 implements seven scaling frameworks, as summarized in Table 2. This in-  
282 cludes the original model by Lal (1991), further developed by Stone (2000)  
283 (referred to as St), that was based on cosmic-ray emulsion data and some  
284 neutron monitor data. A version of the Lal/Stone scaling accounting for ge-  
285 omagnetic field variations is also included (Lm). CRONUScale includes the  
286 neutron-monitor-based models of Dunai (Du) (Dunai, 2000, 2001a), Lifton  
287 (Li) (Lifton et al., 2005), and Desilets (De) (Desilets & Zreda, 2003; Desilets  
288 et al., 2006b). Finally, CRONUScale implements two new models based on  
289 Lifton et al. (2014). The Lifton-Sato-Dunai (LSD, denoted SF herein) scaling  
290 framework (Lifton et al., 2014) does not rely on empirical fitting to a set of  
291 measured data points, but instead is based on analytical fits to physics-based  
292 modeling, and has been tested against measured atmospheric secondary nu-  
293 cleon and muon energy spectra.

294     The energy spectrum of the cosmic-ray flux produced by the LSD frame-  
295 work provides information that is available neither from the traditional Lal  
296 (St) scaling, nor neutron-monitor based scaling (Du, Li, De). This, in turn,  
297 allows the production rates of cosmogenic nuclides to be calculated by inte-  
298 grating the energy-dependent excitation function with the calculated particle  
299 energy spectrum. This is termed “nuclide-dependent scaling” because it re-  
300 sults in a separate scaling factor for each nuclide, rather than a single scaling  
301 factor applicable to all nuclides, as the previous methods did. In the case of  
302  $^{36}\text{Cl}$ , for example, this results in six nuclide-dependent scaling factors, includ-  
303 ing four high-energy scaling factors to scale the spallation reactions (K, Ca,  
304 Ti, and Fe) and one generalized spallation reaction to scale the low-energy  
305 reactions. Due to the derivation from the high-energy flux, the low-energy  
306 pathways cannot be scaled using the incoming low-energy neutron flux. (Note  
307 that since  $^{36}\text{Cl}$  is commonly measured in rocks of varying compositions, each  
308 reaction has to be individually weighted by the concentration of the target  
309 element in the rock, unlike nuclides such as  $^{10}\text{Be}$  or  $^{26}\text{Al}$  that are commonly  
310 measured in minerals of constant composition, such as quartz). In all of the  
311 other scaling frameworks, the nuclide-dependent scaling factors still appear in

312 the code, but all are set equal to the single scaling factor produced by the se-  
313 lected scaling framework. This nuclide-dependent scaling framework (LSDn,  
314 denoted SA herein) is the default on the online interface due to its favorable  
315 calibration results (see Borchers et al. 2015) and the possibility for future  
316 incorporation of updates to the excitation functions and other physics-based  
317 research. For all the details of the scaling frameworks themselves, please see  
318 the original papers (cited in Table 2); for details of implementation, please  
319 see the description in Balco et al. (2008) and Lifton et al. (2014).

320 In CRONUScalc, the geomagnetic history is consistent across all scaling  
321 frameworks, even though each model uses the history in a slightly differ-  
322 ent manner. This information is available in the code and can be modified  
323 directly if a different geomagnetic history is necessary. References for the  
324 currently implemented geomagnetic history can be found in Table 3, with  
325 relevant details in Lifton et al. (2014). The calculator is flexible, allowing  
326 knowledgeable users to modify the code to incorporate alternative geomag-  
327 netic models.

328 Although the various paleomagnetic reconstructions are in broad agree-  
329 ment, there are considerable differences for certain time intervals, indicating  
330 some uncertainty with regard to the accuracy of each reconstruction. In  
331 addition, each reconstruction contains internal uncertainties stemming from  
332 uncertainties in the measurements and chronology. We do not attempt to  
333 propagate these uncertainties into the CRONUScalc ages. This is partly due  
334 to the difficulty of quantifying the unknown errors in each reconstruction  
335 (for example, the assumed constant geomagnetic field of the St model is also  
336 clearly in error, but how does one quantify the magnitude and propagate it  
337 into the resultant age?). When considering the entire CRONUS-Earth sec-  
338 ondary calibration data set (Borchers et al., 2015), the difference between  
339 the average normalized Lal-Stone (St; constant geomagnetic field) ages and  
340 the Lal (1991) (Lm; time-varying field) ages is only 0.4%, and increases to  
341 1.8% for the same comparison at the high-elevation, low-latitude Breque,  
342 Peru, site. However, due to the approximately sinusoidal dipole variation  
343 over the exposure time of a significant number of the calibration sites, these  
344 comparisons may still underestimate the differences when sample exposure is  
345 integrated over longer time spans in which the time-integrated effects might  
346 not cancel (<ca. 100 ka). Considering the difficulty of quantifying this un-  
347 certainty and propagating it, and the minimal effect the effort would have  
348 on age uncertainties for a majority of samples, we have neglected it. We  
349 acknowledge that for older or younger samples especially at low latitude, the

<b>Abbr.</b>	<b>Reference</b>	<b>Description</b>
St	Lal (1991); Stone (2000)	Time-independent (constant production rate). Based on two different types of neutron reaction counting methods (photographic emulsions and neutron monitors). Scaling factor inputs are geographic latitude and atmospheric pressure, based on the Stone (2000) modification.
Lm	Lal (1991); Nishiizumi et al. (1989)	Time-dependent version of St based on time-variation in the dipole magnetic field intensity, as formulated by Nishiizumi et al. (1989).
Li	Lifton et al. (2005, 2008)	Time-dependent model based on neutron monitor measurements and incorporating dipole and non-dipole magnetic field fluctuations and solar modulation. The scaling factor is based on actual atmospheric pressure, solar modulation, and a cutoff rigidity calculated using trajectory tracing.
Du	Dunai (2000, 2001a,b)	Time-dependent model based on neutron monitor measurements and incorporating dipole and non-dipole magnetic field fluctuations. The scaling factor is based on an analytically calculated cutoff rigidity and atmospheric pressure. A long-term mean for solar modulation is used in this model.
De	Desilets et al. (2006b); Desilets & Zreda (2003)	Time-dependent model based on neutron monitor measurements and incorporating dipole and non-dipole magnetic field fluctuations. The scaling factor is based on a cutoff rigidity calculated using trajectory tracing and the actual atmospheric pressure.
LSD (Sf)	Lifton et al. (2014)	Time-dependent model based on equations from a nuclear physics model and incorporating dipole and non-dipole magnetic field fluctuations and solar modulation. The scaling factor is based on actual atmospheric pressure, solar modulation, and a cutoff rigidity calculated using trajectory tracing. The total flux (protons+neutrons) is used to scale all reactions.
LSDn (Sa)	Lifton et al. (2014)	Time-dependent model based on equations from a nuclear physics model and incorporating dipole and non-dipole magnetic field fluctuations and solar modulation. The scaling factor is based on actual atmospheric pressure, solar modulation, and a cutoff rigidity calculated using trajectory tracing. Nuclide-dependent scaling is implemented by incorporating cross-sections for the different reactions.

Table 2: Table of scaling frameworks, including abbreviations, original references, and a brief description of each model.

Time period (kyr)	Model name	Reference
3-7ka	CALS7k	Korte & Constable (2005)
7-18ka	GLOPIS-75	Laj et al. (2004)
18ka-2Ma	PADM2M	Ziegler et al. (2011)

Table 3: Geomagnetic history used in all the scaling frameworks.

350 effect might be larger and we hope that quantification will be addressed in  
351 future research. The geomagnetic models used may also include systematic  
352 spatial or temporal biases that may be resolved with further research.

353 While CRONUScalc offers seven different spallation scaling frameworks,  
354 it uses only one muon scaling model. Muons were not natively scaled in any  
355 of the original models, so we use the energy-dependent Lifton et al. (2014)  
356 muon model to scale the muon flux.

357 A new input to the code is the “year collected” that allows the scaling  
358 frameworks to more precisely account for the time of exposure. In previous  
359 calibrations, the independent age constraints have been listed as “before  
360 present.” For radiocarbon analyses, this is actually “years before 1950.”  
361 The calibrations have been updated accordingly and now list independent  
362 ages as “years before 2010” and the exposure age calculation routines in  
363 CRONUScalc now integrate production through the collection year. For  
364 most samples, this is not a critical change, but with the advent of very high-  
365 precision cosmogenic ages on very young samples (e.g. Schaefer et al. 2009), it  
366 will eliminate the need for ad-hoc corrections for sample date. This capability  
367 will only become more important through time. The sample is assumed to  
368 have been processed shortly after collection or to have been stored where  
369 continued production and decay would be insignificant.

#### 370 *2.4. Attenuation Length*

371 The apparent attenuation length, the attenuation length with respect to a  
372 flat surface with no topographic shielding, quantifies the depth distribution  
373 of the production by neutron spallation. When the apparent attenuation  
374 length is adjusted to account for the dip of the sample surface and any  
375 topographic shielding, the result is the effective attenuation length,  $\Lambda_{f,e}$ .  
376 The effective attenuation length is the parameter that should be used in  
377 calculations pertaining to production from a particular sample.

378 The effective attenuation length is an input parameter for each sample.  
379 The web-based user interface automatically calculates the effective attenua-

<b>Depth/Cut. Rig.</b>	<b>1100</b>	<b>1000</b>	<b>900</b>	<b>800</b>	<b>700</b>	<b>600</b>	<b>500</b>	<b>400</b>
<b>0</b>	151	152	153	154	155	158	163	172
<b>4</b>	152	152	154	156	159	164	171	185
<b>8</b>	156	159	161	164	168	175	185	204
<b>12</b>	162	165	168	171	176	184	196	218
<b>16</b>	168	170	172	177	182	191	204	228
<b>20</b>	169	171	174	179	184	192	206	231

Table 4: The table used for the interpolation of attenuation lengths based on the given atmospheric depth (top row, in units of  $\text{g}/\text{cm}^2$ ) and cutoff rigidity (first column, in units of GV). Values based on those obtained using the spreadsheet that accompanied Sato et al. (2008), but include the additional 11.1% correction discussed in the text.

380 tion length if it is not provided. For use in the raw code where attenuation  
381 length is not automatically calculated, there is a function (`attenuationlengthnormal.m`)  
382 to calculate the parameter at a given location (latitude, longitude, elevation)  
383 and pressure of a sample. The attenuation-length model in CRONUScalc is  
384 based on atmospheric attenuation lengths calculated from the PARMA model  
385 of Sato et al. (2008), which is an analytical model for estimating cosmic-ray  
386 spectra in the atmosphere. The attenuation lengths are interpolated from  
387 the values given in Table 4 using the vertical cutoff rigidity and atmospheric  
388 depth of the site.

389 The interpolated attenuation lengths have been adjusted upward by 11.1%  
390 to account for systematic differences between atmospheric and lithospheric  
391 attenuation. This adjustment is based on the approximate relation:

$$\frac{\lambda_{f,rock}}{\lambda_{f,atm}} = \left(\frac{A_{rock}}{A_{atm}}\right)^{1/3} \quad (5)$$

392 where  $A_{rock}$  and  $A_{atm}$  are the average atomic weights of the rock and  
393 atmosphere, respectively. The average atomic weight of the atmosphere was  
394 taken to be  $14.68 \text{ g mole}^{-1}$  and that of average rock  $20.40 \text{ g mole}^{-1}$ . (We note  
395 that any changes in the chemical composition of the atmosphere over the time  
396 scale of interest for application of cosmogenic-nuclide surface chronology are  
397 too small to affect the attenuation length.) This relation is derived from the  
398 following simple considerations.

399 The macroscopic cross-sectional area of the atoms in a gram of matter  
400 scales as the product of the number of atoms of each element in the volume

401 multiplied by the average cross-sectional area of the atoms. Assuming that  
 402 atomic nuclei are spheres of constant density, and that each nucleus is made  
 403 up of spheres of uniform mass and diameter (protons and neutrons), the  
 404 radius of each atom will scale by the atomic weight to the one-third power  
 405 (Friedlander et al., 1981). The cross-sectional area will then scale as the  
 406 square of the radius. The product of these is the average atomic cross-  
 407 section to the two-thirds power. The number of atoms per gram will scale  
 408 by Avogadro’s number divided by the average atomic weight. Therefore,  
 409 the macroscopic cross-sectional area of substance *i* (rock or atmosphere), per  
 410 gram, will scale as follows:

$$Area_i \propto \frac{N_A A_i^{2/3}}{A_i} = \frac{N_A}{A_i^{1/3}} \quad (6)$$

411 where  $N_A$  is Avogadro’s number. The apparent attenuation length is the  
 412 inverse of the macroscopic area per gram. When the ratios of the attenuation  
 413 lengths for rock and atmosphere are taken, Equation 5 results. (John Stone,  
 414 personal communication, 14 February 2012).

415 The attenuation length will also vary as a function of lithology. The  
 416 average atomic weight of common lithologies varies from 19.8 g mole<sup>-1</sup> for  
 417 quartzite to 21.5 g mole<sup>-1</sup> for ultramafic rocks. However, the maximum  
 418 difference between the attenuation length calculated for any lithology and  
 419 that for the mean atomic weight (averaged over all lithologies) is <2 %.  
 420 This is insignificant and hence CRONUScalc does not compute attenuation  
 421 lengths on a lithology-specific basis. There is some modeling evidence to  
 422 suggest that nuclide-dependent attenuation lengths may be needed in the  
 423 future (Argento et al., 2014), something the calculator is already equipped  
 424 to accommodate because attenuation length is a sample input.

425 Figure 1 shows the dependence of the modeled effective attenuation length  
 426 on elevation and latitude. For samples with large topographic shielding cor-  
 427 rections, these values should be adjusted to account for horizon obstructions.

428 The final attenuation lengths overlap with the range of values presented  
 429 by Dunai (2000) from 121 to >170 g/cm<sup>2</sup>, with the range for most samples  
 430 falling between 150-190 g/cm<sup>2</sup> (see Figure 1). Although the results are in the  
 431 same range as commonly assumed values of 160-170 g cm<sup>-2</sup> (Gosse & Phillips,  
 432 2001; Dunai, 2010), a significant difference in age between the use of the two  
 433 different attenuation lengths (CRONUS-predicted value vs 170 g cm<sup>-2</sup>) is  
 434 possible for samples with high erosion rate, very long exposure times, or at



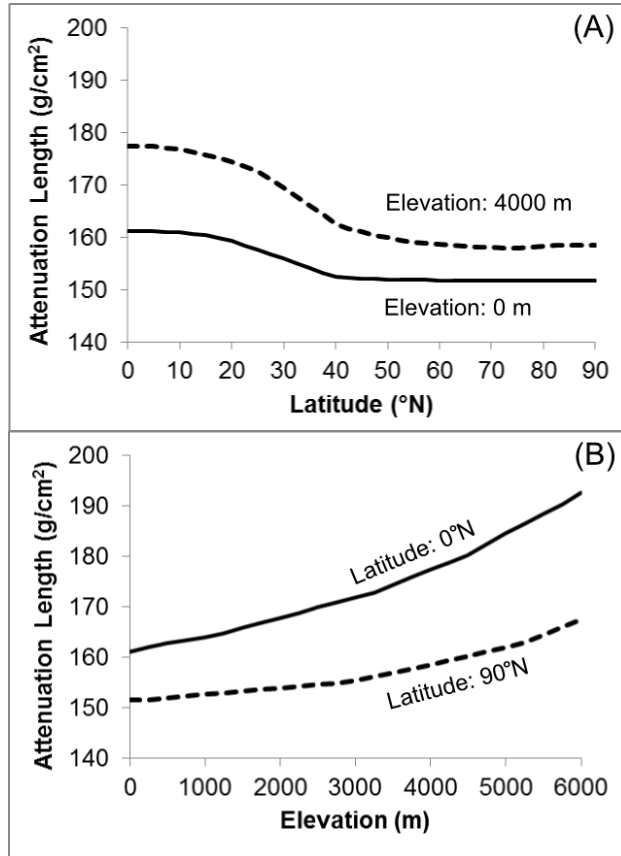


Figure 1: The change in effective attenuation length for a flat surface at various elevations (A), shown for both zero and 90°N latitude, and effective attenuation length at various latitudes (B), shown for elevations of 0 and 4000 m.

435 significant depth. In order to test the magnitude of this effect, we predicted  
436  $^{10}\text{Be}$  concentrations using the CRONUScalc modeled attenuation length of  
437  $153 \text{ g/cm}^2$  (corresponding to  $40^\circ\text{N}$  at sea level) for artificial samples for a  
438 range of ages and erosion rates. The resulting ages were then determined  
439 using an attenuation length of  $170 \text{ g/cm}^2$ . The results (Figure 2, B.6) show  
440 that the attenuation length change from  $153 \text{ g/cm}^2$  to  $170 \text{ g/cm}^2$  results in  
441 up to a 2% difference on the 20 ka age for erosion rates up to 10 mm/kyr.  
442 The difference is considerably larger for faster eroding samples with longer  
443 exposure times, or alternately samples at depth, with differences of almost  
444 50 % for 300 ka exposure times with erosion rates of 10 mm/kyr. However,  
445 for most surface samples with modest or low erosion rates, this difference is  
446 relatively small. When depth profiles are available, the attenuation length  
447 should still be one of the fitted parameters to ensure the most accurate value  
448 (e.g. Braucher et al. 2013). Use of the surface shielding calculator to estimate  
449 attenuation lengths for depth profiles or very high erosion rates should be  
450 approached with caution.

451 Given the physics-based derivation of the new attenuation length model,  
452 the new attenuation lengths are implemented as the default in the online  
453 calculator interface. However, as this parameter is an input for each sample,  
454 the choice of attenuation length is ultimately left to the user. The final model  
455 for attenuation length is included as its own function in the code repository  
456 (see the Function Appendix in the supplementary materials). A separate  
457 shielding calculator has been developed to simplify the calculation of the  
458 topographic shielding factor as well as the appropriate effective attenuation  
459 length. The attenuation length model accounts for the latitude and elevation  
460 of a sample. If shielding information is included, the effective attenuation  
461 length is modified accordingly. A link to the shielding calculator is available  
462 on the calculators homepage (<http://web1.ittc.ku.edu:8888/>).

### 463 *2.5. Accumulation*

464 Instantaneous production rates, such as those described above, must be  
465 integrated in both time and thickness in order to calculate the production  
466 in a real sample. In many common solutions, this is done analytically or  
467 with additional multiplicative factors to account for the finite thickness of  
468 a sample. In the CRONUScalc program, this integration is done numeri-  
469 cally, which is more accurate for depth integrations and makes it simple to  
470 incorporate time-dependent scaling and varying production rates.

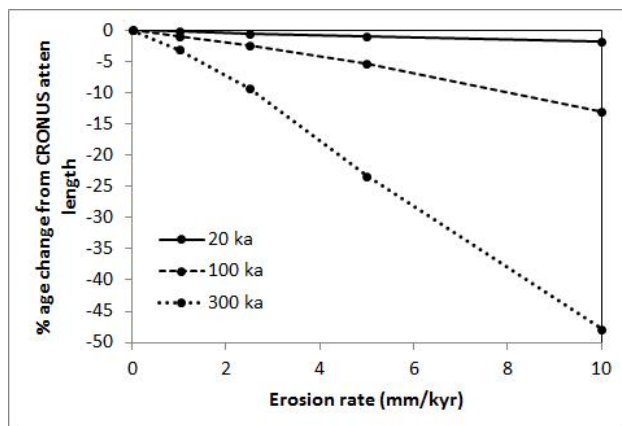


Figure 2: Change in ages due to change in attenuation length from the original CRONUS-calculated value ( $153 \text{ g/cm}^2$ ) to  $170 \text{ g/cm}^2$ , compared over a range of erosion rates (0, 1, 2.5, 5, and 10 mm/kyr) and three different exposure ages (20, 100, and 300 ka).

471 For a given age, an appropriate time step,  $\Delta t$ , is found such that the  
 472 erosion rate is small for that period and the changes in time-dependent pro-  
 473 duction rates are not too large. Although larger time steps may be appropri-  
 474 ate for some samples or scaling methods, the time step default is set to 100  
 475 years in order to maintain time-step errors below 0.4% for all sample types,  
 476 as calculated assuming the correct age is the age produced using a time step  
 477 of 1 year.

478 The sample begins at depth and the cosmogenic inventory within the  
 479 sample is tracked during its migration to the surface. For each time step, the  
 480 current scaling factors and production rates are found for the sample. The  
 481 inventory accounts for the decay of all previously produced nuclide inventory  
 482 (the first term in Equation 7) as well as the production and decay of the  
 483 nuclide during the current time step (second term in Equation 7).

$$N_{tot} = N_{prev}e^{-\lambda\Delta t} + P_{tot} * f_{decay} \quad (7)$$

484 where  $N_{tot}$  is the total inventory in the sample up to the current time step;  
 485  $N_{prev}$  is the inventory from all previous time steps;  $\lambda$  is the decay constant  
 486 for the nuclide;  $P_{tot}$  is the instantaneous production rate of the nuclide from  
 487 all mechanisms; and  $f_{decay}$  is the decay factor (Equation 8) that accounts for  
 488 the fact that a small amount of the nuclide produced at the beginning of the

489 time period will have decayed by the end of the period.

$$f_{decay} = \frac{1 - e^{-\lambda\Delta t}}{\lambda} \quad (8)$$

490 After the nuclide is produced, the samples are “eroded” by updating the  
491 depths for the sample by using the erosion rate and the time step, as shown  
492 in Equation 9.

$$D_{new} = D_{previous} - \Delta t * \epsilon \quad (9)$$

493 where  $D_{new}$  is the new depth,  $D_{prev}$  is the previous sample depth, and  $\epsilon$   
494 is the erosion rate of the surface.

495 These steps are repeated from  $t=(\text{year sampled})\text{-age}$ , with the sample at  
496 depth, until  $t$  is equal to the year sampled, when the sample reaches the  
497 surface. The inventory is then returned by the module and used in any  
498 number of other functions, such as surface or depth-profile calculators, or  
499 simply returned to the user.

### 500 3. Considerations Specific to Individual Cosmogenic Nuclides

501 While the in-situ cosmogenic nuclides share many similarities in terms of  
502 production pathways, they are each produced by a different combination of  
503 pathways and there are other individual issues that need to be addressed.  
504 In the following sections, the specific pathways for production, uncertainties,  
505 and other issues are documented for each of the major four code modules  
506 representing five nuclides.

507 Each nuclide is produced by one or more of the pathways discussed in  
508 the previous section. The most common reactions are shown in Table 5 for  
509 common nuclides and their common target minerals.

510 Inputs required by CRONUScalc vary, but the inputs common to all nu-  
511 clides include location (latitude, longitude, elevation/pressure), sample pa-  
512 rameters (thickness, bulk density, depth, and attenuation length), site pa-  
513 rameters (topographic shielding, erosion rate, year collected), and chemical  
514 parameters (cosmogenic nuclide concentration). Additional inputs are neces-  
515 sary for some nuclides to account for production through low-energy neutron  
516 pathways (composition, water content). For all nuclides, the required cosmo-  
517 genic nuclide concentration is assumed to incorporate any blank corrections,  
518 as these vary from lab to lab and therefore cannot be standardized to be  
519 included in the program.

Nuclide	Reaction
$^3\text{He}$	Spallation: O, Mg, Si, Ca, Fe, Al $^6\text{Li}(n,\alpha)^3\text{He}$
$^{10}\text{Be}$	$^{16}\text{O}(n,4p3n)^{10}\text{Be}$ $^{28}\text{Si}(n,x)^{10}\text{Be}$ $^{16}\text{O}(\mu^-, \alpha pn)^{10}\text{Be}$ $^{28}\text{Si}(\mu^-, x)^{10}\text{Be}$
$^{14}\text{C}$	$^{16}\text{O}(\mu^-, 2p)^{14}\text{C}$ $^{16}\text{O}(n, 2pn)^{14}\text{C}$ $^{17}\text{O}(n, \alpha)^{14}\text{C}$ $^{28}\text{Si}(n, x)^{14}\text{C}$
$^{26}\text{Al}$	$^{28}\text{Si}(n, 2pn)^{26}\text{Al}$ $^{28}\text{Si}(\mu^-, 2n)^{26}\text{Al}$
$^{36}\text{Cl}$	$^{40}\text{Ca}(n, 2n3p)^{36}\text{Cl}$ $^{39}\text{K}(\mu^-, p2n)^{36}\text{Cl}$ $^{40}\text{Ca}(\mu^-, \alpha)^{36}\text{Cl}$ $^{35}\text{Cl}(n, \gamma)^{36}\text{Cl}$ $^{39}\text{K}(n, \alpha)^{36}\text{Cl}$ $\text{Fe}(n, x)^{36}\text{Cl}$ $\text{Ti}(n, x)^{36}\text{Cl}$

Table 5: Common reactions producing in-situ terrestrial cosmogenic nuclides (Gosse & Phillips, 2001). The symbolism is as follows for the X(a,b)Y reaction: X is the target element, a is the particle interacting with the target, b is emitted during the reaction, and Y is the final nuclide product. "x" in the second place inside the parentheses indicates a reaction for which several different combinations of emitted particles are possible. Reactions are only shown for the pathways discussed in the paper. For beryllium, aluminum, and carbon, only those reactions possible in a quartz target mineral are shown.

520 *3.1. Aluminum-26 and Beryllium-10*

521  $^{10}\text{Be}$  is the most commonly used cosmogenic nuclide.  $^{26}\text{Al}$  is also produced  
522 in quartz and is commonly processed in the same samples as  $^{10}\text{Be}$ . Both nu-  
523 clides are produced in quartz through only two mechanisms: spallation and  
524 muogenic production. Muogenic production of  $^{10}\text{Be}$  and  $^{26}\text{Al}$  accounts for  
525 only  $\sim 1.5\%$  and  $\sim 2\%$  of total surface SLHL production, respectively, as cal-  
526 culated using CRONUScalc. CRONUScalc employs the currently accepted  
527 half-life and AMS standard values for  $^{10}\text{Be}$  (Nishiizumi et al., 2007; Ko-  
528 rschinek et al., 2010; Chmeleff et al., 2010). The online interface performs  
529 automatic renormalization for all  $^{10}\text{Be}$  and  $^{26}\text{Al}$  concentrations based on the  
530 standards selected by the user. The interface passes this information to the  
531 underlying raw CRONUScalc program, which assumes the concentration is  
532 normalized to 07KNSTD for  $^{10}\text{Be}$  and KNSTD for  $^{26}\text{Al}$ . For discussions con-  
533 cerning these normalizations, see Balco et al. (2008) and Nishiizumi et al.  
534 (2007).

535 When  $^{26}\text{Al}$  and  $^{10}\text{Be}$  are both being analyzed for a particular sample, they  
536 can be processed in the same quartz split. The code operates in a fashion  
537 similar to that of Balco et al. (2008) in that it allows any given sample to  
538 be associated with data from either  $^{10}\text{Be}$  or  $^{26}\text{Al}$ , or both nuclides. The  
539 production rates for both nuclides have only been determined reliably in  
540 quartz, so this is the only mineral target supported by CRONUScalc at this  
541 time.

542 Additional information, such as erosion rate or burial history, can be  
543 determined if more than one nuclide is analyzed in a sample (Bierman, 1994;  
544 Granger & Muzikar, 2001). The common Al/Be pair is frequently used for  
545 these investigations. CRONUScalc does not currently provide figures for the  
546 paired interpretation if  $^{10}\text{Be}$  and  $^{26}\text{Al}$ , but these capabilities could be added  
547 by an advanced user following the method described in Granger & Muzikar  
548 (2001); Granger (2006).

549 For information on the production rates used in the calculator, see the  
550 CRONUS-Earth spallation production rate calibration paper (Borchers et al.,  
551 2015) or the summary paper (Phillips et al., 2015).

552 *3.2. Chlorine-36*

553 Cosmogenic  $^{36}\text{Cl}$  is produced by a wide range of pathways that have been  
554 discussed in the production systematics section. The main three pathways are  
555 spallation (Ca, K, Ti, Fe), low-energy neutron absorption (Cl), and muogenic  
556 production (Ca, K, Ti, Fe). Note that we include the production of  $^{36}\text{Cl}$

557 by relatively low-energy neutrons (down to approximately 3 MeV) by the  
558 reaction  $^{39}\text{K}(n,\alpha)^{36}\text{Cl}$  in the "spallation" category, using the cross-section of  
559 Reedy (2013), since this energy is still well above the epithermal level.

560 Previous studies have resulted in production-rate estimates that differ  
561 from each other by up to 40%. One goal of the CRONUS-Earth project  
562 was to resolve these uncertainties (Marrero, 2012; Marrero et al., 2015, this  
563 volume, submitted). For spallation production rates, only CRONUS-Earth  
564 mineral separate data is used in the calibration and the resulting production  
565 rates fit the independent secondary data set very well (see evaluation of the  
566 secondary  $^{36}\text{Cl}$  data set in Borchers et al. (2015)). For the low-energy neu-  
567 tron production pathway, however, there are additional unknown complicat-  
568 ing factors, potentially water content or other site-specific parameters, which  
569 influenced the  $P_f(0)$  calibration. A more complete discussion of calibration  
570 results and factors affecting  $^{36}\text{Cl}$  production can be found in Marrero et al.  
571 (2015), but the resulting value for  $P_f(0)$  fits the secondary data set well and  
572 is used in CRONUScalc until additional  $^{36}\text{Cl}$  calibrations can be performed.  
573 The  $P_f(0)$  value that was obtained during the CRONUS-Earth calibration  
574 has a larger uncertainty (about 20%) than the other  $^{36}\text{Cl}$  production param-  
575 eters. Ideally,  $^{36}\text{Cl}$  should be measured on low-chlorine mineral separates to  
576 eliminate the uncertainty associated with this pathway (cf. Schimmelpfennig  
577 et al. 2009). Analysis of low-chlorine mineral separates should help to keep  
578  $^{36}\text{Cl}$  ages to a similar level of uncertainty as other nuclides.

579 It is important to note that the predicted nuclide concentrations are more  
580 sensitive to certain parameters than others. For example, hydrogen is the  
581 most effective moderator of neutron energy (Fabryka-Martin, 1988), and thus  
582 the amount of water in a sample can strongly affect the magnitude of the  
583 low-energy neutron flux and consequently influence the production of  $^{36}\text{Cl}$   
584 through the low-energy pathway. The importance of water was evaluated  
585 theoretically by Dep et al. (1994) and experimentally substantiated by Dunai  
586 et al. (2014), indicating that the presence of hydrogen can significantly influ-  
587 ence production. There is some evidence to indicate that the water content  
588 of the surrounding landscape may also affect the low-energy neutron flux  
589 (Zreda et al., 2008). The sensitivity of sample age to water in the current  
590 calculator is included in the sensitivity study in Section 5.2.

591 Chlorine-36 dating requires compositional parameters that most cosmo-  
592 genic nuclides do not. The code allows for the input of both "mineral target"  
593 and "bulk-rock" compositions. The bulk-rock analysis permits the calcula-  
594 tion of the neutron-transport parameters. If a mineral separate has been used

595 for the analysis, the target-element concentrations (comprehensively, K, Ca,  
596 Ti, Fe, and Cl) are also needed for the sample on which the measurement  
597 was performed. The bulk-rock composition includes data on trace-elements,  
598 such as boron and uranium, that are needed for the appropriate calculation  
599 of neutron-absorption properties of the rock and radiogenic subtraction. For  
600 samples with low Cl content and high concentrations of K and/or Ca, the  
601 full range of trace element analyses may be superfluous. Given a complete  
602 analysis of a rock sample, CRONUScalc calculates the percentage of the pro-  
603 duction originating from low-energy neutron absorption by Cl, spallation on  
604 Ca and K, and muons. This can be used to determine whether chemical  
605 analysis of elements that modulate the low-energy neutron flux are needed  
606 for every sample.

607 Isotope Dilution Mass Spectrometry (IDMS) is a standard method for  
608 highly accurate elemental and isotopic analysis. In cosmogenic-nuclide ap-  
609 plications it is commonly used for analysis of  $^{36}\text{Cl}$  and elemental Cl. The  
610 process includes adding a “spike” of known isotope ratio that has been en-  
611 riched in one of the stable chlorine isotopes, either  $^{35}\text{Cl}$  or  $^{37}\text{Cl}$ . In either case,  
612 the ratios of  $^{36}\text{Cl}/^{35}\text{Cl}$  and  $^{35}\text{Cl}/^{37}\text{Cl}$  are measured by the accelerator mass  
613 spectrometer. The stable chloride concentration and the  $^{36}\text{Cl}$  concentration  
614 of the rock can both be back-calculated using the ratios from the accelerator  
615 and the recorded spike and sample masses from sample preparation. The  
616 process is described in detail in Desilets et al. (2006a).

617 When using IDMS for chlorine, there is a correlation between the uncer-  
618 tainties in stable chloride concentration and the uncertainties on  $^{36}\text{Cl}$  con-  
619 centration because they both depend on the same isotope ratios. In order to  
620 produce the correct uncertainties from raw laboratory results, a set of addi-  
621 tional codes were created to handle this calculation. This code is external  
622 to the main CRONUScalc program, but is distributed with the code. It is  
623 designed to assist the user in calculating the correct concentrations of  $^{36}\text{Cl}$   
624 and Cl and correctly assigning their uncertainties for samples reported as  
625  $^{36}\text{Cl}/\text{total Cl}$  and  $^{35}\text{Cl}/^{37}\text{Cl}$  by AMS. A linearized uncertainty method was  
626 used to calculate the stable chlorine concentration (`spiketoconc.m`). How-  
627 ever, the traditional error propagation does not work for low-Cl samples due  
628 to the non-linear response in this range, so uncertainties are calculated using  
629 a Monte Carlo method (`spiketoconcmc.m`). In the Monte Carlo code, the  
630 uncertainty in the stable chlorine concentration is calculated 10,000 times us-  
631 ing the nominal inputs (spike mass, sample mass, spike concentration, etc.)  
632 and a random uncertainty. The random quantity added to the nominal value



633 of the parameter is normally distributed with a mean of 0 and standard de-  
634 viation equal to the uncertainty in the parameter. For samples with high  
635 chlorine concentrations, the Monte Carlo result is essentially the same as the  
636 linearized approximations; however, at low chlorine concentrations, the un-  
637 certainties can be a significant percentage of the total concentration (>90%).

### 638 3.3. Carbon-14

639 Production of in-situ cosmogenic  $^{14}\text{C}$  is primarily from the spallation of  
640 oxygen, but also other elements including Mg, Al, and Si (Dunai, 2010).  
641 Unlike  $^{10}\text{Be}$ , muons contribute significantly (15-20%) to the cosmogenic pro-  
642 duction at the surface and increasingly at depth. Quartz is the only mineral  
643 phase in which  $^{14}\text{C}$  is commonly measured, although it is possible to measure  
644 it in other minerals as well (Handwerger et al., 1999; Dunai, 2010). Carbon-  
645 14 has a short half-life and therefore reaches secular equilibrium between  
646 production and decay relatively quickly ( $\sim 25\text{-}30$  kyr) (Lifton et al., 2001).  
647 Due to these factors,  $^{14}\text{C}$  is well-suited for short-term erosion rate studies  
648 using multiple nuclides and young burial-history studies (Dunai, 2010).

649 In situ  $^{14}\text{C}$  is extracted from quartz typically by stepped combustion/ dis-  
650 solution (e.g. Lifton et al., 2001; Pigati et al., 2010; Goehring et al., 2014) or  
651 stepped combustion (Hippe et al., 2014). Reproducibility of intercomparison  
652 materials is typically ca. 5% among labs (Jull et al., 2013), but occasional  
653 discrepancies on replicate analyses have been as much as 5-10% in the past  
654 (Borchers et al. 2015). As a result, in situ  $^{14}\text{C}$  production rates have tended  
655 to exhibit somewhat greater uncertainties than other nuclides, although the  
656 situation is improving as extraction techniques continue to advance.

657 In CRONUScalc, only the production of  $^{14}\text{C}$  in quartz by spallation and  
658 by muons is available. This should provide adequate functionality for the  
659 majority of  $^{14}\text{C}$  users. For information on the  $^{14}\text{C}$  production rates used in  
660 the calculator, see the CRONUS-Earth spallation production rate calibration  
661 paper (Borchers et al., 2015).

### 662 3.4. Helium-3

663 Cosmogenic  $^3\text{He}$  is produced primarily by spallation reactions on most  
664 elements present in a rock (Mg, Si, Fe), but also through low-energy neutron  
665 absorption by lithium (Li) (Dunai et al., 2007). Moderate amounts of Li  
666 (50-200 ppm) can cause a significant amount of production to originate from  
667 cosmogenic thermal neutrons, affecting neighboring (and potentially Li-free)  
668 mineral phases (Dunai et al., 2007). Even in relatively low-Li samples (1

669 ppm), radiogenic production can be important in rocks where the formation  
670 age of the rock is much greater than the exposure age of the sample (Lal,  
671 1987; Farley et al., 2006; Dunai et al., 2007). There is currently no evidence  
672 of significant contribution to production via muon reactions (Kurz, 1986;  
673 Dunai, 2010). The most commonly used minerals are pyroxene and olivine,  
674 however  $^3\text{He}$  has been measured in other mineral phases (e.g. apatite, zircon,  
675 biotite, titanite, kyanite, and hornblende) (Amidon & Farley, 2012; Amidon  
676 et al., 2009; Amidon & Farley, 2010; Farley et al., 2006; Amidon et al., 2008).

677 When evaluating  $^3\text{He}$  data, the inherited (magmatic) component must  
678 be subtracted from the measured concentration in order to include only the  
679 cosmogenically produced  $^3\text{He}$  in the dating. This is done through methods  
680 that vary by lab (Kurz, 1986; Cerling, 1990; Blard & Pik, 2008; Blard &  
681 Farley, 2008; Williams et al., 2005). The input needed for CRONUScalc is the  
682 cosmogenic concentration of  $^3\text{He}$  in units of atoms per gram. CRONUScalc  
683 assumes that any corrections for blanks or inherited component have already  
684 been performed.

685 Currently, CRONUScalc only incorporates spallation production for  $^3\text{He}$ .  
686 The spallation production rate is currently calibrated from a combined data  
687 set consisting of olivine and pyroxene samples from the compilation by Goehring  
688 et al. (2010b). The publication includes both official CRONUS data and  
689 high-quality external data sets. Individual sites were determined to be either  
690 primary or secondary data sets based on quality of the independent age con-  
691 trol and other site parameters. For information on the  $^3\text{He}$  calibration, see  
692 Borchers et al. (2015).

693 Recommended use of the calculator is currently limited to olivine and  
694 pyroxene due to the limitations of the calibration data set. For pyroxene  
695 and olivine derived from basalt and xenoliths, Li concentrations are typically  
696 very low (<5 ppm) so the presence of cosmogenic or radiogenic  $^3\text{He}$  from  
697 low-energy neutrons should be negligible (Dunai et al., 2007). The lithium  
698 low-energy pathway needs to be considered for minerals in rocks that are  
699 more evolved than primitive basalts and generally for rocks whose geological  
700 age is much larger than the exposure age (Dunai et al., 2007; Lal, 1987).  
701 Until this pathway is incorporated into the program, users are cautioned to  
702 limit the use to low-Li samples.

703 The calculation of the low-energy production pathway is complicated by  
704 the large number of additional parameters that would be needed (e.g. grain  
705 size of target minerals, complete major and trace element composition of  
706 the host rock, water content) (Dunai et al., 2007). The calculator is already

707 designed to take the mineral phase as an input and a thermal neutron com-  
708 ponent could be added by adapting the low-energy production calculations  
709 already in place for  $^{36}\text{Cl}$ . This would increase the applicability of CRONUS-  
710 calc to helium samples with higher Li contents and ultimately allow inclusion  
711 of other mineralogies.

## 712 4. CRONUScalc Calculators

713 The program written to perform a range of cosmogenic nuclide calcu-  
714 lations is named "CRONUScalc." It is written in the MATLAB program-  
715 ming language, but can also be run under open-source Octave. The pro-  
716 gram is available under the GNU General Public License agreement and can  
717 be accessed and downloaded at: [https://bitbucket.org/cronusearth/  
718 cronus-calc](https://bitbucket.org/cronusearth/cronus-calc). In the repository, users can upload their own files alongside  
719 the main code in order to share new features or functions using CRONUScalc.

720 The program is organized by scaling model, with folders containing code  
721 to perform various calculations. The core functions (Section 4.1) and the  
722 functions common to all nuclides are contained in the `production` folder. Ad-  
723 ditional folders are available for surface sample dating (`surfacecalc`), depth  
724 profile dating (`profilecalc`), and calibration of production rates (`calib`,  
725 `muoncalib`, `pfzero`).

### 726 4.1. Core Functionality

727 The code is designed to predict concentration at a particular depth for  
728 the specified nuclide. This is done using a function called `predNXX`, where  
729 `XX` represents the desired nuclide (i.e. `predN36` calculates production of  
730  $^{36}\text{Cl}$ ). There are a few preliminary code modules necessary to build the in-  
731 puts required for the main code. These include creating constants for physi-  
732 cal parameters (`physpars`), calculating scaling factors (`scalefacNXX`), orga-  
733 nizing the input sample parameters (`sampparsNXX`), and computing sample-  
734 dependent parameters that are needed for later calculations (`compparsNXX`).  
735 These are not discussed in detail here, but can be found in the Function  
736 Appendix in the Supplementary Materials and will be available online for  
737 download with the code. `PredNXX` uses all this preliminary information in  
738 order to predict concentrations of the nuclide. This is summarized in Figure  
739 3 for the  $^{10}\text{Be}$  code.

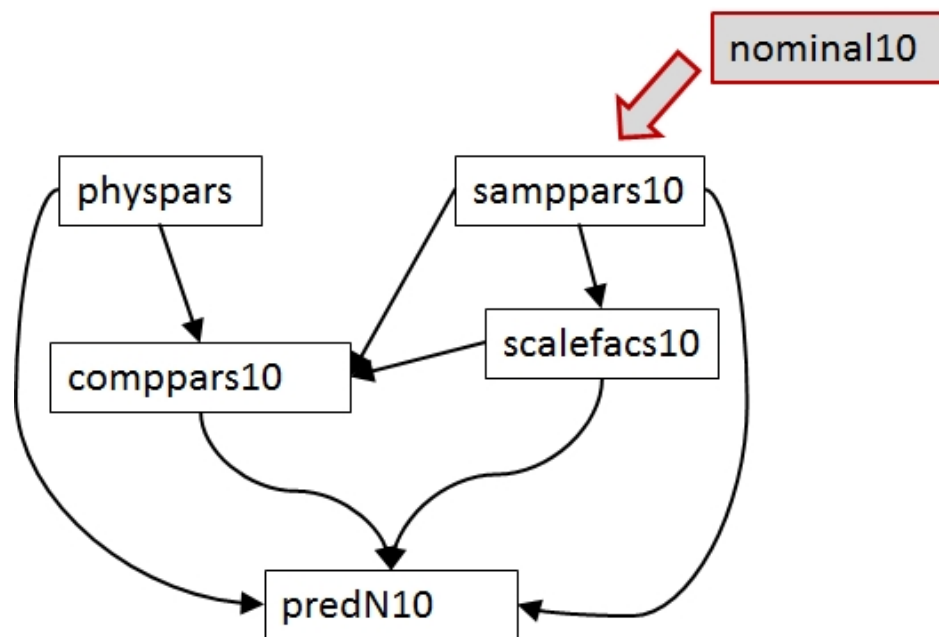


Figure 3: Data flow diagram showing the relationship between different parts of the code for a  $^{10}\text{Be}$  sample. Inputs include the nominal inputs (`nominal10`) and the uncertainties on each of those inputs (`uncerts10`, not shown). Other code pieces (`physpars`, `samppars10`, `comppars10`, and `scalefacs10`) set up the correct variables for the upper-level code pieces. `predN10` predicts the concentration for a given age and depth.

740 *4.2. Features*

741 This program has several differences as compared to previous calculators.  
742 The CRONUScalc program is designed to work for all the commonly used  
743 nuclides, including  $^{10}\text{Be}$ ,  $^{26}\text{Al}$ ,  $^3\text{He}$ ,  $^{36}\text{Cl}$ , and  $^{14}\text{C}$ , with  $^{21}\text{Ne}$  in testing. The  
744 modular nature of the program means that the scaling frameworks are ap-  
745 plied in an identical manner to each nuclide, avoiding possible inconsistencies  
746 from errors in coding or using two different calculators for cross-nuclide com-  
747 parisons. The addition of a new scaling framework by Lifton et al. (2014)  
748 allows for a physics-based calculation of the incoming cosmic-ray flux as well  
749 as nuclide-dependent scaling frameworks that incorporate the individual nu-  
750 clide reaction cross-sections. This calculator has an easy input structure so  
751 that samples can be copied from spreadsheets and allows the user to run  
752 multiple samples simultaneously. This is one of the only calculators to allow  
753 the user to specify uncertainties on all input parameters and propagate those  
754 to the resulting exposure age. Finally, this program does not require any pro-  
755 prietary software because it can be run on either MATLAB or Octave, the  
756 latter being open-source.

757 CRONUScalc is able to calculate production and accumulation for any  
758 given sample as well as perform calibrations and calculate surface sample  
759 and depth-profile exposure ages. This calculator provides both surface sam-  
760 ple and depth-profile dating abilities based on the same underlying code.  
761 Included in the surface calculator is the ability to date a single sample at  
762 depth. The code does not currently calculate burial ages.

763 Other new features that are not clearly visible in the upper levels of the  
764 program are the new integration method and the newly calibrated Heisinger  
765 muon production formulation. Some previous calculators relied on analytical  
766 solutions to integrate over depth by incorporating a 'thickness correction  
767 factor'. In this program, a numerical depth integration is performed, which  
768 removes approximations necessary in the analytical solution. This results in  
769 a more accurate inventory of accumulated nuclide in the sample as well as  
770 the ability to easily modify the code to look at multiple time periods with  
771 varying erosion rates. The new muon production is scaled using Lifton et al.  
772 (2014), and includes new production rate parameters calibrated from deep  
773 profiles for  $^{10}\text{Be}$ ,  $^{26}\text{Al}$ , and  $^{36}\text{Cl}$  (for both Ca and K).

774 Finally, although this paper discusses primarily the code behind the pro-  
775 gram, there is an online interface for the surface calculator, and other small  
776 tools such as the topographic shielding calculator, available to the public  
777 with no need to directly manipulate the code (<http://web1.ittc.ku.edu>:

778 8888/). This simplifies the process and makes the technique available to a  
779 much broader range of users. Instructions for use of the interface calculators  
780 will be maintained online.

## 781 **5. Surface Sample Calculator**

782 The Balco et al. (2008) calculator put the Al/Be cosmogenic nuclide com-  
783 munity on a consistent platform by providing a reliable tool for consistent  
784  $^{10}\text{Be}$  and  $^{26}\text{Al}$  exposure age calculations. However, this did not apply to any  
785 other nuclides and the code did not allow the user to fully propagate uncer-  
786 tainties on all input parameters. CRONUScalc extends this idea to include  
787 multi-nuclide capability, full propagation of uncertainties, and the ability to  
788 work with single samples at depth.

789 Using the equations given in the previous sections, we can compute the  
790 rate of production of a cosmogenic nuclide at any depth within the subsur-  
791 face at any point in the past. This production rate varies over time due to  
792 time-dependent scaling as well as varying due to changes in depth caused  
793 by erosion or aggradation. While the nuclide is accumulating it is also con-  
794 tinuing to decay - the radioactive decay rate must be subtracted from the  
795 production rate. The time-dependent production rate can be numerically  
796 integrated over time in order to predict the concentration of the cosmogenic  
797 nuclide at a specific depth after a specified exposure history. By averaging  
798 the accumulated production at depths throughout the thickness of a sam-  
799 ple, we can predict the average concentration of the cosmogenic nuclide as a  
800 function of the exposure age of the sample.

### 801 *5.1. Computing the Exposure Age or Erosion Rate*

802 To compute the exposure age of a sample, we begin by checking for sat-  
803 uration. This is done by computing the sample-specific saturation concen-  
804 tration by predicting the accumulated concentration in the sample assuming  
805 an exposure time of at least six half-lives, incorporating time-dependent pro-  
806 duction rates and ending in the sample collection year, and using all other  
807 user-provided inputs (see Section 3 for a list of inputs). If the measured  
808 concentration of the cosmogenic nuclide is close to or exceeds the satura-  
809 tion concentration (95% or more), then it is not possible to determine an  
810 exposure age for the sample because the sample is effectively saturated. If  
811 not, then we use the bisection method to find an age at which the predicted  
812 concentration matches the measured concentration of the nuclide. A similar

813 method is applied in order to determine erosion rate for a sample when ei-  
814 ther an independent age is supplied or equilibrium with erosion rate can be  
815 assumed.

## 816 *5.2. Input Uncertainties and Derivatives*

817 The computed exposure age for a sample depends on a number of sample  
818 parameters in addition to the measured nuclide concentration, including its  
819 thickness and density, the assumed erosion rate, the assumed atmospheric  
820 pressure at the exposure site, etc. For each of these parameters, we compute  
821 the derivative of the exposure age with respect to the parameter by finite  
822 difference approximation. If the user supplies uncertainties for these param-  
823 eters, then these derivatives are employed to propagate the uncertainties in  
824 the parameters into an uncertainty on the computed exposure age, using first  
825 order Taylor series expansion (Bevington & Robinson, 1992).

826 The code allows for detailed quantification of the uncertainties associ-  
827 ated with a sample. The commonly reported uncertainty, that from only the  
828 AMS analysis, represents the minimum uncertainty in the age of an unknown  
829 sample. There are uncertainties in the other measurements (chemical concen-  
830 trations, field measurements, etc.), production rates, scaling, and laboratory  
831 processing. CRONUScalc allows an uncertainty to be assigned to each of the  
832 input parameters, a feature that is unavailable in other single-sample sur-  
833 face exposure age calculators. This idea was addressed in the multi-sample  
834 depth-profile calculator using Monte Carlo methods presented by Hidy et al.  
835 (2010), but is treated more systematically here using derivatives. In a manner  
836 similar to that employed by Balco et al. (2008), CRONUScalc distinguishes  
837 between analytical (internal) uncertainty, which is calculated by propagating  
838 uncertainties on every input parameter in `uncertsXX`, and total uncertainty,  
839 which is calculated by fully propagating the production-rate uncertainty and  
840 combining it with the analytical uncertainty. Although statistically-based  
841 uncertainties on the production rate parameters were not possible (Borchers  
842 et al., 2015), an alternative method to assess the uncertainty on this parame-  
843 ter was used in an attempt to provide a more complete uncertainty estimate.

844 The uncertainty associated with the nuclide production rate (i.e., the  
845 uncertainty added to the analytical uncertainty to give the total uncertainty)  
846 is based on a comparison of the deviations of the calculated ages for the  
847 secondary data set with the independent (and assumed correct) ages for those  
848 samples. In essence, the uncertainty associated with the production rate was  
849 increased until the average standard deviation of the calculated ages matched

850 the spread of the deviations of the calculated ages from the independent  
851 ages. This empirical estimation of the additional uncertainty assumes that  
852 the residuals between the calculated ages and the independent ages averages  
853 zero and has a normal distribution. The actual distribution of residuals only  
854 marginally supports this assumption. The most significant sources of the  
855 additional uncertainty (not accounted for by the assigned analytical or other  
856 measurement uncertainties) are the following four. (1) Underestimation of  
857 the actual analytical uncertainties. Jull et al. (2013) have presented evidence  
858 that laboratory-reported uncertainties generally underestimate, sometimes  
859 by significant amounts, the actual spread of the cosmogenic-nuclide analytical  
860 data. (2) Errors in spatial scaling. Regularities in the residuals as a function  
861 of location and elevation give clues that even the best scaling models may  
862 not completely predict the global pattern of nuclide production (Phillips  
863 et al., 2015). (3) Errors in the assigned independent ages for the primary  
864 calibration data sites. Although sites with very well constrained ages were  
865 used, they cannot be guaranteed to all be completely accurate. (4) Site-  
866 specific factors. Assumptions regarding factors such as snow cover, lack of  
867 covering deposits in the past, and erosion rates may have been in error for  
868 some sites. In summary, the additional uncertainty that is specified for the  
869 production-rate terms incorporates all sources of uncertainty or bias that are  
870 not included in the reported laboratory analytical uncertainties. It reflects  
871 the likelihood that a single, randomly selected, high-quality, cosmogenic-  
872 nuclide age will correspond to an independently determined exposure age for  
873 the same material, empirically assessed using the CRONUS-Earth secondary  
874 data sets. Full details on the method, assumptions, and the uncertainty  
875 sources incorporated into the production-rate uncertainty are discussed in  
876 Phillips et al. (2015).

877 It is important to differentiate between the two reported uncertainty types  
878 (analytical and total). For example, analytical uncertainties alone are likely  
879 to underestimate realistic uncertainties when comparing to other dating tech-  
880 niques or comparing widely geographically or temporally separated cosmo-  
881 genic samples. On the other hand, the total uncertainty may overestimate  
882 uncertainties when comparing between groups of samples from a single ge-  
883 ographic location where uncertainties are not independent (e.g. in certain  
884 cases, production rate uncertainties are unimportant for relative chronology  
885 at a single site) (Dunai, 2010; Balco et al., 2008). Comparisons between nu-  
886 clides can be complicated by the use of different calibration data sets and  
887 production models, so it may be necessary to use the external uncertainties



888 to compare between samples from different nuclides located at the same site  
889 (Balco et al., 2008). Both uncertainties are reported, allowing the user to  
890 determine which is the most appropriate for each particular study. The user  
891 is encouraged to report all inputs, including assigned uncertainties, and note  
892 the type of uncertainty used in analyses.

893 A sensitivity analysis was performed in order to determine which inputs  
894 and their uncertainties have a significant effect on the sample exposure age.  
895 The results of the sensitivity analysis are presented in Figure 4. It is based  
896 on a random selection of the  $^{36}\text{Cl}$  primary and secondary calibration samples  
897 (see Marrero (2012) for details), although similar results were seen for  $^{10}\text{Be}$   
898 samples. The results presented are merely intended to be representative and  
899 will vary from sample to sample. Sensitivities are only given for standard  
900 environmental parameters that are applicable for all nuclides. Chlorine-36  
901 uncertainties are also sensitive to sample chemical composition. This topic  
902 is dealt with separately for  $^{36}\text{Cl}$  in Marrero et al. (2015).

903 Based on this sensitivity analysis, there are some uncertainties that are in-  
904 significant. For example, realistic uncertainties on longitude and latitude are  
905 not important when compared to uncertainties on the concentration. Other  
906 variables that realistically do not require uncertainties include shielding and  
907 year collected. On the other hand, relatively large and potentially biased  
908 uncertainties are expected on parameters such as erosion rate and water con-  
909 tent because these require estimation and some knowledge of the site and  
910 can rarely be precisely calculated.

911 When comparing different nuclide results, especially those from different  
912 sites, all uncertainties must be assessed in a consistent manner. The un-  
913 certainties from scaling and methodological considerations become primary  
914 issues. The interlaboratory studies associated with the CRONUS project  
915 (Jull et al., 2011, 2013; Vermeesch et al., 2012; Schaefer et al., 2014; Blard  
916 et al., 2014) were designed to address the uncertainties that arise solely from  
917 different processing techniques and accelerator measurements. These results  
918 were used to incorporate realistic uncertainty into the nuclide concentrations  
919 used for calibration (see Phillips et al. 2015 for details).

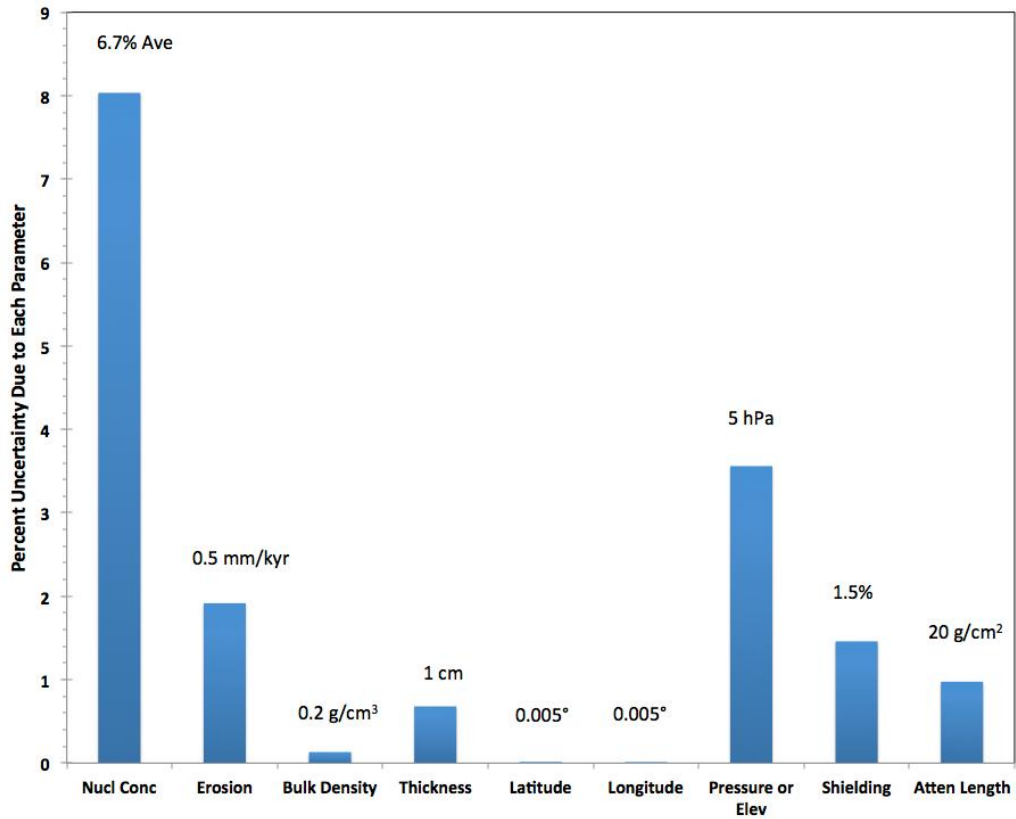


Figure 4: Amount of uncertainty (as a percentage of the final calculated age) contributed by conservative uncertainties assigned to individual sample parameters. The analysis presents the average of the propagated uncertainties for 15 primary and secondary <sup>36</sup>Cl calibration samples (Marrero, 2012; Marrero et al., 2015). The values above each bar give the assigned uncertainty in the parameter.

## 920 6. Depth-Profile Calculator

921 The depth profile calculation is formulated as a Bayesian inverse prob-  
922 lem. This approach has several advantages. First, unlike using a classical  
923 statistics approach to parameter estimation, the Bayesian approach treats un-  
924 known parameters as random variables. Doing so allows the resulting fitted  
925 parameters to be reported as expected values, accompanied by a probability  
926 distribution. Second, this approach allows the user to submit prior infor-  
927 mation or expert knowledge, influencing the solution. The selection of an  
928 informative prior distribution for parameters will strongly bias the resulting  
929 posterior distribution. Therefore the responsible user is obligated to report  
930 the effect that different priors have on their solution. Third, from a compu-  
931 tational standpoint, the method presented in this section is not susceptible  
932 to the convergence failures that iterative line-search solvers can encounter in  
933 certain cases.

934 The inputs to the depth profile code are the same as those for the surface  
935 calculator, with several additional parameters required only for the profile  
936 calculation. The new parameters include maximum and minimum values  
937 for erosion rate, exposure age, and inheritance. In addition to erosion rate  
938 bounds, a value for total maximum erosion (positive or negative) can be used  
939 to additionally constrain the final results, which can be useful as total erosion  
940 can sometimes be easier to determine in the field. Some parameters common  
941 to the surface calculator, such as depth to top of sample and attenuation  
942 length, become more significant in the depth profiles than they were for  
943 surface samples. These parameters are both user inputs (i.e. the calculator  
944 assumes these are known parameters), although the uncertainties in these  
945 parameters have the potential to increase the uncertainty in the calculated  
946 age of the profile. One initial sensitivity test on a profile indicated that  
947 reasonable uncertainties on attenuation length were relatively insignificant,  
948 although reasonable uncertainties on bulk density measurements could result  
949 in up to 5% change in nominal age. For details on other parameters, see the  
950 sensitivity study results in Section 5.2. The depth profile calculator does not  
951 explicitly incorporate uncertainties on input parameters other than nuclide  
952 concentration.

953 Performing the depth profile calculation requires the simultaneous esti-  
954 mation of three parameters: age ( $t$ ), erosion rate ( $\epsilon$ ), and inheritance (inh).  
955 The steps necessary for the computations are summarized here. First, an  
956 evenly spaced, 3-dimensional grid over the parameters of age, erosion rate,

957 and inheritance is created. Note that the spacing is consistent only within  
 958 each dimension and the parameter range for each is specified by the user.  
 959 Second, the misfit  $\chi^2$  value is calculated at each node (each age, erosion rate,  
 960 and inheritance point) using Equation 10.

$$\chi_{t,\epsilon,inh}^2 = \sum_i^n \left( \frac{x_i}{\sigma_i} \right)^2 \quad (10)$$

where

$$x_i = ConcPred_{t,\epsilon,inh} - ConcMeas_i$$

961 Next, the approximated  $\chi^2$  hyper-surface is transformed into a likelihood  
 962 surface using Equation 11.

$$L(\mathbf{x}|\boldsymbol{\theta}) = \prod_{i=1}^n \left( \frac{1}{\sqrt{2\pi}\sigma_i} \right) \cdot \exp \left( -\frac{\chi_{t,\epsilon,inh}^2}{2} \right). \quad (11)$$

963 Finally, to calculate the joint posterior from the likelihood we use Bayes  
 964 rule, shown in Equation 12.

$$p(\boldsymbol{\theta}|\mathbf{x}) = \frac{L(\mathbf{x}|\boldsymbol{\theta})\pi(\boldsymbol{\theta})}{\int_{-\infty}^{\infty} L(\mathbf{x}|\boldsymbol{\theta})\pi(\boldsymbol{\theta})d\boldsymbol{\theta}}, \quad (12)$$

965 where  $\pi(\boldsymbol{\theta})$  is the joint prior distribution set by the user on the following  
 966 parameters: age, erosion rate, and inheritance. A trapezoidal integration  
 967 scheme is used to calculate the denominator, leaving the joint posterior den-  
 968 sity,  $p(\boldsymbol{\theta}|\mathbf{x})$ .

969 When assigning uncertainties to a solution, it is important to determine  
 970 if any multiple interactions exist between erosion rate, age, and inheritance.  
 971 To display these interactions, the calculator produces 3 pairwise 2-D contour  
 972 plots of the joint posterior distribution with contours of 68% and 95% regions  
 973 of probability. For example, integrating  $p(\boldsymbol{\theta}|\mathbf{x})$  over inheritance gives the  
 974 probability distribution given by  $p(\epsilon, t|\mathbf{x})$ . This effectively marginalizes the  
 975 joint posterior over one of the three parameters. An example of the resulting  
 976 2-D contour plots are shown in Figure 5, along with the predicted versus  
 977 measured profile plot.

978 The best-fitting solution is the lowest chi-squared value over the entire  
 979 three-dimensional grid. This is called the maximum a posterior (MAP) solu-  
 980 tion. In the 2-D pairwise plots, the MAP solution and the apparent 2-D best-  
 981 fit solution do not always coincide due to the interaction of the parameters

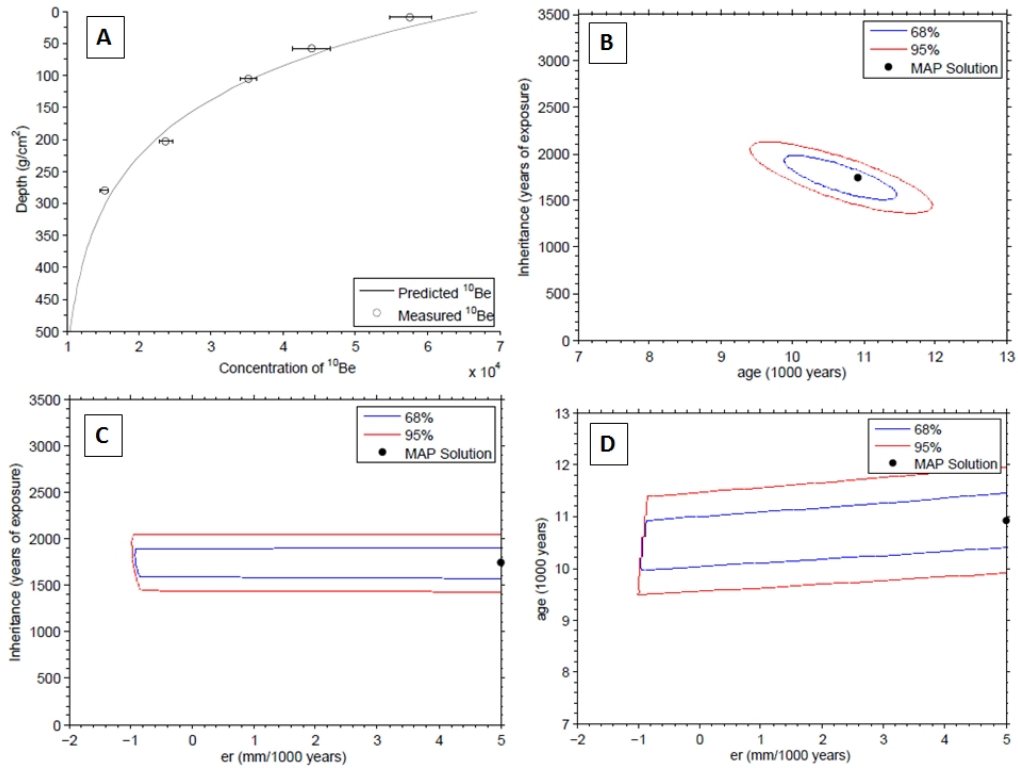


Figure 5: Example of the profile and pairwise plots produced by the depth profile calculator. The example is a  $^{10}\text{Be}$  profile published by Goehring et al. (2010a) and used as an example in Aumer (2010). MAP solution is the best-fitting 3-D solution. 68% and 95% contours are the confidence intervals for the chi-squared values. (A) Figure shows the measured data and the predicted profile with depth; (B) Figure shows the confidence intervals for the plot of the inheritance and age; (C) Figure shows the confidence intervals for the plot of the inheritance and erosion rate; (D) Figure shows the confidence intervals for the plot of the age and erosion rate.

982 with the third dimension. The direct calculation of posterior probabilities  
983 eliminates the need for Monte Carlo, as was used by Hidy et al. (2010). In  
984 contrast to Hidy et al. (2010), this code also computes a posterior probabil-  
985 ity distribution, allowing for an assessment of the probability of the resulting  
986 age being within particular age bounds. While there are other mathematical  
987 methods or spreadsheets available for calculating depth profiles (Braucher  
988 et al., 2009; Hein et al., 2009; Schaller et al., 2009), we discuss CRONUScale  
989 in relation to Hidy et al. (2010) because of its similar format and explicit  
990 distribution for use as a depth profile calculator.

## 991 **7. Discussion and Cautions**

### 992 *7.1. Atmosphere and Elevation Relationships*

993 The relevant inputs are both elevation and atmospheric pressure for the  
994 sample. Elevation, which is more easily measured and can be found on a to-  
995 pographic map even after sampling, is the traditional input for these codes.  
996 The additional pressure input is necessary because it is the more accurate  
997 measure of the sample location in the atmosphere. If the user does not specify  
998 a site pressure, the online user interface automatically estimates the pressure  
999 using the ERA40 Reanalysis data set. The ERA40 reanalysis is a synthesis of  
1000 comprehensive global observations and analyses over a 45 year period, as dis-  
1001 cussed in Uppala et al. (2005). This pressure calculation module is available  
1002 with the code and pressure is a required input (not automatically calculated)  
1003 within the raw code. The production-rate calibrations were all done using  
1004 pressures determined from ERA40 and it is recommended that this conver-  
1005 sion be used unless there is a specific reason to suspect a significantly different  
1006 pressure relationship over the sample exposure period. ERA40 functions in  
1007 Antarctica so no separate atmosphere relationship is required.

1008 Uncertainty in the sample pressure is a significant contributor to sample  
1009 uncertainty. The uncertainty associated with the pressure based on uncer-  
1010 tainties in elevation is quite small ( $<1$  hPa for elevation uncertainties up to  
1011 15 m). This results in only a small amount of total uncertainty on the sample  
1012 age ( $<1\%$ ). A more realistic source of uncertainty associated with pressure  
1013 is the difference between the current pressure and the average pressure over  
1014 the exposure time of the sample. The pressure history through time is not a  
1015 factor that can be accurately calculated. Our assumption that the pressure  
1016 has remained relatively constant through time adds additional uncertainty.  
1017 Based on the maximum differences observed between corresponding grid cells

1018 in the NCEP/NCAR and ERA40 (Uppala et al., 2005) reanalyses, we have  
1019 added a conservative uncertainty of 5 hPa to the CRONUS-Earth samples  
1020 to account for this and this addition results in uncertainties of 2-5% for most  
1021 samples.

## 1022 *7.2. Uncertainties Due to Scaling*

1023 Not all scaling frameworks fit the calibration data equally well. For each  
1024 nuclide, a single data set was used to produce a production rate for each com-  
1025 bination of scaling framework and nuclide. Because of its favorable analytical  
1026 precision and accuracy, relative simplicity of its production mechanisms, and  
1027 the large number of analyses, the nuclide best suited to evaluating the ad-  
1028 equacy of scaling frameworks is  $^{10}\text{Be}$ . This topic is discussed more fully in  
1029 Borchers et al. (2015) and Phillips et al. (2015), but is briefly summarized  
1030 here. The average absolute error, by site averages, of the predicted vs. mea-  
1031 sured concentrations for the neutron-monitor-based scaling methods (Lifton,  
1032 Dunai, Desilets) varied from 15.7 to 18.1 %. Those for the scaling methods  
1033 based on more direct measures of spallation reactions (Lal-based and LSD)  
1034 varied from 8.5 to 9.7 %. The second group is clearly more accurate. Al-  
1035 though within this group the LSD-flux based model gave the best fit, the  
1036 differences are so small that no clear preference is evident. In the following  
1037 discussion of scaling uncertainty, the neutron-monitor based scaling methods  
1038 were not considered due to the poor fit to the data set.

1039 A second issue associated with scaling is the uncertainty from determining  
1040 the scaling factor at a new location that is not a calibration site. The basis  
1041 for estimating this contribution to the total age uncertainty is weak. The  
1042 best basis available is found by comparing the fit of the primary CRONUS-  
1043 Earth  $^{10}\text{Be}$  data set (to which the production rates were calibrated) to the  
1044 fit of the secondary data set (which is independent of the primary data set)  
1045 in Borchers et al. (2015). For the best-fitting scaling framework (LSD-flux  
1046 based), the average absolute error was 5.4 % for the primary data set, com-  
1047 pared to 8.5 % for the secondary data set. The difference between these two  
1048 uncertainties could be interpreted to suggest that error in predicting scaling  
1049 at non-calibration sites contributes about 3 % to the total age uncertainty.  
1050 However, the following factors must be considered: (1) the source of the  
1051 variability cannot be assigned strictly to scaling and could, in fact, be due  
1052 to other issues, such as the production rate calibration (2) samples were as-  
1053 signed to the secondary data set because they were weaker than those in the  
1054 primary one due to factors such as less well constrained exposure histories,

1055 and therefore there are undoubtedly factors in addition to scaling uncer-  
1056 tainty contributing to their larger scatter, and (3) error in scaling clearly  
1057 contributes to the 5 % scatter obtained for the primary data set, giving a  
1058 contribution to the uncertainty from scaling that is not accounted for in the  
1059 comparison. Factors (1) and (2) contribute to a decrease in scaling uncer-  
1060 tainty while factor (3) contributes to an increase in uncertainty. The balance  
1061 between these cannot at present be known, but likely the error in scaling, on  
1062 average, contributes significantly less than 3 % to the total age uncertainty.

1063 The original CRONUS-Earth production-rate calibration was not able to  
1064 calculate statistical uncertainties on the production rate parameters (Borchers  
1065 et al., 2015). Instead, the CRONUS-Earth Project employed an empirical  
1066 method for estimating production-rate uncertainty based on the secondary  
1067 data set (Phillips et al., 2015). The empirical method does not break out the  
1068 contribution to that uncertainty from scaling alone, but it does incorporate  
1069 that source of uncertainty into the production-rate uncertainty recommen-  
1070 dation. This inferred production-rate uncertainty is propagated along with  
1071 other parameter uncertainties in CRONUScalc to provide the total uncer-  
1072 tainty on a sample. Additional insight into scaling uncertainty can be ob-  
1073 tained from the "leave-one-out cross-validation exercise" in Borchers et al.  
1074 (2015).

### 1075 *7.3. Limitations of CRONUScalc*

1076 Although CRONUScalc has new capabilities not previously available in  
1077 other calculators, there are some limitations to the program. CRONUScalc  
1078 was designed to provide the most accurate model for a wide range of samples,  
1079 meaning that approximations were avoided in most cases unless they could  
1080 be shown not to increase uncertainty or error. The incorporation of more  
1081 physics-based modeling into the program has substantially increased the cal-  
1082 culation time for each sample. The online interface minimizes this problem  
1083 by emailing the user with results, original inputs, and all data necessary  
1084 to recreate the graphs prior to their deletion from the server so no further  
1085 contact with the website is required. While samples are running, the user  
1086 is provided a link that shows current progress on submitted samples. The  
1087 use of email avoids browser timeout problems and decreases the dependence  
1088 on a reliable internet connection. Emails and all sample data, except usage  
1089 statistics on general location and nuclide, are automatically deleted every 24  
1090 hours from the server to protect anonymity.



1091 The current program only process one scaling model at a time for each  
1092 sample. While it can be instructive to examine outputs from multiple scaling  
1093 models, the addition of two new scaling models, for a total of seven, makes  
1094 this time-prohibitive given the new framework. By allowing multiple samples  
1095 to be submitted simultaneously, users can still perform the scaling compar-  
1096 isons by submitting samples more than once with a different scaling model  
1097 selection.

#### 1098 *7.4. Expected Changes in Performance Due to New Scientific Content*

1099 Comparisons to results from other similar cosmogenic calculators do not  
1100 serve to show that CRONUScalc functions as expected for two main rea-  
1101 sons. First, differences in the calibration data sets used by each program  
1102 lead to very different results. Second, CRONUScalc has a different set of as-  
1103 sumptions, parameters, and implementations than other programs, leading  
1104 to results that differ by more than rounding error from the other programs,  
1105 even when identical calibration data sets are used. Fundamentally, differences  
1106 between the various programs are expected and this makes it impossible to  
1107 prove the accuracy of CRONUScalc by obtaining the same results as those  
1108 produced by other programs. The main differences are discussed later in this  
1109 section.

1110 However, in the very simplest case where there is only spallogenic pro-  
1111 duction and we assume a time-independent production rate, it is possible to  
1112 compare results from our code with the analytical solution given by equation  
1113 4.11 in Dunai (2010). The  $^3\text{He}$  calculator was tested against analytically  
1114 predicted concentrations for sample ages varying between 0.001-7000 ka and  
1115 erosion rates of 0, 1, and 10 mm/kyr. At the highest erosion rates, the oldest  
1116 samples were saturated. For all unsaturated samples, the differences between  
1117 the analytically produced concentrations and the CRONUScalc solution were  
1118 less than 0.005%, with most several orders of magnitude smaller. The results  
1119 are presented in Appendix D. The agreement between CRONUScalc and  
1120 analytical solutions indicates that the CRONUScalc numerical integration  
1121 performs well over a variety of erosion rates and ages. CRONUScalc results  
1122 for other nuclides cannot be directly compared to analytical solutions due to  
1123 the complex muon model and other new features, but the underlying age in-  
1124 tegration will be as accurate as demonstrated for  $^3\text{He}$ , because of the shared  
1125 numerical integration code.

1126 The section below highlights the new scientific content in CRONUScalc  
1127 that is most likely to contribute to differences in performance when compared

1128 to other similar calculators. This section does not discuss the features of other  
1129 calculators, but reiterates the key scientific content present in CRONUScalc  
1130 and the situations that may yield major differences.

1131 The addition of a new pair of scaling models (flux-based and nuclide-  
1132 dependent models from Lifton et al. (2014)) provides a flexible, physics-  
1133 based model for scaling production rates, but it also introduces the possi-  
1134 bility for differences that vary by location and elevation when compared to  
1135 results from other scaling models available in CRONUScalc or other pro-  
1136 grams. Lifton et al. (2014) contains a more detailed discussion of differences  
1137 between resulting scaling factors, including the effects of solar modulation  
1138 and the updated geomagnetic history.

1139 CRONUScalc allows the user to specify an uncertainty for each parameter  
1140 in the input. In addition to those analytical uncertainties, the production-  
1141 rate uncertainty is propagated through to produce a total uncertainty for each  
1142 sample (see Sections 5.2 and 7.2). Although the added flexibility to include  
1143 an uncertainty on each input is useful, especially for older samples where  
1144 fewer parameters were accurately reported, the CRONUScalc uncertainties  
1145 will likely be different from those reported by other available calculators.

1146 CRONUScalc muon production follows the Heisinger model, but uses  
1147 CRONUS-Earth calibrated muon production rates (Fig 1 in Phillips et al.,  
1148 2015) and is scaled using Lifton et al. (2014). In the fast muon formulation,  
1149 CRONUScalc assumes a value for  $\alpha$  (the parameter that defines how the  
1150 cross-section scales with muon energy) equals one (see Section 2.1.3). This  
1151 has a small effect on the elevation dependence on production rates when  
1152 compared to models that use the value of  $\alpha$  equal to 0.75 reported in the  
1153 original paper (Heisinger et al., 2002b).

1154 As discussed in Section 3.4, CRONUScalc only includes the spallation  
1155 pathway for  $^3\text{He}$  production calculations. This may be appropriate for some  
1156 samples, but users are cautioned to check the composition of samples to  
1157 confirm that this is true. Even moderate to low concentrations of lithium  
1158 (Li) in a sample can potentially contribute significant production via thermal  
1159 neutron production, which is not accounted for in this model.

1160 CRONUScalc calculations for  $^{36}\text{Cl}$  are more complex than for other nu-  
1161 clides, introducing more possible contributors to differences when comparing  
1162 results from other programs. CRONUScalc includes  $^{36}\text{Cl}$  production from  
1163 both fast and slow muons. For samples with higher chlorine concentrations,  
1164 an updated set of elemental parameters (Table 1) may make significant dif-  
1165 ferences in calculated sample results, especially for samples high in boron.

1166 Finally, CRONUScalc assumes that the  $^{36}\text{Cl}$  concentration is in equilibrium  
1167 with the radiogenic and nucleogenic production rates in order to calculate the  
1168 radiogenic subtraction (only significant for samples high in Th or U). This  
1169 is unimportant for rocks with very old formation ages, but it is less clear  
1170 whether this is appropriate for rocks where the formation age is equal to the  
1171 exposure age. For example, based on available data for basalts, it is unclear  
1172 if radiogenic production should begin at eruption or if it is in equilibrium  
1173 prior to that time. Additional research is required to distinguish between  
1174 these two models.

## 1175 **8. Conclusion**

1176 The CRONUScalc program, designed to predict sample concentrations at  
1177 a particular depth, is intended to be versatile and work quickly for the largest  
1178 number of possible applications without sacrificing accuracy. The program's  
1179 abilities to calculate surface and depth-profile exposure ages, calculate ero-  
1180 sion rates, and perform calibrations offer many options to the user. However,  
1181 the code is available under a public license, so advanced users can modify the  
1182 code to work for unusual scenarios. The new features, including a new scal-  
1183 ing framework that performs nuclide-dependent scaling and a more accurate  
1184 integration method, provide an internally consistent option for cosmogenic  
1185 nuclide modeling. While the code can be adapted to many different functions,  
1186 an online calculator with a simple interface has been designed for surface and  
1187 depth-profile exposure age calculation (<http://web1.ittc.ku.edu:8888/>)  
1188 in order to remove any necessity of a Matlab license or knowledge of coding  
1189 and make the code easily available to the general cosmogenic isotope user  
1190 community.

1191 All the previous CRONUScalc versions will be archived in the online code  
1192 repository and available for calculation of previously published results.

## 1193 **9. Acknowledgments**

1194 This research was supported by the National Science Foundation through  
1195 the Cosmic-Ray-Produced Nuclides on Earth (CRONUS-Earth) Project through  
1196 grant EAR-0345949. We would like to thank all the members of the CRONUS-  
1197 Earth and CRONUS-EU Projects for their input. This manuscript benefited  
1198 from three thorough reviews by P. Vermeesch, R. Braucher, and an anony-  
1199 mous reviewer.

## 1200 Appendix A. Production Models

1201 The sections below describe the fundamental theory behind the code.  
1202 This appendix is provided to summarize the systematics of the program  
1203 without referring back to numerous previous publications. See the main text  
1204 for summaries of the key developments of CRONUScale.

### 1205 *Appendix A.1. Cosmic Rays*

1206 Cosmic rays originate primarily from Milky Way galaxy supernova, but  
1207 also from the sun and other energetic phenomena (Dunai, 2010; Gaisser,  
1208 1990; Gosse & Phillips, 2001; Pigati & Lifton, 2004). The main cosmogenic  
1209 particles reaching the atmosphere are protons (87% of the cosmic-ray flux),  
1210 with a smaller portion of the cosmic-ray flux composed of alpha particles  
1211 (12%) and other heavier nuclei (1%) (Dunai, 2010). These incoming particles  
1212 have a wide range of energies, with typical energies ranging from a few MeV  
1213 to  $10^{20}$  eV (Dunai, 2010). Over long periods (10 Ma), the integrated cosmic-  
1214 ray flux has been shown to be constant (to within 10%) when averaged over  
1215 500 kyr timescales, with the uncertainties becoming larger (up to 30% or  
1216 more) when averaged over timescales of hundreds of thousands to millions of  
1217 years (Wieler et al., 2013).

1218 As incoming cosmic-ray particles reach the top of the atmosphere, they  
1219 interact with the earth's magnetic field. Only particles with sufficiently high  
1220 energy and the correct trajectory will actually reach the earth's surface. This  
1221 control on the magnitude of the cosmic-ray flux is quantified by means of the  
1222 cutoff rigidity. The rigidity of a particle ( $R$ ) is given by Equation A.1. In  
1223 the equation for rigidity,  $p$  is the particle momentum,  $c$  is the speed of light,  
1224 and  $e$  is the particle charge.

$$R = pc/e \tag{A.1}$$

1225 The vertical cutoff rigidity, the minimum threshold for the particle energy  
1226 necessary in order to penetrate the field on a path normal to the magnetic  
1227 field, is the standard parameter used to organize the effect of the dipole  
1228 field on the cosmic-ray flux as a function of location on the surface of the  
1229 earth (Dunai, 2010; Gosse & Phillips, 2001; Lifton et al., 2005). The cutoff  
1230 rigidities are related to geomagnetic latitude, having very low values near the  
1231 poles ( $>58^\circ$  at sea level), resulting in admittance of essentially all cosmic-ray  
1232 particles, and increasing towards the equator (Lifton et al., 2005).

1233 The complexity of the paths of cosmic-ray particles due to interaction  
1234 of looping trajectories with the solid earth results in an area where there  
1235 are both allowed and forbidden trajectories in an alternating pattern known  
1236 as the penumbra (Hillas, 1972). In order to determine where this region is  
1237 and its effects on the cosmic-ray flux, reverse particle tracking (or trajectory  
1238 tracing) can be performed for particles within 20 km of the earth’s surface to  
1239 determine the effective vertical cutoff rigidity of a location (Shea & Smart,  
1240 1983; Dunai, 2010; Lifton et al., 2005). The effective vertical cutoff rigidity  
1241 is used in scaling frameworks to parameterize the cosmic-ray flux of a site.  
1242 Additional detail is given in the scaling section, Appendix C.

1243 After the primary cosmic-ray particles reach the top of the atmosphere,  
1244 they interact with atmospheric particles and create a cascade of secondary  
1245 particles. As these secondary particles are produced and the cascade prop-  
1246 agates through the atmosphere, several trends are apparent: the energy of  
1247 the secondary particles decreases, the total flux of particles decreases, and  
1248 the flux becomes dominated by neutrons due to the ionization losses of pro-  
1249 tons (Dunai, 2010). During these reactions, muons are also produced due to  
1250 secondary reactions by energetic incoming particles high in the atmosphere  
1251 (Eidelman, 2004). Unlike the hadronic component of the flux, the muonic  
1252 flux increases and then reaches a plateau as the cascade moves down through  
1253 the atmosphere because muons do not interact as strongly as neutrons and  
1254 are lost very slowly through ionization (Gaisser, 1990). At the earth’s sur-  
1255 face, muons comprise the majority of the particles in the incoming cosmic-ray  
1256 flux (Lal, 1988), but contribute less to surface production than do neutrons  
1257 due to their lower propensity for nuclear interactions.

1258 The energy spectrum of the neutrons that reach the earth’s surface de-  
1259 termines the rate of cosmogenic-nuclide-producing reactions. The neutrons,  
1260 which compose 98% of the nucleonic flux at the earth’s surface (Dunai, 2010),  
1261 have peaks in the energy spectrum at 100 MeV, 1-10 MeV, and <1 eV (Dunai,  
1262 2010; Goldhagen et al., 2002). The neutron energies discussed in this paper  
1263 will be categorized as high (>10 MeV), fast (0.1 to 10MeV), epithermal  
1264 (0.5eV to 0.1MeV), and thermal (<0.5 eV). While these conventions follow  
1265 other papers in the field (Gosse & Phillips, 2001; Schimmelpfennig et al.,  
1266 2008), there are no consistent classifications and the actual energies associ-  
1267 ated with the categories may vary in other publications (Dunai, 2010).

## 1268 Appendix B. Production Equations

1269 The production equations for CRONUScalc are provided here. The de-  
1270 tails below are discussed in general terms for production of any nuclide,  
1271 designated 'k', while details specific to a particular nuclide are discussed in  
1272 later sections.

### 1273 Appendix B.1. Spallation

1274 Spallation refers to the emission of a large number of nucleons (relative  
1275 to the original mass of the nucleus) when an atomic nucleus interacts closely  
1276 with a high-energy particle. In some cases (e.g.  $^3\text{He}$ ) a cosmogenic nuclide of  
1277 interest may be one of the ejected particles. More commonly, (e.g.  $^{26}\text{Al}$ ), it  
1278 is the remainder of the target nucleus. Cosmogenic-nuclide production from  
1279 spallation follows a well-established exponential decrease with depth. At the  
1280 surface, spallation is typically the dominant production mechanism. All the  
1281 nuclides discussed in this paper are produced through at least one spallation  
1282 pathway. The formula for the instantaneous production rate from spallation  
1283 ( $P_{s,m}$ ) is (Gosse & Phillips, 2001; Schimmelpfennig et al., 2008):

$$P_{s,m}(Z) = S_T \sum S_{el,s} P_{m,k}(0) C_k \exp\left(-\frac{Z}{\Lambda_{f,e}}\right), \quad (\text{B.1})$$

1284 where  $P_{m,k}$  is the sea-level, high-latitude production rate of species m  
1285 by spallation of element k (atoms  $\text{g}^{-1} \text{a}^{-1}$ ;  $S_T$  is the topographic shielding  
1286 factor (unitless);  $S_{el,s}$  is the geographical scaling factor for spallation reactions  
1287 for the particular reaction of interest, including temporal variation in the  
1288 production rate due to fluctuations in the geomagnetic field or solar magnetic  
1289 field (unitless);  $C_k$  is the concentration of the element k (atoms  $\text{g}^{-1} \text{a}^{-1}$ );  
1290 and  $\Lambda_{f,e}$  is the effective attenuation length for fast neutrons ( $\text{g cm}^{-2}$ ). The  
1291 production is summed for all target elements k that produce nuclide m to  
1292 give the total spallation production rate.

#### 1293 Appendix B.1.1. Attenuation Length

1294 The particle attenuation length is the passage length through a medium  
1295 required to attenuate the original intensity of a collimated beam of particles  
1296 by a factor of  $e^{-1}$  (Gosse & Phillips, 2001). This value varies depending on  
1297 the type of particle (proton, neutron, muon) and the associated energy level  
1298 (fast, thermal, epithermal, etc.). For neutrons, the main factor is the energy  
1299 level, with higher energy particles penetrating further into the subsurface

1300 than lower energy particles. The apparent attenuation length,  $\lambda_{f,e}$ , is the  
1301 flux-weighted integral of the particle attenuation length over the entire sky.

1302 The apparent attenuation length is an important parameter because it  
1303 quantifies the depth distribution of the production by neutron spallation.  
1304 The apparent attenuation length is defined with respect to a flat sample with  
1305 no topographic shielding. When the apparent attenuation length is adjusted  
1306 to account for the dip of the sample surface and any topographic shielding,  
1307 the result is the effective attenuation length,  $\Lambda_{f,e}$ . The effective attenuation  
1308 length is the parameter that should be used in calculations pertaining to  
1309 production from a particular sample.

1310 Typically, as the topographic shielding increases, the effective attenua-  
1311 tion length increases (Dunne et al., 1999). The spectrum of neutron energy  
1312 varies depending on the azimuth angle. The highest energy cosmic rays are  
1313 vertically incident upon the sample and the flux is dominated by these rays  
1314 (Dorman et al., 1999, in Dunai 2010). As the incident angle decreases going  
1315 from vertical to horizontal, the intensity of the cosmic rays decreases due to  
1316 the longer transport paths through the atmosphere (Dunai, 2010). The equa-  
1317 tion for this change in intensity is shown in Equation B.2. As topography  
1318 typically blocks out only cosmic rays near the horizon, the average energy  
1319 of the remaining cosmic rays increases. The sample dip also contributes to  
1320 a change in the effective attenuation length and shielding, as described in  
1321 Dunne et al. (1999).

$$I(\theta) = I_0 \sin^m \theta, \quad (\text{B.2})$$

1322 where  $I$  is the particle beam intensity and  $\theta$  is the inclination angle from  
1323 the vertical. The exponent  $m$ , which is dependent on both energy and particle  
1324 type, has been experimentally fit in several papers with significant differences  
1325 in the results, as discussed in Dunai (2010). The most commonly cited value  
1326 is  $2.3 \pm 0.5$  from Nishiizumi et al. (1989), although Lal (1958) also gives a  
1327 value of 2.3. However, Conversi and Rothwell (1954), cited by Lal, give a  
1328 value of  $2.1 \pm 0.3$  for 60 MeV nucleons ( $2.6 \pm 0.2$  for 750 MeV). In other  
1329 studies, values of  $2.5 \pm 0.5$  to  $3.0 \pm 0.5$  (Barford and Davis, 1952),  $3.5 \pm$   
1330  $1.2$  (Heidbreder et al., 1971), and 2.65 (Masarik et al., 2000) have also been  
1331 provided. Using Sato's PARMA model, the exponent is ca. 2.8 for neutrons  
1332 (calculated for neutrons  $>100$  MeV, at solar minimum, 200 m altitude,  $R_c$   
1333  $= 0$  GV). The corresponding result for protons of similar energies is on the  
1334 order of 3-3.5. Comparisons between this value and those reported in other

1335 studies must be considered with carefully because the energy ranges of the  
1336 measurements are potentially quite different. Muons follow a similar trend,  
1337 although the exponent in this case is 2 (Eidelman, 2004) or about 3.5 using  
1338 the PARMA model. CRONUScalc does not use this formulation, however,  
1339 and calculates the apparent attenuation length by interpolating from the  
1340 values in Table 4, which were obtained using the spreadsheet published with  
1341 Sato et al. (2008) and the adjustments described in the text.

1342 The effective attenuation length depends on the sample location as well as  
1343 the dip and shielding. The values for real samples vary from approximately  
1344 150-190 g/cm<sup>2</sup>, which overlaps with the measured values for the apparent  
1345 attenuation length,  $\Lambda_f$ , for fast nucleonic particles, which range from 121  
1346 to >170 g/cm<sup>2</sup> (Dunai, 2000). Some recent studies for Be use a value of  
1347 177 (Farber et al., 2008; Schimmelpfennig et al., 2008). In addition to the  
1348 dependence of the effective attenuation length on topographic shielding, it  
1349 also depends on site cutoff rigidity and elevation, due to the dependence  
1350 of the particle penetration length on particle energy. Samples from lower  
1351 elevation and lower latitude will have longer attenuation lengths because of  
1352 the increasing hardness of the neutron energy spectrum.

1353 The attenuation-length model in CRONUScalc is based on atmospheric  
1354 attenuation lengths calculated from the PARMA model of Sato et al. (2008).  
1355 These are adjusted upward by 11.1% to account for systematic differences  
1356 between atmospheric and lithospheric attenuation. See Section 2.4 for the  
1357 complete derivation of the CRONUScalc attenuation length model. The data  
1358 for the comparison of synthetic sample ages using different attenuation length  
1359 models are presented here (B.6).

#### 1360 *Appendix B.2. Epithermal Neutrons*

1361 Low-energy cosmogenic nuclide production, including that from thermal  
1362 and epithermal neutrons, does not follow a simple exponential pattern with  
1363 depth due to the atmosphere-ground interface effects. Due to the large cross-  
1364 section of nitrogen for absorption of low-energy neutrons, the flux of cosmo-  
1365 genic thermal and epithermal neutrons in equilibrium with air is much less  
1366 than that in equilibrium with rock. Low-energy neutrons produced in the  
1367 upper  $\sim 50$  cm of rock therefore tend to diffuse upward out of the rock and  
1368 into the atmosphere, resulting in a reduction of the flux as the rock surface  
1369 is approached (see Figure B.6). Phillips et al. (2001) analytically solved the  
1370 neutron-flux differential equation across the land/atmosphere interface to



Erosion (mm/kyr)	Be conc (at/g)	153 g/cm <sup>2</sup> Age (ka)	170 g/cm <sup>2</sup> Age (ka)
0	73513	20.0	20.0
0	360327	100.0	100.0
0	1029138	300.0	300.0
1	72154	20.0	20.0
1	328482	100.0	99.1
1	789962	300.0	290.8
2.5	70156	20.0	19.9
2.5	287378	100.0	97.6
2.5	558968	300.0	272.2
5	66974	20.0	19.8
5	233598	100.0	94.7
5	354648	300.0	230.2
10	61176	20.0	19.6
10	163166	100.0	86.9
10	195499	300.0	156.6

Table B.6: Summary of comparison of exposure ages using two different attenuation lengths for a variety of erosion rates. Sample parameters assumed in the calculations for CRONUScalc were: 40 deg latitude, 0 deg longitude, 0 m elevation, thickness of 0.001 cm, shielding of 1, density of 2.65 g/cm<sup>3</sup>, collection date of 2014 AD.

1371 obtain the equations below. These, in turn, were combined with the formu-  
 1372 lations for muon-induced neutron production by Gosse and Phillips (2001)  
 1373 to obtain the complete equations for epithermal production.

1374 The general form for the equation for the production of the cosmogenic  
 1375 nuclide of interest from epithermal neutrons is shown in Equation B.3. The  
 1376 epithermal neutron attenuation length ( $\Lambda_{eth,ss}$ , Equation B.4) accounts for  
 1377 both moderation and absorption of epithermal neutrons and parameterizes  
 1378 the effective depth of penetration of the epithermal neutron flux (Gosse &  
 1379 Phillips, 2001).

$$P_{eth,ss,m} = \frac{f_{eth,ss,m}}{\Lambda_{eth,ss}} \Phi_{eth,ss,total}(Z)(1 - p(E_{th})_{ss}), \quad (B.3)$$

1380 where  $f_{eth,ss,m}$  is the fraction of epithermal neutrons absorbed that are taken  
 1381 up by target element k to produce nuclide m (eqn E.15);  $\Phi_{eth,ss,total}$  is the  
 1382 epithermal neutron flux (eqn B.8).

$$\Lambda_{eth,ss} = [\bar{\xi}_{bulk}(I_{eff,ss} + \Sigma_{sc,ss})]^{-1} = \Sigma_{eth,ss}^{-1}, \quad (B.4)$$

1383 where  $\bar{\xi}_{bulk}$  is the average macroscopic log decrement energy loss per neutron  
 1384 collision in the subsurface (eqn E.28);  $I_{eff,ss}$  is the macroscopic resonance  
 1385 integral for absorption of epithermal neutrons in the subsurface (eqn E.16);  
 1386  $\Sigma_{sc,ss}$  is the macroscopic neutron scattering cross-section in the subsurface  
 1387 (Equation E.27).

1388 The distribution of epithermal neutrons in the subsurface can be de-  
 1389 scribed by Equation B.5. The epithermal neutrons are assumed to be pro-  
 1390 duced entirely from the moderation of both spallation and evaporation neu-  
 1391 trons and are assumed to be in equilibrium with the high-energy flux (Gosse  
 1392 & Phillips, 2001).

$$D_{eth,ss} \frac{d^2 \Phi_{eth,ss}}{dZ^2} = \frac{\Phi_{eth,ss}}{\Lambda_{eth,ss}} - R_{eth,ss} P_f, \quad (B.5)$$

1393 where the diffusion coefficient for epithermal neutrons in the subsurface  
 1394 ( $D_{eth,ss}$ ) is defined in Equation E.9, with the corresponding parameter in  
 1395 the atmosphere, defined in Equation E.10;  $R_{eth,ss}$  is the normalization factor  
 1396 for the epithermal neutron production rate (eqn E.25);  $P_f$  is the production  
 1397 rate of epithermal neutrons from fast neutrons, with the value at the surface  
 1398 represented as  $P_f(0)$ , which is a calibrated production rate parameter for  
 1399  $^{36}\text{Cl}$ .

1400 The observed subsurface, epithermal neutron flux,  $\Phi_{eth,ss}$ , at a particular  
 1401 point is the balance of exponential production with depth against the loss of  
 1402 neutrons through diffusion at the rock/air interface as well as loss through  
 1403 absorption and moderation. The hypothetical epithermal neutron flux in the  
 1404 subsurface assuming that there is no boundary (all material is the same as  
 1405 the subsurface) is indicated by  $\Phi_{eth,ss}^*$  and is given in Equation B.6. The  
 1406 difference between the hypothetical equilibrium flux in the air ( $\Phi_{eth,a}^*$ ) and  
 1407 the hypothetical equilibrium flux in the subsurface ( $\Phi_{eth,ss}^*$ ) is  $\Delta\Phi_{eth,ss}^*$ . The  
 1408 physical cause of the difference between the fluxes (no interface vs interface)  
 1409 is the effect of diffusion. This is shown mathematically in Equation B.7 and  
 1410 graphically in Figure B.6.

$$\Phi_{eth,ss}^*(Z) = P_f(0) \frac{R_{eth,ss}}{\Sigma_{eth,ss} - D_{eth,ss}/\Lambda_{f,e}^2} \quad (\text{B.6})$$

$$\Delta\Phi_{eth,ss}^* = \Phi_{eth,a}^* - \Phi_{eth,ss}^* = -\Delta\Phi_{eth,a}^* \quad (\text{B.7})$$

1411 For the purposes of this initial solution, photodisintegration and other  
 1412 neutron-producing interactions are neglected. The diffusion-like behavior of  
 1413 low-energy neutrons means that the diffusion equation, in addition to the  
 1414 production equations, must be solved in order to predict the appropriate  
 1415 amount of cosmogenic nuclide from this type of production. The solution to  
 1416 the coupled differential equations (originally solved in Phillips et al. (2001))  
 1417 yields Equation B.8.

$$\Phi_{eth,ss} = S_T S_{el,s} \Phi_{eth,ss}^* \exp\left(-\frac{Z}{\Lambda_{f,e}}\right) + (F\Delta\Phi)_{eth,ss}^* \exp\left(-\frac{|Z|}{L_{eth,ss}}\right), \quad (\text{B.8})$$

1418 where the physical meaning of the  $(F\Delta\Phi)_{eth,ss}^*$  term (Equation B.9) is  
 1419 the difference between the actual observed flux (with an interface present)  
 1420 and the flux that would be observed at the surface ( $Z=0$ ) if all materials  
 1421 were the same as those in the subsurface. This can also be formulated for  
 1422 the air, as seen in Equation E.12.  $L_{eth,ss}$  (eqn E.19) is the diffusion length  
 1423 for epithermal neutrons in the subsurface and the corresponding parameter  
 1424 in the atmosphere,  $L_{eth,a}$ , is shown in Equation E.20.  $S_{el,s}$  is the scaling  
 1425 factor for spallation reactions, as the flux is derived from the high-energy  
 1426 component.

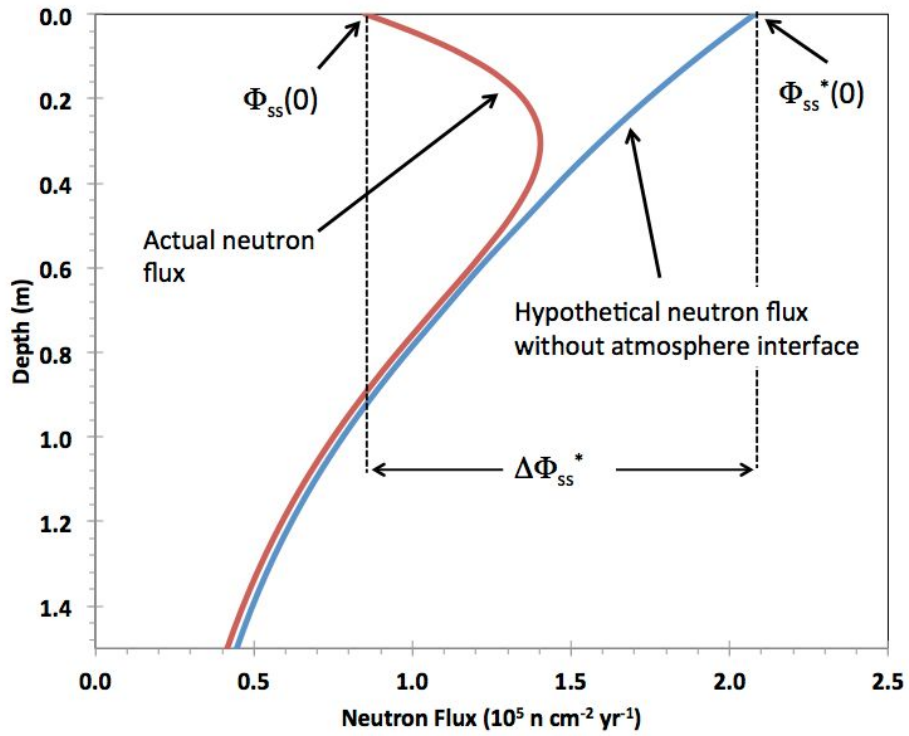


Figure B.6: Thermal-neutron flux profile calculated for standard granite from Fabryka-Martin (1988), illustrating the physical meaning of the terms  $\Phi_{ss}(0)$ ,  $\Phi_{ss}^*(0)$ , and  $\Delta\Phi_{ss}^*$ . The physical meaning is equivalent for both thermal and epithermal neutron fluxes.

$$(F\Delta\Phi)_{eth,ss}^* = \frac{\Delta\Phi_{eth,ss}^* D_{eth,a}/L_{eth,a} - \Delta\Phi_{eth,a}^{**} D_{eth,ss}/\Lambda_{f,e}}{D_{eth,a}/L_{eth,a} + D_{eth,ss}/L_{eth,ss}}, \quad (\text{B.9})$$

1427 where:

$$\Delta\Phi_{eth,a}^{**} = \Delta\Phi_{eth,ss}^* - \frac{D_{eth,a}}{D_{eth,ss}} \Phi_{eth,a}^* \quad (\text{B.10})$$

1428 *Appendix B.3. Thermal Neutrons*

1429 Cosmogenic thermal neutrons are produced as a result of the moderation  
 1430 of cosmogenic epithermal neutrons (in other words, cosmogenic epithermal  
 1431 neutrons lose energy through collisions with atoms in the subsurface and end  
 1432 up as thermal neutrons, having only the ambient energy imparted by ordi-  
 1433 nary thermal vibration). The source term for thermal-neutron production is  
 1434 therefore the epithermal neutron distribution with depth. The production  
 1435 equations for thermal neutron pathways are analogous to those for epither-  
 1436 mal neutrons. In the general production equation, the form is very similar  
 1437 with many parameters being replaced by ones specific for thermal neutrons  
 1438 instead of epithermal neutrons. The production rate ( $P_{th,m}$ ) for thermal  
 1439 neutrons is shown in Equation B.11 (Gosse & Phillips, 2001).

$$P_{th,ss,m} = \frac{f_{th,ss,m}}{\Lambda_{th,ss}} \Phi_{th,ss,total}(Z), \quad (\text{B.11})$$

1440 where  $f_{th,ss,m}$  is the fraction of absorbed thermal neutrons that are taken  
 1441 up by element k to produce nuclide m (eqn E.32);  $\Phi_{th,ss,total}$  is the thermal  
 1442 neutron flux (eqn B.13); and  $\Lambda_{th,ss}$  is the effective thermal neutron attena-  
 1443 tion length (Equation E.33).

1444 The distribution for thermal neutrons in the subsurface (Equation B.12)  
 1445 is also similar to that of epithermal neutrons, except that the thermal neutron  
 1446 source is assumed to be only neutrons moderated from the epithermal energy  
 1447 range.

$$D_{th,ss} \frac{d^2 \Phi_{th,ss}}{dZ^2} = \frac{\Phi_{th,ss}}{\Lambda_{th,ss}} - R_{th,ss} \frac{p(E_{th})_a}{\Lambda_{eth,ss}} [\Phi_{eth,ss}^* \exp(-\frac{Z}{\Lambda_{f,e}}) + (F\Delta\Phi)_{eth,ss}^* \exp(-\frac{|Z|}{L_{eth,ss}})], \quad (\text{B.12})$$

1448 where  $D_{th,ss}$  (Equation E.29) is the diffusion coefficient for thermal neu-  
 1449 trons;  $R_{th,ss}$  is the ratio of thermal neutron production in the rock to that in  
 1450 the atmosphere (Equation E.38). The term  $p(E_{th})_a$  is the resonance escape  
 1451 probability of a neutron from the epithermal energy range in the atmosphere  
 1452 (Equation E.24), with the corresponding subsurface term shown in Equation  
 1453 E.23.

1454 The equations described above can be solved for the thermal neutron  
 1455 flux using the same boundary conditions assumed in the epithermal problem.  
 1456 The thermal neutron flux, discounting muon-induced neutrons, is shown in  
 1457 Equation B.13.

$$\begin{aligned} \Phi_{th,ss} = S_T S_{el,s} \Phi_{th,ss}^* \exp\left(-\frac{Z}{\Lambda_{f,e}}\right) + (\mathcal{F} \Delta \Phi)_{eth,ss}^* \exp\left(-\frac{|Z|}{L_{eth,ss}}\right) \\ + (\mathcal{F} \Delta \Phi)_{th,ss}^* \exp\left(-\frac{|Z|}{L_{th,ss}}\right) \end{aligned} \quad (\text{B.13})$$

1458 where:

$$\Phi_{th,ss}^* = \frac{p(E_{th})_a R_{th,ss} \Phi_{eth,ss}^*}{\Lambda_{eth,ss} (\Sigma_{th,ss} - \frac{D_{th,ss}}{\Lambda_{eth,ss}^2})} \quad (\text{B.14})$$

$$(\mathcal{F} \Delta \Phi)_{eth,ss}^* = \frac{p(E_{th})_a R_{th,ss} (F \Delta \Phi)_{eth,ss}^*}{\Lambda_{eth,ss} (\Sigma_{th,ss} - D_{th,ss}/L_{eth,ss}^2)} \quad (\text{B.15})$$

$$\begin{aligned} (\mathcal{F} \Delta \Phi)_{th,ss}^* = [D_{th,a} \left( \frac{\Phi_{th,a}^*}{\Lambda_{f,e}} - \frac{(\mathcal{F} \Delta \Phi)_{eth,a}^*}{L_{eth,a}} \right) \\ - D_{th} \left( \frac{\Phi_{th,ss}^*}{\Lambda_{f,e}} - \frac{(\mathcal{F} \Delta \Phi)_{eth,ss}^*}{L_{eth,ss}} \right) \\ + \frac{D_{th,a}}{L_{th,a}} (\Delta \Phi_{th,ss}^* + \Delta (\mathcal{F} \Delta \Phi)_{eth,ss}^*)] / \left( \frac{D_{th,ss}}{L_{th,ss}} + \frac{D_{th,a}}{L_{th,a}} \right) \end{aligned} \quad (\text{B.16})$$

1459 In Equation B.16, additional parameters of  $\Delta \Phi_{th,ss}^*$  and  $\Delta (\mathcal{F} \Delta \Phi)_{eth,ss}^*$   
 1460 are described in Equations E.31 and E.4, respectively.  $S_{el,s}$  is the scaling  
 1461 factor for spallation reactions.

#### 1462 *Appendix B.4. Muons*

1463 Muons are unstable, charged subatomic particles with a mass of about 207  
 1464 times that of an electron and a mean life of about 2.2 s. They are produced by

1465 decay of charged pions and K mesons, which in turn result from the interac-  
1466 tion of high-energy cosmic-ray protons with matter in the atmosphere and the  
1467 solid earth (Lal & Peters, 1967). Cosmic-ray muons possess a wide spectrum  
1468 of energies and the nature of their interaction with atomic nuclei depends  
1469 strongly on energy. Lower energy (“slow”) muons can participate in muon-  
1470 capture reactions. The muon-capture reactions can release neutrons that  
1471 later participate in neutron-capture reactions. Higher energy (“fast”) muons  
1472 can produce nuclear transmutations through inelastic scattering reactions,  
1473 including both primary scattering reactions by the muons themselves and  
1474 secondary ones by hadrons and photons released as a result of the primary  
1475 muon interaction. The hadrons released include neutrons, and neutrons are  
1476 also produced by gamma rays from muon-induced bremsstrahlung reactions  
1477 (emission of electromagnetic radiation from an atomic nucleus stimulated  
1478 by deflection of an energetic charged particle passing close to the nucleus).  
1479 The energetic bremsstrahlung gamma rays can produce neutrons if they par-  
1480 ticipate in  $(\gamma, n)$  reactions with the nuclei of other atoms. These neutrons  
1481 also can later participate in neutron-absorption reactions. Muons can thus  
1482 induce the production of the nuclides modeled by CRONUScalc by means  
1483 of a wide variety of reactions (Charalambus, 1971; Fabryka-Martin, 1988;  
1484 Gaisser, 1990; Heisinger et al., 2002a,b).

1485 Although the cosmic-ray muon flux is larger than the hadron flux at the  
1486 earth’s surface, the rate of interaction is much lower. The muonic component  
1487 of the cosmic radiation is thus much more penetrating than the hadronic  
1488 component. The slow component of the muon flux tends to be lost more  
1489 rapidly due to muon-capture reactions and thus, although the magnitude  
1490 of the flux decreases with depth below the earth’s surface, the average en-  
1491 ergy increases. Whereas the hadron flux is important for cosmogenic-nuclide  
1492 production down to about  $1,000 \text{ g cm}^{-2}$ , the slow-muon flux is important  
1493 down to about  $2,500 \text{ g cm}^{-2}$  and nuclides produced by the fast-muon flux  
1494 are detectable down to  $10,000 \text{ g cm}^{-2}$ . The penetration of muons producing  
1495 cosmogenic nuclides is often characterized by an attenuation length employed  
1496 in an exponential depth-dependent equation (e.g., Braucher et al. 2013), but  
1497 due to the continuous hardening of the muon energy spectrum with depth,  
1498 the muon flux does not have an exponential dependence on depth and the  
1499 apparent attenuation length will increase as the depth of the measurements  
1500 increases.

1501 Muon contributions to total production are typically small at the surface,  
1502 but become predominant at depths exceeding  $\sim 1,000 \text{ g cm}^{-2}$ . Accurate

1503 calculation of muogenic production is thus important for sampling sites with  
1504 large erosion rates or depth profiles. Accurate muon production formulations  
1505 are also necessary for depth profiles deeper than about 3 m (Stone et al., 1998;  
1506 Granger & Smith, 2000), where the simultaneous evaluation of spallogenic  
1507 and muogenic fractions offers the opportunity to uniquely determine both  
1508 age and erosion rate (Braucher et al., 2009).

1509 The original CRONUS-Earth calculator of Balco et al. (2008) imple-  
1510 mented the Heisinger et al. (2002a,b) muon model as an improvement over  
1511 the more empirical formulation in Stone et al. (1998). However, soon after  
1512 Heisinger’s publications, Braucher et al. (2003) used a deep core to provide  
1513 evidence that the parameters specified by Heisinger et al. (2002a,b) overes-  
1514 timated actual  $^{10}\text{Be}$  production by fast muons by approximately a factor of  
1515 two. This was supported by additional profile data measured by Braucher  
1516 et al. (2011) and by Kim & Englert (2004), as well as reanalysis of previ-  
1517 ously published deep profile data by Braucher et al. (2013). This result has  
1518 been confirmed by a deep profile drilled in a very low-erosion environment at  
1519 Beacons Hills, Antarctica, by the CRONUS-Earth Project (Fig 1 in Phillips  
1520 et al., 2015). CRONUScalc employs the Heisinger formulation for calculation  
1521 of the subsurface muon flux for all nuclides, but uses calibrated production  
1522 parameters obtained by fitting to the Beacon Heights profile data for  $^{10}\text{Be}$   
1523 and  $^{26}\text{Al}$ .

1524 The muon-flux model of Sato et al. (2008), combined with the previous  
1525 Heisinger muon production equations and CRONUS-Earth data, has been  
1526 employed to formulate a new hybrid muon production model that combines  
1527 aspects of each of these models. The CRONUScalc muon code has been  
1528 constructed by N. Lifton by modifying the Heisinger muon implementation  
1529 described in Balco et al. (2008) and supplemental materials. The procedure  
1530 followed by the code is summarized here along with the relevant equations.

1531 The muon flux at the surface is scaled based on the Lifton-Sato-Dunai  
1532 model (Lifton et al., 2014). The scaling is done by computing the omnidirec-  
1533 tional muon flux as a function of energy at the site and at a reference location  
1534 (SLHL) and dividing the site flux by the reference flux. The CRONUScalc  
1535 muon module initially calculates the omnidirectional muon flux at SLHL and  
1536 at the site of interest using the PARMA-based equations (Sato et al., 2008).  
1537 Energy-dependent scaling factors are then calculated as the ratio of site flux  
1538 to that at SLHL for each energy interval. A single scaling factor is similarly  
1539 calculated for the stopping muon flux at the surface - we define stopping  
1540 muons as those that have ranges less than  $10 \text{ g/cm}^2$  (equivalent to ca. 40



1541 MeV energy) (Groom et al., 2001). The vertical muon flux at SLHL is calcu-  
 1542 lated using the equation presented in Equation 3 in Heisinger et al. (2002a)  
 1543 and shown here as Equation B.17.

$$\phi_{\nu,0}(Z) = \frac{a}{(Z + b)([Z + 1000]^{1.66} + c)} e^{dZ}, \quad (\text{B.17})$$

1544 where the coefficients are as follows:  $a = 5.401 \times 10^7$ ,  $b = 21000$ ,  $c =$   
 1545  $1.567 \times 10^5$ ,  $d = -5.5 \times 10^{-6}$ . This formulation is only valid down to 200,000  
 1546  $\text{g/cm}^2$  ( $\sim 750$  m depth) and the alternative formulation provided in Balco  
 1547 (2008 supplemental material - Eqns. 49-51) should be used for deeper appli-  
 1548 cations.

1549 The stopping rate of the vertically incident muons ( $R_{\nu,0}(Z)$ ) is calculated  
 1550 by equivalence to the range spectrum of the muons at the surface. Equation  
 1551 B.18 shows this calculation.

$$R_{\nu,0}(Z) = \frac{d}{dz}(\phi_{\nu,0}(Z)) = -5.401 \times 10^7 \left[ \frac{bc \frac{da}{dz} - a \left( \frac{db}{dz} c + \frac{dc}{dz} b \right)}{b^2 c^2} \right], \quad (\text{B.18})$$

1552 where  $a = e^{-5.5 \times 10^{-6} z}$ ;  $b = (z + 21000)$ ;  $c = (z + 1000)^{1.66} + 1.567 \times 10^5$ ;  
 1553  $\frac{da}{dz} = -5.5 \times 10^{-6} e^{-5.5 \times 10^{-6} z}$ ;  $\frac{db}{dz} = 1$ ;  $\frac{dc}{dz} = 1.66(z + 1000)^{0.66}$  (Balco et al.,  
 1554 2008; Heisinger et al., 2002b).

1555 The vertical muon flux as a function of depth ( $\phi_{\nu}(Z)$ ) at the site is found  
 1556 by numerically integrating the stopping rate from infinite depth to the depth  
 1557 of interest (Equation B.19).

$$\phi_{\nu}(Z) = \int_Z^{\infty} R_{\nu}(x) dx \quad (\text{B.19})$$

1558 The vertical muon flux is converted to total muon flux at the site following  
 1559 Heisinger et al. (2002b) (Equation B.20), but modified to use depth units of  
 1560  $\text{g/cm}^2$  by Balco et al. (2008), as shown in Equation B.21.

$$\phi(Z, \theta) = \phi_{\nu}(Z) \cos^{n(Z)} \theta \quad (\text{B.20})$$

$$n(Z) = 3.21 - 0.297 \ln \left( \frac{Z}{100} + 42 \right) + Z * 1.21 \times 10^{-5} \quad (\text{B.21})$$

1561 The total muon flux at a given depth ( $\phi_{\mu}(Z)$ ) is given by Equation B.22.

$$\phi_{\mu}(Z) = \frac{2\pi}{n(Z + \delta Z) + 1} \phi_{\nu}(Z) \quad (\text{B.22})$$

1562 where  $\delta Z$  is the difference between the site of interest and sea level in units  
 1563 of  $\text{g cm}^{-2}$ . The total muon stopping rate as a function of depth ( $R(Z)$ ) can  
 1564 be calculated by Equation B.23, following Balco (2007). The total stopping  
 1565 rate in muons  $\text{g}^{-1} \text{s}^{-1}$  is converted to the negative muon stopping rate by  
 1566 accounting for the percentage of all stopped muons that are negative stopped  
 1567 muons (44%) and then converting the units to muons  $\text{g}^{-1} \text{yr}^{-1}$ . In both flux  
 1568 calculations (total muon flux and stopped negative muon flux) the values are  
 1569 calculated so that the flux is a positive value.

$$R(Z) = \frac{2\pi}{n(Z + \delta Z) + 1} R_{\nu}(Z) - \phi_{\nu}(Z)(-2\pi) * \\ (n(Z + \delta Z) + 1)^2 \left[ \frac{-0.297 \times 10^{-2}}{\frac{Z + \delta Z}{100} + 42} + 1.21 \times 10^{-5} \right] \quad (\text{B.23})$$

#### 1570 *Appendix B.4.1. Fast Muon Production*

1571 Production from fast muons as a function of depth is calculated using the  
 1572 formulas in Heisinger et al. (2002b), with the general production described  
 1573 by Equation B.24.

$$P_{\mu,fast} = S_T \phi_{\mu,total}(Z) \beta(Z) (\bar{E}(Z))^{\alpha} \sigma_0 N_{t,i} \quad (\text{B.24})$$

1574 Where the factor  $\beta(Z)$  is a function of the mean total muon energy and  
 1575 is shown in Equation B.25 and  $\bar{E}$  is defined as the mean muon energy at a  
 1576 given depth  $Z$  and is shown in Equation B.26.  $N_{t,i}$  is the number density of  
 1577 the atoms in the target element (in units of  $\text{at/g}$ ). This value is a constant  
 1578 for each nuclide unless the composition of the target changes, as it does for  
 1579  $^{36}\text{Cl}$ .

$$\beta(Z) = 0.846 - 0.015 \log\left(\frac{Z}{100} + 1\right) + 0.003139 \left(\log\left(\frac{Z}{100} + 1\right)\right)^2 \quad (\text{B.25})$$

$$\bar{E}(Z) = 7.6 + 321.7 * (1 - \exp(-8.059 \times 10^{-6} Z)) + 50.7 (1 - \exp(-5.05 \times 10^{-7} Z)) \quad (\text{B.26})$$

1580 In Heisinger et al. (2002b), the experimentally-determined value of  $\sigma_{190}$   
 1581 (i.e., the energy-dependent reaction cross-section measured at 190 GeV) was  
 1582 used to calculate the value for  $\sigma_0$  (the cross-section at 1 GeV) using Equation  
 1583 B.27, which can then be used to calculate the production from muons for a  
 1584 particular nuclide, as shown in Equation B.24. Alpha ( $\alpha$ ) is an only weakly  
 1585 energy-dependent coefficient that parameterizes the energy dependence of  
 1586 the cross-section on muon energy, with low values indicating a weaker de-  
 1587 pendence and higher values a stronger dependence. Based on a survey of the  
 1588 literature, Heisinger et al. (2002b) adopted a value of  $\alpha \approx 0.75$ , but their  
 1589 own experimental evidence supported a value of about 0.93.  $^{26}\text{Al}/^{10}\text{Be}$  ra-  
 1590 tios measured by Kim & Englert (2004) in a profile down to 50,000 g/cm<sup>-2</sup>  
 1591 depth are higher than predicted by Heisinger et al. (2002b), supporting a  
 1592 larger value of  $\alpha$ . Experimental results are permissive of values between 0.75  
 1593 and >1.0 (Heisinger et al., 2002b) so the CRONUS-Earth Project chose a  
 1594 value of  $\alpha = 1.0$ . By assuming that  $\alpha$  equals one,  $\beta$  will also be equal to  
 1595 one. Heisinger et al. (2002b) reported experimentally determined values of  
 1596  $\sigma_{190}$  for many of the nuclides of interest including  $^{26}\text{Al}$ ,  $^{10}\text{Be}$ ,  $^{14}\text{C}$ , and  $^{36}\text{Cl}$   
 1597 from calcium. Note that there is no value for  $^{36}\text{Cl}$  from potassium. However,  
 1598 application of these values in many cases produced calculated concentrations  
 1599 in excess of what has been measured in deep profiles (Braucher et al., 2011,  
 1600 2013).

1601 Rather than using parameters estimated from laboratory muon irradiations,  
 1602 the CRONUS-Earth Project has adopted values calibrated from nuclide-  
 1603 concentration profiles at carefully selected sites whenever possible (Fig 1 in  
 1604 Phillips et al., 2015; Borchers et al., 2015; Marrero, 2012).  $\sigma_0$  was selected as  
 1605 the calibration parameter for the production of nuclides by muon reactions,  
 1606 as discussed in Marrero (2012). This was done mainly for two reasons. First,  
 1607  $\sigma_0$  is the only nuclide-dependent parameter in the fast production equation,  
 1608 so it is the logical choice. Second, by directly calibrating the  $\sigma_0$  parameter,  
 1609 any dependence on the accuracy of the conversion from  $\sigma_{190}$  to  $\sigma_0$  is elim-  
 1610 inated. Equation B.27 was used to calculate initial starting parameters for  
 1611 the  $\sigma_0$  calibration.

$$\sigma(E) = \sigma_0 E^\alpha, \tag{B.27}$$

1612 where E is the muon energy in GeV.

1613 *Appendix B.4.2. Slow Negative Muon Capture Production*

1614 Nuclide production by slow negative muon capture ( $P_{\mu-}$ ) is described by  
 1615 Equation B.28, originally from Charalambus (1971) and discussed in detail  
 1616 for  $^{36}\text{Cl}$  by Stone et al. (1998). The production rate depends on the stopping  
 1617 rate of negative muons ( $\phi_{\mu-}$ ) as well as the nuclide-dependent factors ( $f_{i,C}$ ,  
 1618  $f_{i,D}$ ,  $f_i^*$ ).  $f_{i,D}$  is the fraction of muons stopped by element  $k$  and absorbed  
 1619 by the nucleus before decay of the muon.  $f_{i,C}$ , the compound factor, rep-  
 1620 represents the fraction of the muons that are captured by a target element (as  
 1621 opposed to the other elements present) within the bulk rock. The formula  
 1622 for the compound factor is taken from Charalambus (1971) and the values  
 1623 are consistent with those used by Heisinger et al. (2002a). In the case of  
 1624 nuclides measured in a rock of uniform composition, the compound factor  
 1625 is a constant parameter; however, for cases where the lithology, and hence  
 1626 the chemical composition, is spatially variable, the compound factor will also  
 1627 vary. The value for  $f_{i,C}$  can be calculated using the formula in Equation E.40  
 1628 and the values in von Egidy & Hartmann (1982).

$$P_{\mu-} = S_T \phi_{\mu-}(Z) f_{i,C} f_{i,D} f_i^* \quad (\text{B.28})$$

1629 The remaining parameter,  $f_i^*$ , the particle emission channel probability,  
 1630 is the probability that the excited nucleus of the target atom will emit the  
 1631 proper particle to result in transformation to the nuclide of interest. Heisinger  
 1632 et al. (2002a) report experimentally determined  $f_i^*$  values for the production  
 1633 of  $^{26}\text{Al}$  (from Si),  $^{10}\text{Be}$  and  $^{14}\text{C}$  (from O), and  $^{36}\text{Cl}$  (from K and Ca). As for  
 1634 the fast muon production reactions, the parameters of Heisinger et al. (2002a)  
 1635 tend to overestimate nuclide concentrations measured in depth profiles (Fig  
 1636 1 in Phillips et al., 2015; Braucher et al., 2011), so  $f_i^*$  for  $^{10}\text{Be}$ ,  $^{26}\text{Al}$ ,  $^{36}\text{Cl}$   
 1637 were calibrated by fitting to the measured CRONUS-Earth profiles (Phillips  
 1638 et al., 2015; Borchers et al., 2015; Marrero, 2012).

1639 *Appendix B.4.3. Muon-induced Neutrons*

1640 As muons react with atomic nuclei in the subsurface, neutrons are re-  
 1641 leased. These can, in turn, react with other nuclei to produce cosmogenic  
 1642 nuclides of interest. The principal reactions responsible for the production of  
 1643 neutrons are muon capture and ( $\gamma$ , n) reactions resulting from interaction of  
 1644 high-energy gamma from muon-induced bremsstrahlung reactions with the  
 1645 nuclei of atoms in the subsurface. In order to calculate the nuclide produc-  
 1646 tion due to these muonic neutrons, it is necessary to know the muon flux as

1647 a function of depth. Due to the capabilities of the muon model, the quan-  
 1648 tification of fluxes has improved and they need no longer be approximated  
 1649 using a simple exponential equation (Stone et al., 1998), as was previously  
 1650 done in most models, including CHLOE (Phillips & Plummer, 1996) and the  
 1651 Schimmelpfennig et al. (2009) calculator, but instead are directly calculated  
 1652 using Equation B.29. The muon module, described in the previous section, is  
 1653 used to calculate the negative muon stopping rate ( $\phi_{\mu-}(Z)$ ) and total muon  
 1654 flux ( $\phi_{\mu f}(Z)$ ) terms at a given depth.

$$P_{n,\mu}(Z) = Y_s \phi_{\mu-}(Z) + 5.8 \times 10^{-6} \phi_{\mu f}(Z), \quad (\text{B.29})$$

1655 where  $Y_s$  is the average neutron yield per stopped negative muon (Fabryka-  
 1656 Martin, 1988).

1657 Near the atmosphere/subsurface interface, muon-induced low-energy neu-  
 1658 trons are assumed to follow the same distribution as the spallation-induced  
 1659 neutrons. Although the muon-induced neutron flux near the surface is not  
 1660 in equilibrium with the production rate due to diffusion, the diffusion is  
 1661 occurring based on the total concentration of neutrons at the surface. The  
 1662 dominant source of neutrons is spallation reactions, so the muons are assumed  
 1663 to follow the same pattern as the spallation-induced neutrons, leading to the  
 1664 incorporation of the muogenic neutrons into the epithermal neutron flux as  
 1665 shown in Equation B.30.

$$\begin{aligned} \Phi_{\text{eth,ss}}(Z) = & S_T S_{el,s} \Phi_{\text{eth,ss}}^* \exp\left(-\frac{Z}{\Lambda_{f,e}}\right) \\ & + (1 + R_\mu(0) R_{\text{eth,ss}}) (F \Delta \Phi)_{\text{eth,ss}}^* \exp\left(-\frac{Z}{L_{\text{eth,ss}}}\right) \\ & + R_\mu(Z) \Phi_{\text{eth,ss}}^* \end{aligned} \quad (\text{B.30})$$

1666 There are two different values used in the code for the muon-induced  
 1667 neutron factor,  $R_\mu$ .  $R_\mu(Z)$  is defined in Equation B.31. In the parts of the  
 1668 equation dealing with epithermal neutrons, the surface production rate of  
 1669 the muogenic neutrons ( $R_\mu(0)$ ) is used because of the assumption that the  
 1670 production follows the same trend as the spallogenic neutrons. For the parts  
 1671 of the equation dependent on the attenuation at depth of the muon flux, the  
 1672 actual values for  $R_\mu(Z)$  are calculated from the muon module and used in  
 1673 the equation.

$$R_\mu(Z) = \frac{S_{el,\mu} P_{n,\mu}(Z)}{S_{el,eth} P_f(0) R_{eth}} \quad (\text{B.31})$$

1674 The code calculates the epithermal neutron flux and the subsequent cos-  
 1675 mogenic nuclide production by combining the muon-induced neutrons with  
 1676 the original epithermal neutron production equation, Equation B.8, to pro-  
 1677 duce the total epithermal neutron production for nuclide m, as shown in  
 1678 Equation B.32.

$$\begin{aligned}
 P_{\text{eth,ss,m}}(Z) = & \frac{f_{\text{eth,ss}} \Phi_{\text{eth,ss,total}}}{\Lambda_{\text{eth,ss}}} = \frac{f_{\text{eth,ss}}}{\Lambda_{\text{eth,ss}}} \left\{ \Phi_{\text{eth,ss}}^* \exp\left(-\frac{Z}{\Lambda_{f,e}}\right) \right. \\
 & + (1 + R_\mu(0) R_{\text{eth,ss}}) (F \Delta \Phi)_{\text{eth,ss}}^* \exp\left(-\frac{z}{L_{\text{eth,ss}}}\right) \\
 & \left. + R_\mu(Z) \Phi_{\text{eth,ss}}^* \right\} \quad (\text{B.32})
 \end{aligned}$$

1679 Similar considerations for muon-induced neutrons must be made for the  
 1680 thermal energy range. Some of the epithermal-range neutrons produced by  
 1681 muon interactions lose enough energy to become thermal neutrons. The  
 1682 contribution of these muon-induced neutrons to the thermal flux is shown  
 1683 in Equation B.33. Once again, the muon-induced neutrons are assumed to  
 1684 follow the same trends as the spallogenic neutrons and are scaled appropri-  
 1685 ately using only the surface value of  $R'_\mu(Z)$  for the spallogenic parts of the  
 1686 equation. For the neutron-dependent term, the actual values for each depth  
 1687 are calculated. The final equation for the thermal neutron flux is shown in  
 1688 Equation B.34.

$$R'_\mu(Z) = \frac{p(E_{th})_a}{p(E_{th})} R_\mu(Z) \quad (\text{B.33})$$

$$\begin{aligned}
\Phi_{th,ss,total} = S_T S_{el,s} & \left\{ \Phi_{th,ss}^* \exp\left(-\frac{Z}{\Lambda_{f,e}}\right) + \right. \\
& (1 + R'_\mu(0)) (\mathfrak{S}\Delta\Phi)_{eth,ss}^* \exp\left(-\frac{Z}{L_{eth,ss}}\right) \\
& + (1 + R'_\mu(0)R_{th,ss}) (\mathfrak{S}\Delta\Phi)_{th,ss}^* \exp\left(-\frac{Z}{L_{eth,ss}}\right) + \\
& \left. R'_\mu(Z) \Phi_{th,ss}^* \right\} \quad (B.34)
\end{aligned}$$

1689 The total production of cosmogenic nuclide k via thermal neutron path-  
1690 ways is described by combining Equation B.34 with Equation B.11 and yields  
1691 an equation for total production with depth from thermal neutrons, shown  
1692 in Equation B.35.

$$\begin{aligned}
P_{th,ss,m}(Z) = S_T S_{el,s} \frac{f_{th} \Phi_{th,ss,total}}{\Lambda_{th,ss}} = \frac{f_{th}}{\Lambda_{th,ss}} & \left\{ \Phi_{th,ss}^* \exp\left(-\frac{Z}{\Lambda_{f,e}}\right) \right. \\
& + (1 + R'_\mu(0)) (\mathfrak{S}\Delta\Phi)_{eth,ss}^* \exp\left(-\frac{Z}{L_{eth,ss}}\right) \\
& + (1 + R'_\mu(0)R_{th}) (\mathfrak{S}\Delta\Phi)_{th,ss}^* \exp\left(-\frac{Z}{L_{eth,ss}}\right) \\
& \left. + R'_\mu(Z) \Phi_{th,ss}^* \right\} \quad (B.35)
\end{aligned}$$

1693 *Appendix B.5. Radiogenic Production*

1694 “Radiogenic production” in this context refers to the generation of low-  
1695 energy neutrons by reactions related to the radioactive decay or spontaneous  
1696 fission of U or Th, and the subsequent absorption of those neutrons to pro-  
1697 duce nuclides of interest, principally <sup>36</sup>Cl. The radiogenic low-energy neutron  
1698 flux is assumed to be in equilibrium with the concentrations of uranium (U)  
1699 and thorium (Th) in the rock. This component is quantified using measured  
1700 concentrations of U and Th and the method described in Fabryka-Martin  
1701 (1988), which is based on the formulations developed by Feige et al. (1968).  
1702 The uranium and thorium  $\alpha$ -decay chain members produce alpha particles

1703 ( $\alpha$ ) as they decay. The alpha particles react with light nuclei in the rock  
 1704 matrix to produce low-energy neutrons. In turn, the neutrons can react with  
 1705 target elements in the rock in the same way that cosmogenically produced  
 1706 neutrons react to produce nuclides such as  $^{36}\text{Cl}$ . The equations for calcu-  
 1707 lating this contribution to the total nuclide inventory within a sample are  
 1708 provided in detail in Fabryka-Martin (1988) and are summarized here.

1709 The radiogenic production of nuclides is given by Equation B.36. The  
 1710 elements with the maximum yield of neutrons due to alpha particle reaction  
 1711 are Be, B, F, and Li. However, due to the low concentration of these elements  
 1712 in most rocks, the largest concentrations of neutrons result from targets  
 1713 with larger matrix concentrations, such as Al, Si, Mg, O, and Na. The  
 1714 concentrations of both O and H are calculated from the oxide measurements  
 1715 performed on the other elements.

$$P_r = P_{eth,r}f_{eth} + P_{th,r}f_{th} \quad (\text{B.36})$$

1716 where  $P_r$  is the total radiogenic production from all mechanisms in a par-  
 1717 ticular sample;  $P_{eth,r}$  is the total radiogenic epithermal neutron production  
 1718 (Equation B.37);  $P_{th,r}$  is the total radiogenic thermal neutron production  
 1719 (Equation B.38).

1720 Although the concentrations of the largest producers of neutrons are the  
 1721 most important elements to quantify, the remaining rock matrix composition  
 1722 must still be quantified in addition to the elements listed above so that all  
 1723 elements can be used to calculate the stopping power of the rock. In par-  
 1724 ticular, there are several elements, such as boron and gadolinium, that have  
 1725 large thermal neutron absorption cross-sections, meaning that they have a  
 1726 large probability of absorbing neutrons (from both radiogenic and cosmo-  
 1727 genic sources) (Fabryka-Martin, 1988). This decreases the actual amount  
 1728 of  $^{36}\text{Cl}$  formed within the rock because these other elements intercept the  
 1729 neutrons prior to formation of  $^{36}\text{Cl}$ .

$$P_{eth,r} = (P_{n,\alpha} + P_{n,sf})(1 - p(E_{th})), \quad (\text{B.37})$$

$$P_{th,r} = (P_{n,\alpha} + P_{n,sf})p(E_{th}), \quad (\text{B.38})$$

1730 where  $P_{n,\alpha}$  is the production rate of neutrons from alpha particles in  
 1731 neutrons  $\text{g}^{-1} \text{yr}^{-1}$  (Equation B.39).  $P_{n,sf}$  is the neutron production rate due  
 1732 to the spontaneous fission of  $^{238}\text{U}$  and can be calculated as  $0.429[\text{U}]$ , where  
 1733  $[\text{U}]$  is the concentration of uranium in ppm.



$$P_{n,\alpha} = X[U] + Y[Th], \quad (\text{B.39})$$

1734 where [Th] is the thorium concentration in ppm. X and Y are neutron  
 1735 production factors related to the light isotope composition of the rock matrix  
 1736 and are described in Equations B.40 and B.41, respectively. These were  
 1737 originally described by Feige et al. (1968).

$$X = \frac{\sum k S_k F_{k,bulk} Y_n^U}{\sum k S_k F_{k,bulk}}, \quad (\text{B.40})$$

$$Y = \frac{\sum k S_k F_{k,bulk} Y_n^{Th}}{\sum k S_k F_{k,bulk}}, \quad (\text{B.41})$$

1738 where  $S_k$  is the mass stopping power of element k for  $\alpha$ -particles of a  
 1739 given energy;  $Y_n^U$  and  $Y_n^{Th}$  are the neutron yields of element i per ppm U or  
 1740 Th in equilibrium;  $F_{k,bulk}$  is the fractional abundance of element k in ppm in  
 1741 the bulk rock.

## 1742 Appendix C. Scaling

1743 Cosmogenic nuclide scaling applies the physics governing the modulation  
 1744 of the cosmic-ray flux by atmospheric mass and the terrestrial and solar  
 1745 magnetic fields to provide production rates as a function of location and  
 1746 exposure time. Numerous scaling frameworks have been proposed in order  
 1747 to correct for latitude, elevation, atmospheric pressure anomalies, dipole and  
 1748 non-dipole geomagnetic field changes, and solar modulation. For all the  
 1749 details of the scaling frameworks themselves, please see the original papers  
 1750 (cited in Table 2); for details of implementation, please see the descriptions  
 1751 in Balco et al. (2008) and Lifton et al. (2014).

1752 The fundamental correction for elevation and latitude is the key part  
 1753 of each scaling framework. The first scaling framework to implement this  
 1754 was Lal (1991). Eventually, Stone (2000) reformulated the original equa-  
 1755 tions to take atmospheric pressure, instead of elevation, as an input. This  
 1756 is still a commonly cited scaling framework. However, the original, time-  
 1757 independent Lal/Stone scaling (abbreviated as St in the code) does not ac-  
 1758 count for changes in production rate that we know are occurring through  
 1759 time due to fluctuations in the terrestrial and solar magnetic fields.

1760 The production rates of cosmogenic nuclides are a function of the mag-  
 1761 netic field strength. As the geomagnetic field of the earth changed in the

1762 past, production rates of the nuclides also changed. This fact has led to the  
1763 development of scaling frameworks that incorporate the geomagnetic history  
1764 of the earth. Dunai (2000, 2001a) (Du) , Desilets et al. (2006b); Desilets &  
1765 Zreda (2003) (De) , and Lifton et al. (2005, 2008) (Li), and Lifton-Sato-Dunai  
1766 (Lifton et al., 2014) (LSD, herein labeled Sf) have all implemented different  
1767 models to incorporate the changing magnetic field. Following Balco et al.  
1768 (2008), we have also provided the time-dependent Lal scaling (Lm, including  
1769 dipole geomagnetic effects as approximated by Nishiizumi et al. (1989)) in  
1770 order to differentiate between the geomagnetic effects and other differences  
1771 in the models.

1772 In CRONUScalc, the geomagnetic history is consistent across all scaling  
1773 frameworks and is summarized in Table 3. The Lifton et al. (2005) and the  
1774 more recent model presented in Lifton et al. (2014) (LSD) also incorporate  
1775 the effects of solar modulation into the scaling framework. For a discussion  
1776 of the uncertainties associated with geomagnetic models, see Section 2.3.

1777 In each scaling framework that incorporates geomagnetic effects, the ap-  
1778 propriate input is cutoff rigidity. However, each scaling framework imple-  
1779 ments the rigidity cutoff calculations differently (see Schimmelpfennig (2009)  
1780 for a summary of these differences). See each original scaling reference for the  
1781 equations for cutoff rigidity. In the program, most of the scaling frameworks  
1782 are taken directly from Balco et al. (2008) and complete descriptions can be  
1783 found in the original calculator supplemental material (Balco et al., 2008).  
1784 For the Sa and Sf models, see the paper by Lifton et al. (2014).

#### 1785 **Appendix D. Comparison of CRONUScalc and Analytical Solu-** 1786 **tions for $^3\text{He}$**

1787 Synthetic  $^3\text{He}$  concentrations were predicted using the analytical solution  
1788 presented in Dunai (2010) for samples undergoing both production and ero-  
1789 sion. The CRONUS-Earth calibrated production rate for ST scaling and the  
1790 erosion rate (Table D.7, column 1) were used to predict the concentration  
1791 (Table D.7, column 2). The resulting CRONUScalc ages for ST scaling are  
1792 presented in Table D.7, column 4. The differences in terms of % are provided  
1793 in the final column of the table. Saturated samples were excluded from com-  
1794 parison. Samples were assumed to be located at SLHL, 0 degrees longitude,  
1795 and have a density of  $2.65 \text{ g/cm}^3$ , shielding of 1, thickness of 0.001 cm, an  
1796 effective attenuation length of  $136 \text{ g/cm}^2$  and were collected in 2014 AD.

Erosion rate (mm/kyr)	Concentration (atoms g <sup>-1</sup> )	Actual age (ka)	Calc age (ka)	% Difference (%)
0	118	0.001	0.001	$4.6 \times 10^{-7}$
0	11821	0.1	0.100	$2.0 \times 10^{-7}$
0	1182137	10	10.000	$-4.9 \times 10^{-7}$
0	5910685	50	50.000	$5.6 \times 10^{-7}$
0	11821370	100	100.000	$5.6 \times 10^{-7}$
0	23642739	200	200.000	$5.6 \times 10^{-7}$
0	47285479	400	400.000	$5.6 \times 10^{-7}$
0	118213696	1000	1000.000	$-7.5 \times 10^{-7}$
0	236427393	2000	2000.000	$-7.5 \times 10^{-7}$
0	354641089	3000	3000.000	$-9.9 \times 10^{-7}$
0	591068482	5000	5000.000	$6.0 \times 10^{-7}$
0	827495875	7000	7000.000	$8.5 \times 10^{-7}$
1	11820	0.1	0.100	$2.0 \times 10^{-7}$
1	1170695	10	10.000	$6.8 \times 10^{-7}$
1	5631906	50	50.000	$5.6 \times 10^{-7}$
1	10741040	100	100.000	$5.6 \times 10^{-7}$
1	19580586	200	200.000	$5.6 \times 10^{-7}$
1	32842095	400	400.000	$5.6 \times 10^{-7}$
1	52026941	1000	1000.000	$7.5 \times 10^{-7}$
1	59441147	2000	2000.000	$2.2 \times 10^{-6}$
1	60497723	3000	3000.000	$8.9 \times 10^{-6}$
1	60669750	5000	5000.014	$2.8 \times 10^{-4}$
1	60673244	7000	7000.662	$9.5 \times 10^{-3}$
10	11810	0.1	0.100	$11.7 \times 10^{-5}$
10	1074104	10	10.000	$1.7 \times 10^{-5}$
10	3776908	50	50.000	$2.7 \times 10^{-5}$
10	5202694	100	100.000	$4.9 \times 10^{-5}$
10	5944115	200	200.000	$2.0 \times 10^{-4}$
10	6064829	400	400.020	$4.9 \times 10^{-3}$

Table D.7: Summary of comparison between analytical solutions for <sup>3</sup>He and CRONUScalc results over a range of erosion rates and exposure ages.

1797 **Appendix E. Glossary of Terms and Equations**

Table E.8: Glossary of terms and equations

Term	Definition
<i>General parameters and subscripts</i>	
bulk	In reference to the bulk rock composition of the sample as opposed to the target (processed) material
$C_k$	Mass concentration of element k [(g element k) (g material) <sup>-1</sup> ]
eth	Subscript used to denote the epithermal production pathway, defined as neutrons with energies of 0.5 eV to 0.1 MeV.
h	Atmospheric depth [g cm <sup>-2</sup> ]
k	Subscript used to denote a particular cosmogenic-producing element
m	Subscript used to denote a particular cosmogenic nuclide
m	Molar concentration
$\mu$	Subscript used to denote the muon production pathway
$\rho$	Density [g cm <sup>-3</sup> ]
s	Subscript used to denote the spallation production pathway
target	In reference to the particular target fraction of the sample, specifically in the case of mineral separates
th	Subscript used to denote the thermal production pathway, defined as neutrons with energies of <0.5 eV.
z	Ordinary linear distance [cm]
Z	Mass depth below the surface [g cm <sup>-2</sup> ]  $Z(z) = \int_0^z \rho(z) dz \quad (\text{E.1})$
<i>Cosmic Rays</i>	
c	Speed of light (see eqn A.1)
e	Particle charge (see eqn A.1)
p	Particle momentum (see eqn A.1)
Continued on next page	

**Table E.8 – continued from previous page**

<b>Term</b>	<b>Definition</b>
$R$	Rigidity of a particle (see eqn A.1)
$S_{el}$	Latitude/Elevation scaling coefficient (see scaling scheme section) [ <i>unitless</i> ]
$S_T$	Topographic scaling coefficient describing the shielding from surrounding topography [unitless]
$\theta$	Inclination angle from the horizontal [ <i>degrees</i> ]
$z_p$	Vertical penetration depth [ $\text{g cm}^{-2}$ ]
	$z_p = \Lambda_{f,p} \cos\phi$ (E.2)

*Spallation*

$I(\theta)$	Intensity. See eqn B.2. $I_0$ is the intensity of I for a sample with 0 dip.
$\Lambda_{f,e}$	Effective attenuation length for fast neutrons. See Appendix B.1.1.
$P_{s,m}$	Production rate for spallation of nuclide m. See eqn 1.
$P_{m,k}$	Production rate of nuclide m from target element k. See eqn 1.
$\theta$	Sample dip/inclination as measured from the horizontal. See eqn B.2.

*Epithermal Production*

$\bar{A}_{ss}$	Average atomic weight of the bulk rock [ $\text{g mol}^{-1}$ ]
	$\bar{A}_{ss} = \frac{\sum_k A_k N_{k,ss,bulk}}{\sum_k N_{k,ss,bulk}}$ (E.3)
$\bar{A}_a$	Average atomic weight of the atmosphere; constant = 14.5 [ $\text{g mol}^{-1}$ ] (Phillips & Plummer, 1996)
$A_k$	Atomic weight of element k [ $\text{g mol}^{-1}$ ]
Continued on next page	

Table E.8 – continued from previous page

Term	Definition
$\Delta(\mathcal{F}\Delta\Phi)_{eth,ss}^*$	<p>Difference between <math>\mathcal{F}\Delta\Phi_{eth}^*</math> in the atmosphere (<math>\mathcal{F}\Delta\Phi_{eth,a}^*</math>) and the subsurface (<math>\mathcal{F}\Delta\Phi_{eth,ss}^*</math>)</p> $\Delta(\mathcal{F}\Delta\Phi)_{eth,ss}^* = (\mathcal{F}\Delta\Phi)_{eth,a}^* - (\mathcal{F}\Delta\Phi)_{eth,ss}^* \quad (\text{E.4})$
$\Delta\Phi_{eth,ss}^*$	<p>Difference between the hypothetical equilibrium epithermal neutron fluxes in atmosphere and rock [neutrons <math>\text{cm}^{-2} \text{yr}^{-1}</math>]</p> $\Delta\Phi_{eth,ss}^* = \Phi_{eth,a}^* - \Phi_{eth,ss}^* \quad (\text{E.5})$
$\Delta\Phi_{eth,a}^*$	<p>Difference between the hypothetical equilibrium epithermal neutron fluxes in atmosphere and rock [neutrons <math>\text{cm}^{-2} \text{yr}^{-1}</math>]</p> $\Delta\Phi_{eth,a}^* = \Phi_{eth,ss}^* - \Phi_{eth,a}^* \quad (\text{E.6})$
$\Delta\Phi_{eth,ss}^{**}$	<p>Adjusted difference between the hypothetical equilibrium epithermal neutron fluxes in atmosphere and rock. [neutrons <math>\text{cm}^{-2} \text{yr}^{-1}</math>]</p> $\Delta\Phi_{eth,ss}^{**} = \Phi_{eth,a}^* - \frac{D_{eth,ss}}{D_{eth,a}} \Phi_{eth,ss}^* \quad (\text{E.7})$
$\Delta\Phi_{eth,a}^{**}$	<p>Adjusted difference between the hypothetical equilibrium epithermal neutron fluxes in atmosphere and rock. [neutrons <math>\text{cm}^{-2} \text{yr}^{-1}</math>]</p> $\Delta\Phi_{eth,a}^{**} = \Phi_{eth,ss}^* - \frac{D_{eth,a}}{D_{eth,ss}} \Phi_{eth,a}^* \quad (\text{E.8})$
Continued on next page	

Table E.8 – continued from previous page

Term	Definition
$D_{eth,ss}$	<p>Diffusion coefficient for epithermal neutrons in subsurface [g cm<sup>-2</sup>]</p> $D_{eth,ss} = [3\Sigma_{sc}(1 - \frac{2}{3\bar{A}})]^{-1} \quad (E.9)$
$D_{eth,a}$	<p>Diffusion coefficient for epithermal neutrons in air [g cm<sup>-2</sup>] can be calculated using values of <math>(\Sigma_{sc,a})=0.3773</math> [cm<sup>-2</sup> g<sup>-1</sup>] (Phillips &amp; Plummer, 1996).</p> $D_{eth,a} = [3\Sigma_{sc,a}(1 - \frac{2}{3\bar{A}})]^{-1} \quad (E.10)$
$(F\Delta\Phi)_{eth,ss}^*$	<p>Difference between the epithermal neutron flux if there was no boundary (<math>\Phi_{eth,ss}^*</math>) and the actual epithermal neutron flux at the atmosphere/subsurface interface (see equation B.9) [neutrons cm<sup>-2</sup> yr<sup>-1</sup>]</p> $(F\Delta\Phi)_{eth,ss}^* = \frac{\Delta\Phi_{eth,ss}^* D_{eth,a}/L_{eth,a} - \Delta\Phi_{eth,a}^{**} D_{eth,ss}/\Lambda_{f,e}}{D_{eth,a}/L_{eth,a} + D_{eth,ss}/L_{eth,ss}} \quad (E.11)$
$(F\Delta\Phi)_{eth,a}^*$	<p>Difference between <math>\Phi_{eth,a}^*</math> (the epithermal neutron flux in the atmosphere if there was no boundary) and <math>\Phi_{eth,a}</math> (the actual epithermal neutron flux at the atmosphere/subsurface interface) [neutrons cm<sup>-2</sup> yr<sup>-1</sup>]</p> $(F\Delta\Phi)_{eth,a}^* = \frac{\Delta\Phi_{eth,a}^* D_{eth,ss}/L_{eth,ss} - \Delta\Phi_{eth,a}^{**} D_{eth,ss}/\Lambda_{f,e}}{D_{eth,a}/L_{eth,a} + D_{eth,ss}/L_{eth,ss}} \quad (E.12)$
Continued on next page	

Table E.8 – continued from previous page

Term	Definition
$(\mathcal{F} \Delta \Phi)_{eth,ss}^*$	<p>Describes the difference between <math>\Phi_{eth,ss}^*</math> and the actual flux due to the shape of the epithermal neutron profile across the atmosphere/subsurface interface</p> $(\mathcal{F} \Delta \Phi)_{eth,ss}^* = \frac{p(E_{th})_a R_{th,ss} (F \Delta \Phi)_{eth,ss}^*}{\Lambda_{eth,ss} (\Sigma_{th,ss} - D_{th,ss}/L_{eth,ss}^2)} \quad (\text{E.13})$
$(\mathcal{F} \Delta \Phi)_{eth,a}^*$	<p>Describes the difference between <math>\Phi_{eth,a}^*</math> and the actual flux due to the shape of the epithermal neutron profile across the atmosphere/subsurface interface</p> $(\mathcal{F} \Delta \Phi)_{eth,a}^* = \frac{p(E_{th})_a R_{th,a} (F \Delta \Phi)_{eth,a}^*}{\Lambda_{eth,a} (\Sigma_{th,a} - D_{th,a}/L_{eth,a}^2)} \quad (\text{E.14})$
$f_{eth,m,ss}$	<p>Fraction of total epithermal neutrons absorbed per unit mass of rock that react to produce nuclide m; compositionally dependent [<i>unitless</i>]</p> $f_{eth,m,ss} = \frac{N_{k,ss} I_{a,k}}{I_{eff}} \quad (\text{E.15})$
$\Gamma_{eth,m,ss}$	Total rate of epithermal neutron absorption in subsurface [neutrons $\text{g}^{-1} \text{yr}^{-1}$ ]
$I_{a,k}$	Dilute resonance integral for absorption of epithermal neutrons by element k [ $10^{-24} \text{cm}^{-2}$ ]
$I_{eff,ss}$	<p>Effective/macroscopic resonance integral for absorption of epithermal neutrons in subsurface [<math>\text{cm}^{-2} \text{g}^{-1}</math>]</p> $I_{eff} = \sum_k I_{a,k} N_{k,bulk} \quad (\text{E.16})$
Continued on next page	



**Table E.8 – continued from previous page**

<b>Term</b>	<b>Definition</b>
$\Lambda_{eth,ss}$	Effective epithermal neutron attenuation length in subsurface, accounting for both absorption and moderation [g cm <sup>-2</sup> ] $\Lambda_{eth,ss} = [\xi(I_{eff,ss} + \Sigma_{sc,ss})]^{-1} = \Sigma_{eth,ss}^{-1} \quad (\text{E.17})$
$\Lambda_{eth,a}$	Effective epithermal neutron attenuation length in the atmosphere, accounting for both absorption and moderation [g cm <sup>-2</sup> ] $\Lambda_{eth,a} = [\xi(I_{eff,a} + \Sigma_{sc,a})]^{-1} = \Sigma_{eth,a}^{-1} \quad (\text{E.18})$
$L_{eth,ss}$	Diffusion length for epithermal neutrons in the subsurface [g cm <sup>-2</sup> ] $L_{eth,ss} = (\sqrt{3\Sigma_{sc,ss}\Sigma_{eth,ss}})^{-1} \quad (\text{E.19})$
$L_{eth,a}$	Diffusion length for epithermal neutrons in the air [g cm <sup>-2</sup> ] $L_{eth,a} = (\sqrt{3\Sigma_{sc,a}\Sigma_{eth,a}})^{-1} \quad (\text{E.20})$
$N_{k,ss,bulk/target}$	Atomic concentration of element k in subsurface (target or bulk specified as additional subscript) [at/g]
$N_{k,a}$	Atomic concentration of element k in air [at/g]
$P_{eth,m}$	Production rate for epithermal production of nuclide m. See eqn B.28.
$\Phi_{eth,ss}(z)$	Epithermal neutron flux in subsurface [neutrons cm <sup>-2</sup> yr <sup>-1</sup> ]
Continued on next page	

Table E.8 – continued from previous page

Term	Definition
$\Phi_{eth,ss}^*$	<p>Epithermal neutron flux that would be observed at the land surface if the properties of the medium did not change (e.g. identical to the subsurface.) [neutrons <math>\text{cm}^{-2} \text{yr}^{-1}</math>] (See equation B.6)</p> $\Phi_{eth,ss}^* = P_f(0) \frac{R_{eth,ss}}{\Sigma_{eth,ss} - \frac{D_{eth,ss}}{\Lambda_{f,e}^2}} \quad (\text{E.21})$
$\Phi_{eth,a}^*$	<p>Epithermal neutron flux that would be observed at the land surface if the properties of the medium did not change (e.g. atmosphere identical to the air.) [neutrons <math>\text{cm}^{-2} \text{yr}^{-1}</math>]</p> $\Phi_{eth,a}^* = P_f(0) \frac{R_{eth,a}}{\Sigma_{eth,a} - \frac{D_{eth,a}}{\Lambda_{f,e}^2}} \quad (\text{E.22})$
$P_f(Z)$	<p>Production rate of epithermal neutrons from fast secondary cosmogenic neutrons as a function of depth. [neutrons <math>(\text{g air})^{-1}\text{yr}^{-1}</math>]</p>
$P_f(0)$	<p>is <math>P_f</math> at depth equal to 0 and is a calibrated production rate parameter. [neutrons <math>(\text{g air})^{-1}\text{yr}^{-1}</math>]</p>
$p(E_{th})_{ss}$	<p>Resonance escape probability in the subsurface - probability that a neutron will pass through the epithermal energy range to the thermal range without being absorbed [unitless]</p> $p(E_{th}) = \exp\left[-\frac{I_{eff}}{\sum_k \xi_k N_{k,bulk} \sigma_{sc,k}}\right] \quad (\text{E.23})$
Continued on next page	

Table E.8 – continued from previous page

Term	Definition
$p(E_{th})_a$	Resonance escape probability in the air - probability that a neutron will pass through the epithermal energy range to the thermal range without being absorbed [unitless]. Value according to Phillips & Plummer (1996). $p(E_{th})_a = 0.56 \quad (\text{E.24})$
$R_{eth,ss}$	Ratio of epithermal neutron production in the rock to that of the atmosphere [unitless] $R_{eth,ss} = \sqrt{\frac{\bar{A}_{ss}}{A_a}} \quad (\text{E.25})$
$R_{eth,a}$	Ratio of epithermal neutron production in the atmosphere to that of the atmosphere [unitless]. $R_{eth,a} = \sqrt{\frac{\bar{A}_a}{A_a}} = 1 \quad (\text{E.26})$
$\Sigma_{eth,ss}$	Effective epithermal loss cross-section in subsurface, by both absorption and energy moderation [ $\text{cm}^2 \text{g}^{-1}$ ]
$\Sigma_{eth,a}$	Effective epithermal loss cross-section in air, by both absorption and energy moderation [ $\text{cm}^2 \text{g}^{-1}$ ]
$\Sigma_{sc,ss}$	Macroscopic neutron scattering cross-section in subsurface [ $\text{cm}^2 \text{g}^{-1}$ ] $\Sigma_{sc,ss} = \sum_k N_{k,bulk} \sigma_{sc,k} \quad (\text{E.27})$
$\Sigma_{sc,a}$	Macroscopic neutron scattering cross-section in air. Constant = 0.3773 [ $\text{cm}^2 \text{g}^{-1}$ ]

Continued on next page

Table E.8 – continued from previous page

Term	Definition
$\sigma_{sc,k}$	Neutron scattering cross-section for element k [ $1 \times 10^{-24}$ cm <sup>2</sup> ]
$\xi_{bulk}$	Macroscopic average log decrement neutron energy loss per collision for the bulk rock  $\bar{\xi}_{bulk} = \frac{\sum_k \xi_k \sigma_{sc,k} N_{k,ss,bulk}}{\sum_k \sigma_{sc,k} N_{k,ss,bulk}} \quad (\text{E.28})$
$\xi_k$	Average log decrement of energy loss for element k
<i>Thermal Production</i>	
$D_{th,ss}$	Diffusion coefficient for thermal neutrons in the subsurface [ <i>unitless</i> ]  $D_{th,ss} = [3\Sigma_{sc,ss}(1 - \frac{2}{3A_s})]^{-1} \quad (\text{E.29})$
$D_{th,a}$	Diffusion coefficient for thermal neutrons in the atmosphere [ <i>unitless</i> ]  $D_{th,a} = [3\Sigma_{sc,a}(1 - \frac{2}{3A_a})]^{-1} \quad (\text{E.30})$
$\Delta\Phi_{th,ss}^*$	Describes the difference between the hypothetical equilibrium thermal neutron flux in the air and the subsurface [neutrons cm <sup>-2</sup> yr <sup>-1</sup> ]  $\Delta\Phi_{th,ss}^* = \Phi_{th,a}^* - \Phi_{th,ss}^* \quad (\text{E.31})$
Continued on next page	

Table E.8 – continued from previous page

Term	Definition
$f_{th,ss,m}$	Fraction of thermal neutrons absorbed per unit mass by target k that react to form cosmogenic nuclide m [unitless] $f_{th,ss,m} = \frac{\sigma_{th,k} N_{k,ss,target}}{\Sigma_{th,ss}} \quad (\text{E.32})$
$(\mathcal{F} \Delta \Phi)_{th,ss}^*$	Describes the difference between $\Phi_{th,ss}^*$ and the actual flux due to the shape of the thermal neutron flux profile across the interface. See equation B.16
$\Lambda_{th,ss}$	Effective thermal neutron attenuation length for medium i [g cm <sup>-2</sup> ] $\Lambda_{th,ss} = \sum_{th,ss}^{-1} \quad (\text{E.33})$
$L_{th,ss}$	Diffusion length for thermal neutrons in the subsurface [g cm <sup>-2</sup> ] $L_{th,ss} = \sqrt{\frac{D_{th,ss}}{\Sigma_{th,ss}}} \quad (\text{E.34})$
$P_{th,ss,m}$	production rate of nuclide m by thermal neutrons [atoms g <sup>-1</sup> yr <sup>-1</sup> ]
$L_{th,a}$	Diffusion length for thermal neutrons in the air [g cm <sup>-2</sup> ] $L_{th,a} = \sqrt{\frac{D_{th,a}}{\Sigma_{th,a}}} \quad (\text{E.35})$
$\Phi_{th,ss}(Z)$	Thermal neutron flux at depth Z [neutrons cm <sup>-2</sup> yr <sup>-1</sup> ]
Continued on next page	

Table E.8 – continued from previous page

Term	Definition
$\Phi_{th,ss}^*$	<p>Thermal neutron flux that would be observed at the land surface if the properties of the atmosphere and subsurface were identical [neutrons <math>\text{cm}^{-2} \text{yr}^{-1}</math>]</p> $\Phi_{th,ss}^* = \frac{p(E_{th})_a R_{th,ss} \Phi_{eth,ss}^*}{\Lambda_{eth,ss} (\Sigma_{th,ss} - \frac{D_{th,ss}}{\Lambda_{eth,ss}^2})} \quad (\text{E.36})$
$\Phi_{th,a}^*$	<p>Thermal neutron flux that would be observed at the land surface if the properties of the medium did not change and were identical to the atmosphere [neutrons <math>\text{cm}^{-2} \text{yr}^{-1}</math>]</p> $\Phi_{th,a}^* = \frac{p(E_{th})_a R_{th,a} \Phi_{eth,a}^*}{\Lambda_{eth,a} (\Sigma_{th,a} - \frac{D_{th,a}}{\Lambda_{eth,a}^2})} \quad (\text{E.37})$
$R_{th,ss}$	<p>Ratio of thermal neutron production in the rock to that in the atmosphere [unitless]</p> $R_{th,ss} = \frac{p(E_{th,ss})}{p(E_{th,a})} \quad (\text{E.38})$
$\sigma_{th,ss,k}$	Elemental thermal neutron cross-section for the subsurface [barns] 1 barn = $10^{-24} \text{cm}^2$
$\sigma_{th,a,k}$	Elemental thermal neutron cross-section for the air [barns] 1 barn = $10^{-24} \text{cm}^2$
$\Sigma_{th,ss}$	<p>Macroscopic neutron absorption cross section [<math>\text{cm}^2 \text{g}^{-1}</math>]</p> $\Sigma_{th,ss} = \sum_k \sigma_{th,k} N_{k,ss,bulk} = \Lambda_{th,ss}^{-1} \quad (\text{E.39})$
$\Gamma_{th,ss,m}$	Total rate of thermal neutron absorption [neutrons $\text{g}^{-1} \text{yr}^{-1}$ ]

*Muons*

Continued on next page

Table E.8 – continued from previous page

Term	Definition
$f_i^*$	Probability for particle emission to the radionuclide. See Heisinger et al. (2002a).
$f_{i,D}$	Fraction of muons stopped by element k and absorbed by the nucleus before decay of the muon (Fabryka-Martin, 1988) [ <i>unitless</i> ]
$f_{i,C}$	Chemical compound factor [ <i>unitless</i> ] Chemical compound factor (for Be, Al, C, see Heisinger et al. (2002a)); values computed on a sample by sample basis for $^{36}\text{Cl}$ due to variations in composition using values from von Egidy & Hartmann (1982). $f_{i,C} = \frac{M_{k,bulk}\Omega_k}{\sum_j M_{j,bulk}\Omega_j} \quad (\text{E.40})$
$N_{atoms}$	Atom number density of the target atom [atoms $\text{g}^{-1}$ ]
$\Omega$	Atomic number of the element. Subscript k refers to the target element and j refers to all elements in the rock.
P	Average probability of muon capture by a nucleus relative to that of oxygen (von Egidy & Hartmann, 1982) [ <i>unitless</i> ]
$P_{\mu-,m}$	Production rate for negative muon production of nuclide m. See eqns B.3 and B.32.
$P_{\mu,fast,m}$	Production rate for fast muon production of nuclide m. See eqn B.24.
$P_{n,\mu}$	Production rate for muon-induced neutrons. See eqn B.29.
$P_{n,\mu}(Z)$	Total muon-induced neutron production at depth Z [neutrons $\text{cm}^{-2} \text{yr}^{-1}$ ]; value at surface is $P_{n,\mu}(0)$ $P_{n,\mu}(Z) = Y_s\Psi_\mu(Z) + 5.8 \times 10^{-6}\Phi_{\mu f}(Z) \quad (\text{E.41})$

Continued on next page

**Table E.8 – continued from previous page**

<b>Term</b>	<b>Definition</b>
$\Phi_{\nu,0}$	Vertical muon flux at SLHL as a function of depth. Only valid for depths of $<200,000 \text{ g/cm}^2$ . See equation B.17. [ $\text{cm}^{-2}\text{s}^{-1}\text{sr}^{-1}$ ]
$\phi_{\mu f}(Z, \theta)$	Fast muon flux at depth Z [muons $\text{g}^{-1}\text{yr}^{-1}$ ]; calculated from the muon code
$\Psi_{\mu-}(Z)$	Slow negative muon stopping rate at depth Z [muons $\text{g}^{-1}\text{yr}^{-1}$ ]; calculated from the muon code
$R_{\mu-}(h)$	Rate of negative muons stopping at an atmospheric depth of h
$R_{\mu}(Z)$	Ratio of muon production to epithermal neutron production [ <i>unitless</i> ]
	$R_{\mu}(Z) = \frac{S_{el,\mu}P_{n,\mu}(Z)}{S_{el}P_f(0)R_{eth}} \quad (\text{E.42})$
$R'_{\mu}$	Ratio of the muon production rate to the production rate for thermal neutrons. [ <i>unitless</i> ] See eqn B.33.
	$R'_{\mu} = \frac{p(E_{th})_a}{p(E_{th})} R_{\mu} \quad (\text{E.43})$
$\sigma_{190}$	Cross-section for fast muon production at 190 GeV [ $\text{mb}$ ]. Note: 1 barn= $1 \times 10^{-24} \text{ cm}^2$
$Y_s$	Average neutron yield per stopped negative muon [neutrons/(stopped negative muon)]
	$Y_s = \sum_k f_{c,k,bulk} f_{d,k} Y_{n,k} \quad (\text{E.44})$
$Y_{n,k}$	Average neutron yield per captured muon for element k - (Fabryka-Martin, 1988)
<i>Radiogenic Production</i>	
$F_{k,bulk}$	Fractional abundance of element k in ppm in the bulk rock
Continued on next page	



Table E.8 – continued from previous page

Term	Definition
$P_r$	Total radiogenic production from all mechanisms in a particular sample. (equation B.37)
$P_{n,\alpha}$	Production rate of neutrons from alpha particles in neutrons/g/yr
$P_{n,sf}$	Neutron production rate due to the spontaneous fission of $^{238}\text{U}$
$S_k$	Mass stopping power of element k for $\alpha$ -particles of a given energy
X	Neutron production factors related to the light isotope composition of the rock matrix. See equation B.40.
Y	Neutron production factors related to the light isotope composition of the rock matrix. See equation B.41.
$Y_n^U$	Neutron yields of element i per ppm U in equilibrium
$Y_n^{Th}$	Neutron yields of element i per ppm Th in equilibrium
<i>Accumulation</i>	
$D$	Depth of the sample with ‘old’ representing the original sample depth and ‘new’ is the updated sample depth, accounting for erosion during the time period
$\Delta t$	Time step in the CRONUScalc program.
$\epsilon$	Erosion rate [g/cm <sup>2</sup> ]
$f_{decay}$	Decay factor that accounts for the fact that some of the nuclides produced at the beginning of the time period will have decayed by the end of the period. (equation 8)
$\lambda$	Decay constant for the nuclide
$N_{tot}$	Total inventory in the sample up to the current time step
$N_{prev}$	Inventory from all previous time steps.
$P_{tot}$	Instantaneous production rate of the nuclide from all mechanisms and is the sum of production from all other mechanisms.

1799 **References**

- 1800 Amidon, W. H., & Farley, K. A. (2010). Mass spectrometric He-3 measure-  
1801 ment in He-4-rich phases: Techniques and limitations for cosmogenic He-3  
1802 dating of zircon, apatite, and titanite. *Geochemistry Geophysics Geosys-*  
1803 *tems*, 11.
- 1804 Amidon, W. H., & Farley, K. A. (2012). Cosmogenic He-3 and Ne-21 dating  
1805 of biotite and hornblende. *Earth and Planetary Science Letters*, 313, 86–  
1806 94.
- 1807 Amidon, W. H., Farley, K. A., Burbank, D. W., & Pratt-Sitaula, B. (2008).  
1808 Anomalous cosmogenic (3)He production and elevation scaling in the high  
1809 Himalaya. *Earth and Planetary Science Letters*, 265, 287–301.
- 1810 Amidon, W. H., Rood, D. H., & Farley, K. A. (2009). Cosmogenic He-3 and  
1811 Ne-21 production rates calibrated against Be-10 in minerals from the Coso  
1812 volcanic field. *Earth and Planetary Science Letters*, 280, 194–204.
- 1813 Argento, D. C., Stone, J. O., Reedy, R. C., & O'Brien, K. (2014).  
1814 Physics-based modeling of cosmogenic nuclides part II – Key aspects of  
1815 in-situ cosmogenic nuclide production. *Quaternary Geochronology*, (p.  
1816 doi:10.1016/j.quageo.2014.09.005).
- 1817 Aumer, R. A. (2010). *Calibration of low energy production of <sup>36</sup>Cl and the*  
1818 *creation of an exposure age calculator*. M.S. Thesis New Mexico Tech.
- 1819 Balco, G., Stone, J. O., Lifton, N., & Dunai, T. J. (2008). A complete and  
1820 easily accessible means of calculating surface exposure ages or erosion rates  
1821 from <sup>10</sup>Be and <sup>26</sup>Al measurements. *Quaternary Geochronology*, 3, 174–195.
- 1822 Bevington, P. R., & Robinson, D. K. (1992). *Data Reduction and Error*  
1823 *Analysis for the Physical Sciences*. (2nd ed.). McGraw-Hill, Inc.
- 1824 Bierman, P. R. (1994). Using in situ produced cosmogenic isotopes to esti-  
1825 mate rates of landscape evolution: A review from the geomorphic perspec-  
1826 tive. *Journal of Geophysical Research*, 99, 13885–13896.
- 1827 Blard, P.-H., Balco, G., Burnard, P., Farley, K., Fenton, C., Friedrich, R.,  
1828 Jull, A., Niedermann, S., Pik, R., Schaefer, J. M., Scott, E., Shuster,  
1829 D., Stuart, F., Tibari, B., Winckler, G., & Zimmermann, L. (2014). An

- 1830 inter-laboratory comparison of cosmogenic  $^3\text{He}$  and  $^4\text{He}$  in the CRONUS-  
1831 P pyroxene standard. *Quaternary Geochronology, CRONUS-Earth Special*  
1832 *Volume*, doi:10.1016/j.quageo.2014.08.004.
- 1833 Blard, P.-H., & Farley, K. (2008). The influence of radiogenic  $^4\text{He}$  on cos-  
1834 mogenic  $^3\text{He}$  determinations in volcanic olivine and pyroxene. *Earth and*  
1835 *Planetary Science Letters*, 276, 20–29.
- 1836 Blard, P.-H., & Pik, R. (2008). An alternative isochron method for measuring  
1837 cosmogenic  $^3\text{He}$  in lava flows. *Chemical Geology*, 251, 20–32.
- 1838 Borchers, B., Marrero, S. M., Balco, G., Caffee, M., Goehring, B., Gosse,  
1839 J., Lifton, N., Nishiizumi, K., Phillips, F. M., Schaefer, J., & Stone,  
1840 J. O. (2015). Geological calibration of spallation production rates in the  
1841 CRONUS-Earth project. *Quaternary Geochronology, CRONUS-Earth spe-*  
1842 *cial volume*, doi:10.1016/j.quageo.2015.01.009.
- 1843 Braucher, R., Bourles, D., Merchel, S., Vidani Romani, J., Fernandez-  
1844 Mosquera, D., Marti, K., Leanni, L., Chauvet, F., Arnold, M., Aumaitre,  
1845 G., & Keddadouche, K. (2013). Determination of muon attenuation lengths  
1846 in depth profiles from in situ produced cosmogenic nuclides. *Nuclear In-*  
1847 *struments & Methods in Physics Research Section B - Beam Interactions*  
1848 *with Materials and Atoms*, 294, 484–490.
- 1849 Braucher, R., Brown, E. T., Bourles, D., & Colin, F. (2003). In situ produced  
1850  $^{10}\text{Be}$  measurements at great depths: implications for production rates by  
1851 fast muons. *Earth and Planetary Science Letters*, 211, 251–258.
- 1852 Braucher, R., Del Castillo, P., Siame, L., Hidy, A. J., & Bourles, D. L. (2009).  
1853 Determination of both exposure time and denudation rate from an in situ-  
1854 produced  $^{10}\text{Be}$  depth profile: A mathematical proof of uniqueness. model  
1855 sensitivity and applications to natural cases:. *Quaternary Geochronology*,  
1856 4, 56–57.
- 1857 Braucher, R., Merchel, S., Borgomano, J., & Bourles, D. L. (2011). Pro-  
1858 duction of cosmogenic nuclides at great depth: A multi element approach.  
1859 *Earth and Planetary Science Letters*, 309, 1–9.
- 1860 Cerling, T. E. (1990). Dating Geomorphic Surfaces Using Cosmogenic  $^3\text{He}$ .  
1861 *Quaternary Research*, 33, 148–156.

- 1862 Charalambus, S. (1971). Nuclear transmutation by negative stopped muons  
1863 and the activity induced by the Cosmic-Ray muons. *Nuclear Physics*,  
1864 *A166*, 145–161.
- 1865 Chmeleff, J., von Blankenburg, F., Kossert, K., & Jakob, D. (2010). Determi-  
1866 nation of the  $^{10}\text{Be}$  half-life by multicollector ICP-MS and liquid scintillation  
1867 counting. *Nuclear Instruments and Methods in Physics Research Section*  
1868 *B - Beam Interactions with Materials and Atoms*, *268*, 192–199.
- 1869 Dep, L., Elmore, D., Lipshutz, M., Vogt, S., Phillips, F., & Zreda, M. G.  
1870 (1994). Depth dependence of cosmogenic neutron-captured-produced  $^{36}\text{Cl}$   
1871 in a terrestrial rock. *Nuclear Instruments and Methods in Physics Research*  
1872 *B*, *92*, 301–307.
- 1873 Desilets, D., & Zreda, M. G. (2003). Spatial and temporal distribution of  
1874 secondary cosmic-ray nucleon intensities and applications to in situ cos-  
1875 mogenic dating. *Earth and Planetary Science Letters*, *206*, 21–42.
- 1876 Desilets, D., Zreda, M. G., Almasi, P. F., & Elmore, D. (2006a). Determina-  
1877 tion of cosmogenic  $^{36}\text{Cl}$  in rocks by isotope dilution: innovations, validation  
1878 and error propagation. *Chemical Geology*, *233*, 185–195.
- 1879 Desilets, D., Zreda, M. G., & Prabu, T. (2006b). Extended scaling factors  
1880 for in situ cosmogenic nuclides: New measurements at low latitude. *Earth*  
1881 *and Planetary Science Letters*, *246*, 265–276.
- 1882 Dorman, L. I., Valdes-Galicia, J. F., & Dorman, I. V. (1999). Numerical  
1883 simulation and analytical description of solar neutron transport in the  
1884 Earth’s atmosphere. *Journal of Geophysical Research*, *104*, 22417–22426.
- 1885 Dunai, T. (2001a). Influence of secular variation of the geomagnetic field  
1886 on production rates of in situ produced cosmogenic nuclides. *Earth and*  
1887 *Planetary Science Letters*, *193*, 197–212.
- 1888 Dunai, T., Binnie, S. A., Hein, A. S., & Paling, S. M. (2014). The effects of a  
1889 hydrogen-rich ground cover on cosmogenic thermal neutrons: Implications  
1890 for exposure dating. *Quaternary Geochronology*, *22*, 183–191.
- 1891 Dunai, T. J. (2000). Scaling factors for production rates of in situ produced  
1892 cosmogenic nuclides: a critical reevaluation. *Earth and Planetary Science*  
1893 *Letters*, *176*, 157–169.

- 1894 Dunai, T. J. (2001b). Reply to comment on 'Scaling factors for production  
1895 rates of in situ produced cosmogenic nuclides: a critical reevaluation' by  
1896 Darin Desilets, Marek Zreda, and Nathaniel Lifton. *Earth and Planetary  
1897 Science Letters*, 188, 289–298.
- 1898 Dunai, T. J. (2010). *Cosmogenic Nuclides: Principles, Concepts and Appli-  
1899 cations in the Earth Surface Sciences*. Cambridge University Press.
- 1900 Dunai, T. J., Stuart, F. M., Pik, R. I., Burnard, P., & Gayer, E. (2007).  
1901 Production of  $^3\text{He}$  in crustal rocks by cosmogenic thermal neutrons. *Earth  
1902 and Planetary Science Letters*, 258, 228–236.
- 1903 Dunne, J., Elmore, D., & Muzikar, P. (1999). Scaling factors for the rates of  
1904 production of cosmogenic nuclides for geometric shielding and attenuation  
1905 at depth on sloped surfaces. *Geomorphology*, 27, 3–11.
- 1906 von Egidy, T., & Hartmann, F. J. (1982). Average muonic coulomb capture  
1907 probabilities for 65 elements. *Physical Review A*, 26, 2355–2360.
- 1908 Eidelman, S. (2004). Review of Particle Physics\*1. *Physics Letters B*, 592,  
1909 1–5.
- 1910 Evans, J. M. (2001). *Calibration of the production rates of cosmogenic  $^{36}\text{Cl}$   
1911 from potassium*. Ph.D. thesis The Australian National University, Can-  
1912 berra. Doctorate of Philosophy.
- 1913 Fabryka-Martin, J. (1988). *Production of radionuclides in the earth and  
1914 their hydrogeologic significance, with emphasis on chlorine-36 and iodine-  
1915 129*. Ph.D. thesis University of Arizona, Hydrology and Water Resources,  
1916 Tucson. Doctor of Philosophy with a major in Hydrology.
- 1917 Farber, D. L., Mériaux, A.-S., & Finkel, R. C. (2008). Attenuation length  
1918 for fast nucleon production of  $^{10}\text{Be}$  derived from near-surface production  
1919 profiles. *Earth and Planetary Science Letters*, 274, 295–300.
- 1920 Farley, K. A., Libarkin, J., Mukhopadhyay, S., & Amidon, W. (2006). Cos-  
1921 mogenic and nucleogenic He-3 in apatite, titanite, and zircon. *Earth and  
1922 Planetary Science Letters*, 248, 451–461.
- 1923 Feige, Y., Oltman, B. G., & Kastner, J. (1968). Production Rates of Neutrons  
1924 in Soils Due to Natural Radioactivity. *Journal of Geophysical Research*,  
1925 73, 3135–3142.

- 1926 Friedlander, G., Kennedy, J. W., Macias, E. S., & Miller, J. M. (1981).  
1927 *Nuclear and Radiochemistry*. (2nd ed.). John Wiley & Sons, Inc.
- 1928 Gaisser, T. K. (1990). *Cosmic Rays and Particle Physics*. Cambridge: Cam-  
1929 bridge University Press.
- 1930 Goehring, B. M., Kelly, M. A., Schaefer, J. M., Finkel, R., & Lowell, T. V.  
1931 (2010a). Dating of raised marine and lacustrine deposits in east Green-  
1932 land using beryllium-10 depth profiles and implications for estimates of  
1933 subglacial erosion. *Journal of Quaternary Science*, *26*, 865–874.
- 1934 Goehring, B. M., Kurz, M. D., Balco, G., Schaefer, J. M., Licciardi, J., &  
1935 Lifton, N. (2010b). A reevaluation of in situ cosmogenic  $^3\text{He}$  production  
1936 rates. *Quaternary Geochronology*, *5*, 410–418.
- 1937 Goehring, B. M., Schimmelpfennig, I., & Schaefer, J. M. (2014). Capabilities  
1938 of the lamont-doherty earth observatory in situ  $^{14}\text{C}$  extraction laboratory  
1939 updated. *Quaternary Geochronology*, *19*, 194–197.
- 1940 Goldhagen, P., Reginatto, M., Kniss, T., Wilson, J. W., Singleterry, R. C.,  
1941 Jones, I. W., & Steveninck, W. V. (2002). Measurement of the energy  
1942 spectrum of cosmic-ray induced neutrons aboard an ER-2 high-altitude  
1943 airplane. *Nuclear Instruments and Methods in Physics Research A*, *476*,  
1944 42–51.
- 1945 Gosse, J. C., & Phillips, F. M. (2001). Terrestrial in situ cosmogenic nuclides:  
1946 theory and application. *Quaternary Science Reviews*, *20*, 1475–1560.
- 1947 Granger, D., & Muzikar, P. (2001). Dating sediment burial with in situ-  
1948 produced cosmogenic nuclides: theory, techniques, and limitations. *Earth  
1949 and Planetary Science Letters*, *188*, 269–281.
- 1950 Granger, D. E. (2006). A review of burial dating methods using  $^{26}\text{Al}$  and  
1951  $^{10}\text{Be}$ . In L. Siame, D. L. Bourles, & E. T. Brown (Eds.), *In situ-produced  
1952 cosmogenic nuclides and quantification of geological processes* (pp. 1–16).  
1953 volume 415 of *Geological Society of America Special Papers*.
- 1954 Granger, D. E., & Smith, A. L. (2000). Dating buried sediments using ra-  
1955 dioactive decay and muogenic production of Al-26 and Be-10. *Nuclear  
1956 Instruments & Methods in Physics Research*, *B126*, 822–826.

- 1957 Groom, D., Mokhov, N., & Striganov, S. (2001). Muon stopping power and  
1958 range tables 10 MeV-100 TeV. *Atomic Data and Nuclear Data Tables*, *78*,  
1959 183–356.
- 1960 Handwerger, D. A., Cerling, T. E., & Bruhn, R. L. (1999). Cosmogenic  $^{14}\text{C}$   
1961 in carbonate rocks. *Geomorphology*, *27*, 13–24.
- 1962 Hein, A. S., Hulton, N. R., Dunai, T. J., Schnabel, C., Kaplan, M. R.,  
1963 Naylor, M., & Xu, S. (2009). Middle Pleistocene glaciation in Patagonia  
1964 dated by cosmogenic-nuclide measurements on outwash gravels. *Earth*,  
1965 *286*, 184–197.
- 1966 Heisinger, B., Lal, D., Jull, A. J. T., Kubik, P., Ivy-Ochs, S., Knie, K.,  
1967 & Nolte, E. (2002a). Production of selected cosmogenic radionuclides by  
1968 muons: 2. Capture of negative muons. *Earth and Planetary Science Let-*  
1969 *ters*, *200*, 357–369.
- 1970 Heisinger, B., Lal, D., Jull, A. J. T., Kubik, P., Ivy-Ochs, S., Neumaier,  
1971 S., Knie, K., Lazarev, V., & Nolte, E. (2002b). Production of selected  
1972 cosmogenic radionuclides by muons: 1. Fast muons. *Earth and Planetary*  
1973 *Science Letters*, *200*, 345–355.
- 1974 Hidy, A. J., Gosse, J. C., Pederson, J. L., Mattern, J. P., & Finkel,  
1975 R. C. (2010). A geologically constrained Monte Carlo approach to mod-  
1976 eling exposure ages from profiles of cosmogenic nuclides: An example  
1977 from Lees Ferry, Arizona. *Geochemistry Geophysics Geosystems*, *11*, doi:  
1978 10.1029/2010GC003084.
- 1979 Hillas, A. M. (1972). *Cosmic Rays*. Oxford: Pergamon Press.
- 1980 Jull, A., Scott, E., & Bierman, P. (2013). The CRONUS-Earth inter-  
1981 comparison for cosmogenic isotope analysis. *Quaternary Geochronology*,  
1982 *CRONUS-Earth Special Volume*, doi:10.1016/j.quageo.2013.09.003.
- 1983 Jull, A., Scott, E., & Marrero, S. (2011). The CRONUS-Earth inter-  
1984 comparison for cosmogenic isotope analysis. In *The Twelfth International*  
1985 *Conference on Accelerator Mass Spectrometry* (p. 242).
- 1986 Kim, K. J., & Englert, P. A. J. (2004). Profiles of in situ  $^{10}\text{Be}$  and  $^{26}\text{Al}$   
1987 at great depths at the Macraes Flat, East Otago. *Earth and Planetary*  
1988 *Science Letters*, *223*, 113–126.

- 1989 Kim, K. J., Lal, D., Englert, P. A. J., & Southon, J. (2007). In situ  $^{14}\text{C}$  depth  
1990 profile of subsurface vein quartz samples from Macraes Flat New Zealand.  
1991 *Nuclear Instruments and Methods in Physics Research Section B - Beam*  
1992 *Interactions with Materials and Atoms*, 259, 632–636.
- 1993 Korschinek, G., Bergmaier, A., Faestermann, T., Gerstmann, U. C., Knie, K.,  
1994 Rugel, G., Wallner, A., Dillmann, I., Dollinger, G., Lierse von Gostomski,  
1995 C., Kossert, K., Maiti, M., Poutivtsec, M., & Remmert, A. (2010). A  
1996 new value for the half-life of  $^{10}\text{Be}$  by heavy-ion elastic recoil detection and  
1997 liquid scintillation counting. *Nuclear Instruments and Methods in Physics*  
1998 *Research Section B - Beam Interactions with Materials and Atoms*, B268,  
1999 187–191.
- 2000 Korte, M., & Constable, C. G. (2005). Continuous geomagnetic field models  
2001 for the past 7 millennia: 2. CALS7K. *Geochemistry, Geophysics, Geosys-*  
2002 *tems*, 6, Q02H16.
- 2003 Kurz, M. D. (1986). Cosmogenic helium in a terrestrial igneous rock. *Nature*,  
2004 320, 435–439.
- 2005 Laj, C., Kissel, C., Beer, J., Channell, J., Kent, D., Lowrie, W., & Meert, J.  
2006 (2004). High resolution global paleointensity stack since 75 kyr (GLOPIS-  
2007 75) calibrated to absolute values. *Timescales of the Geomagnetic Field*,  
2008 (pp. 255–265).
- 2009 Lal, D. (1958). *Investigations of Nuclear Interactions Produced by Cosmic*  
2010 *Rays*. Phd Bombay University.
- 2011 Lal, D. (1987). Production of  $^3\text{He}$  in terrestrial rocks. *Chemical Geology*, 66,  
2012 89–98.
- 2013 Lal, D. (1988). In Situ-Produced Cosmogenic Isotopes in Terrestrial Rocks.  
2014 *Ann. Rev. Earth Planet. Sci.*, 16, 355–388.
- 2015 Lal, D. (1991). Cosmic ray labeling of erosion surfaces: In situ nuclide  
2016 production rates and erosion models. *Earth and Planetary Science Letters*,  
2017 104, 424–439.
- 2018 Lal, D., & Peters, B. (1967). Cosmic ray produced radioactivity on the earth.  
2019 In K. Sitte (Ed.), *Hanbuch der Physik* (pp. 551–612). Berlin: Springer.



- 2020 Lifton, N., Sato, T., & Dunai, T. J. (2014). Scaling in situ cosmogenic  
2021 nuclide production rates using analytical approximations to atmospheric  
2022 cosmic-ray fluxes. *Earth and Planetary Science Letters*, *386*, 149–160.
- 2023 Lifton, N., Smart, D. F., & Shea, M. A. (2008). Scaling time-integrated in  
2024 situ cosmogenic nuclide production rates using a continuous geomagnetic  
2025 model. *Earth and Planetary Science Letters*, *268*, 190–201.
- 2026 Lifton, N. A., Bieber, J. W., Clem, J. M., Duldig, M. L., Evenson, P., Hum-  
2027 ble, J. E., & Pyle, R. (2005). Addressing solar modulation and long-term  
2028 uncertainties in scaling in situ cosmogenic nuclide production rates. *Earth  
2029 and Planetary Science Letters*, *239*, 140–161.
- 2030 Lifton, N. A., Jull, A. J. T., & Quade, J. (2001). A new extraction tech-  
2031 nique and production rate estimate for in situ cosmogenic  $^{14}\text{C}$  in quartz.  
2032 *Geochimica et Cosmochimica Acta*, *65*, 1953–1969.
- 2033 Lupker, M., Hippe, K., Kober, F., Wacker, L., Braucher, R., Bourles, D. L.,  
2034 Vidal Romani, J., & Weiler, R. (2013). Depth-dependence of the pro-  
2035 duction rate of in-situ  $^{14}\text{C}$  in quartz. *American Geophysical Union Fall  
2036 Meeting, Poster EP13C-0849*.
- 2037 Lupker, M., Hippe, K., Wacker, L., Kober, F., Maden, C., Braucher, R.,  
2038 Bourles, D., Vidal Romani, J., & Wieler, R. (2015). Depth-dependence of  
2039 the production rate of in-situ  $^{14}\text{C}$  in quartz from the Leymon High core,  
2040 Spain. *Quaternary Geochronology*, *28*, 80–87.
- 2041 Marrero, S., Phillips, F., Caffee, M., & Gosse, J. (2015). CRONUS-Earth  
2042 cosmogenic  $^{36}\text{Cl}$  calibration. *Quaternary Geochronology, CRONUS-Earth  
2043 Special Volume*, submitted.
- 2044 Marrero, S. M. (2012). *Calibration of Cosmogenic Chlorine-36*. Doctorate  
2045 New Mexico Tech, Dept of Earth & Environmental Science.
- 2046 Marrero, S. M., Phillips, F. M., Caffee, M., Stone, J. O., Swanson, T., &  
2047 Hinz, M. (this volume, submitted). Resampling of puget lowlands yields  
2048 lower discrepancy in cosmogenic chlorine-36 production rates. *Quaternary  
2049 Geochronology, CRONUS Special Volume*.
- 2050 Masarik, J., Kollar, D., & Vanya, S. (2000). Numerical simulation of in  
2051 situ production of cosmogenic nuclides: Effects of irradiation geometry.

- 2052 *Nuclear Instruments and Methods in Physics Research Section B: Beam*  
2053 *Interactions with Materials and Atoms*, 172, 786–789.
- 2054 Mughabghab, S. (2006). *Atlas of Neutron Resonances: Resonance parameters*  
2055 *and thermal cross-sections Z=1-100*. Elsevier Science Ltd.
- 2056 Nishiizumi, K., Imamura, M., Caffee, M. W., Southon, J. R., Finkel, R. C.,  
2057 & McAninch, J. (2007). Absolute calibration of  $^{10}\text{Be}$  AMS standards.  
2058 *Nuclear Instruments and Methods in Physics Research Section B - Beam*  
2059 *Interactions with Materials and Atoms*, 258, 403–413.
- 2060 Nishiizumi, K., Winterer, E. L., Kohl, C. P., Klein, J., Middleton, R., Lal,  
2061 D., & Arnold, J. R. (1989). Cosmic ray production rates of  $^{10}\text{Be}$  and  $^{26}\text{Al}$   
2062 in quartz from glacially polished rocks. *Journal of Geophysical Research*,  
2063 94, 9.
- 2064 Phillips, F., Stone, W. D., & Fabryka-Martin, J. (2001). An improved  
2065 approach to calculating low-energy cosmic-ray neutron fluxes near the  
2066 land/atmosphere interface. *Chemical Geology*, 175, 689–701.
- 2067 Phillips, F. M., Argento, D. C., Balco, G., Caffee, M. W., Clem, J., Dunai,  
2068 T., Finkel, R., Goehring, B., Gosse, J. C., Hudson, A., Jull, T. A., Kelly,  
2069 M., Kurz, M., Lal, D., Lifton, N., Marrero, S. M., Nishiizumi, K., Reedy,  
2070 R., Schaefer, J., Stone, J. O., Swanson, T., & Zreda, M. G. (2015). The  
2071 cronus-earth project: A synthesis. *Quaternary Geochronology*, *CRONUS-*  
2072 *Earth*, submitted.
- 2073 Phillips, F. M., & Plummer, M. A. (1996). CHLOE: a program for interpret-  
2074 ing in-situ cosmogenic nuclide data for surface exposure dating and erosion  
2075 studies. *Radiocarbon (Abstr. 7th Int. Conf. Accelerator Mass Spectrom-*  
2076 *etry)*, 38, 98–99.
- 2077 Pigati, J., Lifton, N., Jull, A., & Quade, J. (2010). A simplified in situ  
2078 cosmogenic  $^{14}\text{C}$  extraction system. *Radiocarbon*, 52, 1236–1243.
- 2079 Pigati, J. S., & Lifton, N. (2004). Geomagnetic effects on time-integrated  
2080 cosmogenic nuclide production with emphasis on in situ  $^{14}\text{C}$  and  $^{10}\text{Be}$ .  
2081 *Earth and Planetary Science Letters*, 226, 193–205.

- 2082 Reedy, R. C. (2013). Cosmogenic nuclide production rates: Reaction cross  
2083 section update. *Nuclear Instruments and Methods in Physics Research*  
2084 *Section B - Beam Interactions with Materials and Atoms*, 294, 470–474.
- 2085 Sato, T., Yasuda, H., Niita, K., Endo, A., & Sihver, L. (2008). Development  
2086 of PARMA: PHITS-based analytical radiation model in the atmosphere.  
2087 *Radiation Research*, 170, 244–259.
- 2088 Schaefer, J. M., Denton, G. H., Kaplan, M. R., Putnam, A. E., Finkel, R.,  
2089 Barrell, D. J. A., Andersen, B. G., Schwartz, R., Mackintosh, A., Chinn,  
2090 T., & Schluchter, C. (2009). High-frequency holocene glacier fluctuations  
2091 in new zealand differ from the northern signature. *Science*, 324, 622–625.
- 2092 Schaefer, J. M., Winckler, G., Blard, P.-H., Balco, G., Shuster, D., Friedrich,  
2093 R., & Schluechter, C. (2014). Performance of CRONUS-P: a pyroxene  
2094 reference material for helium isotope analysis. *Quaternary Geochronology*,  
2095 *CRONUS-Earth Special Volume*, doi:10.1016/j.quageo.2013.09.003.
- 2096 Schaller, M., Ehlers, T., Blum, J., & Kallenberg, M. (2009). Quan-  
2097 tifying glacial moraine age, denudation, and soil mixing with cosmo-  
2098 genic nuclide depth profiles. *Journal of Geophysical Research*, 114, doi:  
2099 10.1029/2007/JF000921.
- 2100 Schimmelpfennig, I. (2009). *Cosmogenic  $^{36}\text{Cl}$  in Ca and K rich minerals:  
2101 analytical developments, production rate calibrations and cross calibration  
2102 with  $^3\text{He}$  and  $^{21}\text{Ne}$* . Doctorale Universite Paul Cezanne Aix-Marseille III  
2103 Cerege.
- 2104 Schimmelpfennig, I., Benedetti, L., Finkel, R., Pik, R., Blard, P.-H., Bourlès,  
2105 D., Burnard, P., & Williams, A. (2009). Sources of in-situ  $^{36}\text{Cl}$  in  
2106 basaltic rocks. Implications for calibration of production rates. *Quater-  
2107 nary Geochronology*, (pp. 441–461).
- 2108 Schimmelpfennig, I., Benedetti, L., Pik, R., Burnard, P., Blard, P., Dunai,  
2109 T. J., & Bourles, D. L. (2008). In situ cosmogenic  $^{36}\text{Cl}$  production rate  
2110 calibration from Ca and K in lava flows. *Goldschmidt Abstracts*, .
- 2111 Shea, M. A., & Smart, D. F. (1983). A world grid of calculated cosmic ray  
2112 vertical cutoff rigidities for 1980. *Proceedings from the 18th International  
2113 Cosmic Ray Conference*, 3, 415–418.

- 2114 Stone, J. (2000). Air pressure and cosmogenic isotope production. *Journal*  
2115 *of Geophysical Research*, *105*, 23753–23760.
- 2116 Stone, J. O. H., Evans, J. M., Fifield, L. K., Allan, G. L., & Cresswell,  
2117 R. G. (1998). Cosmogenic chlorine-36 production in calcite by muons.  
2118 *Geochimica et Cosmochimica Acta*, *62*, 433–454.
- 2119 Uppala, S., Kallberg, P., Simmons, A., Andrae, U., Bechtold, V., Fiorino,  
2120 M., Gibson, J., Haseler, J., Hernandez, A., Kelly, G., Li, X., Onogi, K.,  
2121 Saarinen, S., Sokka, N., Allan, R., Andersson, E., Arpe, K., Balmaseda,  
2122 M., Beljaars, A., Berg, L., Bidlot, J., Bormann, N., Caires, S., Chevallier,  
2123 F., Dethof, A., Dragosavac, M., Fisher, M., Fuentes, M., Hagermann, S.,  
2124 Holm, E., Hoskins, B., Isaksen, L., Janssen, P., Jenne, R., McNally, A.,  
2125 Mahfouf, J., Morcrette, J., Rayner, N., Saunders, R., Simon, P., Sterl, A.,  
2126 Trenberth, K., Untch, A., Vasiljevic, D., Viterbo, P., & Woollen, J. (2005).  
2127 The ERA-40 reanalysis. *Quarterly Journal of the Royal Meteorological*  
2128 *Society*, *131*, 2961–3012.
- 2129 Vermeesch, P., Balco, G., Blard, P.-H., Dunai, T. J., Kober, F., Nieder-  
2130 mann, S., Shuster, D., Strasky, S., Stuart, F., Wieler, R., & Zimmerman,  
2131 L. (2012). Interlaboratory comparison of cosmogenic  $^{21}\text{Ne}$  in quartz. *Qua-*  
2132 *ternary Geochronology*, <http://dx.doi.org/10.1016/j.quageo.2012.11.009>,  
2133 *CRONUS-Earth Special Volume*.
- 2134 Wieler, R., Beer, J., & Leya, I. (2013). The Galactic Cosmic Ray Inten-  
2135 sity over the Past  $10^6$ - $10^9$  Years as Recorded by Cosmogenic Nuclides in  
2136 Meteorites and Terrestrial Samples. *Space Science Reviews*, *176*, 351 –  
2137 363.
- 2138 Williams, A., Stuart, F., Day, S., & Phillips, W. (2005). Using pyroxene  
2139 microphenocrysts to determine cosmogenic  $^3\text{He}$  concentrations in old vol-  
2140 canic rocks: an example of landscape development in central gran canaria.  
2141 *Quaternary Science Reviews*, *24*, 211–222.
- 2142 Ziegler, L. B., Constable, C. G., Johnson, C. L., & Tauxe, L. (2011).  
2143 PADM2M: a penalized maximum likelihood model of the 0-2 Ma paleo-  
2144 omagnetic axial dipole moment. *Geophys. J. Int.*, doi: 10.1111/j.1365-  
2145 246X.2010.04905.x, .

2146 Zreda, M., Desilets, D., Ferre, T. P. A., & Scott, R. L. (2008). Measuring soil  
2147 moisture content non-invasively at intermediate spatial scale using cosmic-  
2148 ray neutrons. *Geophysical Research Letters*, 35.